

An Investigation into the Nature of the
Relativistic Compact Object in the Micro-quasar
System LS 5039:
A Multi-wavelength Study

Brian van Soelen

Submitted in fulfillment of the requirements for the degree
Magister Scientiae
in the Faculty of Natural and Agricultural Sciences,
Department of Physics,
University of the Free State,
South Africa

Date of submission: 30th November 2007

Supervised by: Prof P.J. Meintjes, Department of Physics

Abstract

LS 5039 is a high mass binary system that shows multi-wavelength broad non-thermal emission. It is also a very high energy gamma-ray emitter, with TeV energy gamma-rays detected by H.E.S.S. (High Energy Stereoscopic System). The nature of the compact object is unknown, but a mass $> 1.44 M_{\odot}$ is implied by the lack of an X-ray eclipse. The presence of radio jet-like structures and a proposed mass of $3.7 M_{\odot}$, under the assumption that the system is pseudo-synchronized, has led to the system's classification as a microquasar. Another model, in terms of a pulsar wind has also been proposed for the system. This study undertakes a model independent investigation of LS 5039 (neither microquasar nor pulsar), to attempt to determine what conclusions can be drawn from the system from first principles. A brief review of certain aspects of high mass binary theory is first presented, including accretion, binary motion, non-thermal radiation and mass outflow processes. The analysis looks at thermal evaporation from a disc structure in a black hole system, showing that this is unlikely, given the required temperature and the lack of thermal emission observed. The required conversion efficiency $> 20\%$ of accretion power in the black hole scenario also suggests that an additional reservoir of power is needed. The presence of a rotating magnetized neutron star, provides not only the magnetic field required to produce the non-thermal emission, it also supplies an additional power source, i.e the rotational kinetic energy of the neutron star. The magnetic field strengths and electron energies (for single particles) required to produce the very high energy gamma-rays is considered. An analysis of a fast rotating magnetosphere suggests that the centrifugal force exerted on the wind material could prevent accretion in the system. The power for the system is then extracted by a turbulent MHD process near the Alfvén radius.

Key words: LS 5039 – high mass X-ray binary – neutron star – black hole – wind accretion – non-thermal emission – propeller effect – magnetohydrodynamics

Opsomming

LS 5039 is 'n hoë massa binêre sisteem wat multi-golflengte nie-termiese uitstraling wys. Dit straal ook baie hoë energie gammastrale uit, met TeV energie gammastrale wat waargeneem is deur H.E.S.S. Die aard van die kompakte voorwerp is onbekend, maar 'n massa $> 1.44 M_{\odot}$ word geimpliseer deur die afwesigheid van 'n X-straal verduistering. Die teenwoordigheid van radio spuite en 'n voorgestelde massa van $3.7 M_{\odot}$, onder die aanname dat die sisteem pseudo-gesinkroniseer is, het gelei tot 'n klassifikasie van 'n mikrokwasar sisteem. 'n Ander model, in terme van 'n vinnig roterende neutron ster, is ook voorgestel vir die sisteem. Hierdie studie bied 'n model-onafhanklike ondersoek van LS 5039, in 'n poging om te bepaal watter gevolgtrekkings van die sisteem gemaak kan word vanuit eerste beginsels. 'n Kort oorsig oor sekere aspekte van die hoë massa binêre teorie word eerste gebied, wat akkresie, binêre baanbeweging, nie-termiese radiasie en massa uitstroming prosesse insluit. Die analise wys dat termiese verdamping van 'n skyfstruktuur in 'n gravitasiekolk onwaarskynlik is, gegee die nodige temperatuur en die tekort aan termiese uitstraling. Die nodige omskakel doeltreffendheid $> 20\%$ van akkresie energie in die geval van 'n gravitasiekolk toon ook aan dat 'n addisionele energiebron nodig is. Die teenwoordigheid van 'n roterende gemagnetiseerde neutron ster verskaf nie slegs die magneetveld wat nodig is om die nie-termiese straling te produseer nie, maar dien ook as 'n addisionele energiebron, d.w.s die rotasionele kinetiese energie van die neutron ster. Die magnetiese veldsterktes en elektron energieë (vir enkel deeltjies) wat benodig word om die baie hoë energie gamma strale te produseer, word beskou. 'n Analise van 'n vinnig roterende magnetosfeer stel voor dat die sentrifugale effek wat op die wind materiaal uitgeoefen word, akkresie in die sisteem verhinder. Die drywing vir die sisteem is dan afkomstig van 'n turbulente MHD proses naby die Alfvén radius.

Sleutelwoorde: LS 5039 – Ho massa X-straal binre sisteem – neutron ster – gravitasiekolk – wind akkresie – nie-termiese emissie – propeller effek – magnetohidrodinamika

Contents

1	Introduction	1
1.1	High Mass X-ray Binaries	3
1.2	Microquasars	5
1.3	Observations of LS 5039	7
1.3.1	Optical	7
1.3.2	Radio	12
1.3.3	X-ray	15
1.3.4	Gamma-ray	19
1.4	Motivation for this Study	20
2	High Mass Binary Systems	22
2.1	Binary Systems	22
2.1.1	The Two-Body Problem	22
2.1.2	Orbital Diagram	25
2.2	Accretion	26
2.2.1	Roche Lobe Overflow	27
2.2.2	Wind Accretion	31
2.2.3	Disc Accretion	33
2.2.4	Accretion onto a Compact Object	39
2.3	Neutron Stars/Pulsars	50
2.3.1	Properties of Neutron Stars	51
2.3.2	The Pulsar Wind	53
2.3.3	Pulsar Spin-Down Power	56
2.4	Black Holes	58
2.4.1	Non-Rotating Black Holes	58
2.4.2	Kerr Black Holes	59
2.5	Evolution of High Mass X-ray Binaries	60
2.5.1	Stellar Evolution	61
2.5.2	The Conservative HMXB Binary Evolution	62

2.6	Observational Properties of HMXBs	65
2.6.1	Optical Observations	65
2.6.2	Spectroscopic	66
2.6.3	X-ray Observations	67
3	Radiation and Mass Outflow Theory	70
3.1	Radiation Theory	70
3.1.1	Black Body Radiation	70
3.1.2	Synchrotron Radiation / Cyclotron Radiation	72
3.1.3	Inverse Compton Scattering	74
3.1.4	Gamma-ray absorption	77
3.2	Pulsar Wind Nebula	78
3.2.1	The Pulsar Wind	79
3.2.2	The Nebula	80
3.2.3	Kennel-Coroniti Model	83
3.2.4	Bow Shocks	85
3.2.5	Application to High Mass Binaries	87
3.3	Jets and Disc Outflow	94
3.3.1	Accretion Disc Mass Outflow	94
3.3.2	Blandford-Znajek Model	97
3.3.3	Jets in PWNe	102
4	A Model Independent Approach towards Solving the Mysteries of LS 5039	106
4.1	The Broad Band Spectrum	107
4.2	System Parameters	108
4.2.1	Binary Separation and Velocity	109
4.2.2	Wind Accretion Ratio	110
4.3	A Thermal Driven Jet Outflow in LS 5039?	112
4.3.1	Fraction of Particles	113
4.3.2	Application to LS 5039	115
4.4	A Magnetized Compact Object	119
4.4.1	Requirements of High Energy Non-thermal Emission	121
4.4.2	Magnetic Field Strength	124
4.4.3	Magnetosphere–Stellar Wind Interaction	125
4.4.4	Non-thermal Radiation at the Alfvén radius	126
4.4.5	Effective Gravity: A MHD Propeller in LS 5039	133
4.4.6	MHD Power	136
4.5	Magnetosphere as a Power Source	143
5	Conclusion	145

Acknowledgements	149
List of Acronyms	151
Bibliography	151

Chapter 1

Introduction

LS 5039 is a fascinating High Mass X-ray Binary (HMXB) system that exhibits a wide range of multi-wavelength features. The system was originally cataloged in the *Luminous Stars in the Southern Milky Way* catalogue (Stephenson and Sanduleak, 1971). This was an extension of the *Luminous Stars in the Northern Milky Way* catalogue that was published 12 years earlier (Hardop et al., 1959). The Southern-sky observations were performed at the Schmidt telescope, Cerro Tololo, Chile, where the observations had to match those made at the Hamburger Sternwarte, Warner and Swasey Observatory, in Germany, used for the northern sky survey. To this end, even the prism used was shipped to Chile to be used in the Schmidt telescope.

The system's association with a possible X-ray source was based on a comparison between the ROSAT All Sky Survey and the compiled SIMBAD Catalogue for OB type stars (Motch et al., 1997). The search looked for X-ray sources above 10^{31} erg s⁻¹ that matched stars younger than B6. This resulted in five stars being identified as possible HMXB candidates, namely, LS 5039, BSD 24-491, LS 992, LS 1698 and LS I +61 235. These authors proposed that LS 5039 was the most likely candidate for the optical companion of the ROSAT source RX J1826.2-1450. Based on the hardness of the spectrum they suggested that it was an accretion driven system where the compact object most likely accreted from the stellar wind of an O-type star (Motch et al., 1997).

The following year, as part of a search for Radio Emitting X-ray Binaries (REXRBs), Martí, Paredes, and Ribó (1998), observed LS 5039 with the Very Large Array (VLA) at 20, 6, 3.5 and 2.0 cm wavelengths. The images showed that LS 5039 was associated with an unresolved radio source, as shown in Figure 1.1.

In Paredes et al. (2000) the authors reported on a follow-up radio observation done in May of 1999 at 5 GHz with the Very Long Baseline Array (VLBA). This showed what appears to be bi-polar radio jets in the system (Figure 1.2). Later observations with the European VLBI Network (EVN) and Multi-Element Radio Linked Interferometer Network (MERLIN) confirmed these results (Paredes et al., 2002)(see Figure 1.16). These later observations resulted in the

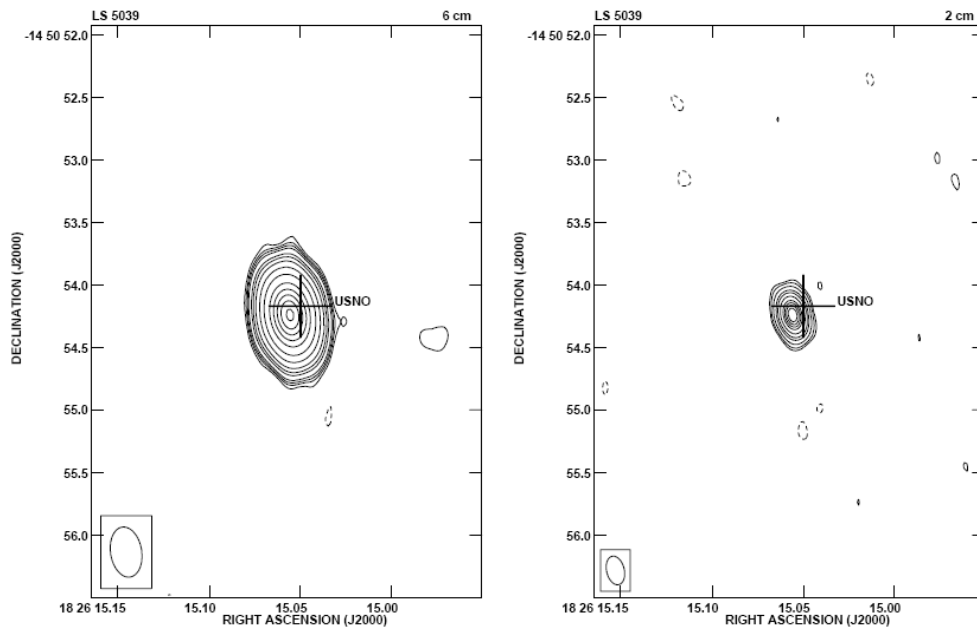


Figure 1.1: **Left** 3.5 cm and **right** 2.0 cm image of LS 5039, taken with the VLA (Martí et al., 1998).

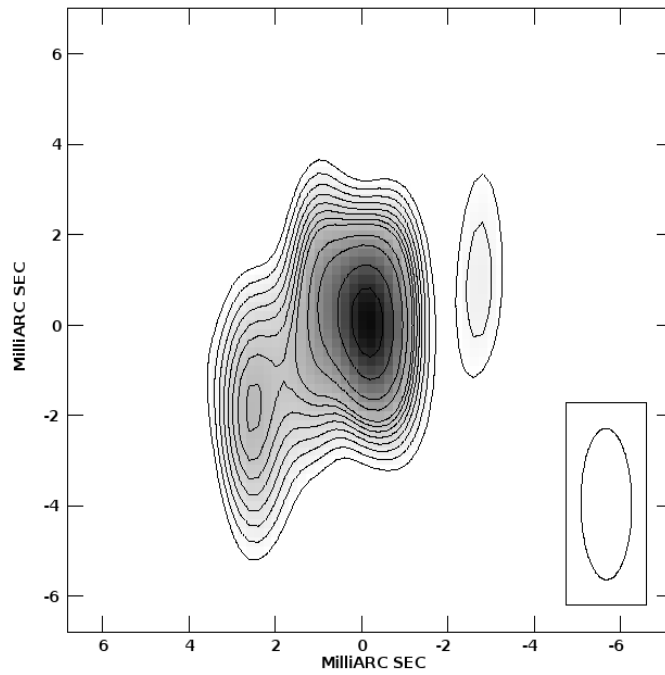


Figure 1.2: 5 GHz radio image resolved with the VLBA (Paredes et al., 2000).

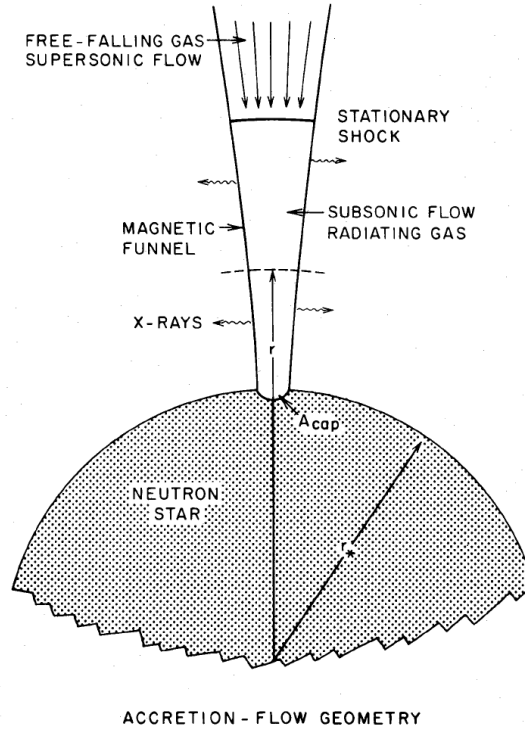


Figure 1.3: Accretion of material onto the surface of a neutron star (Langer and Rappaport, 1982a). Material is channelled along magnetic field lines and accretes onto the the poles. Shock fronts appear to be a consequence of this accretion (accretion columns) (see Section 2.2.4)

system being classified as a microquasar.

Before focusing on LS 5039 directly, a brief discussion of HMXBs will be presented.

1.1 High Mass X-ray Binaries

A detailed review on X-ray binaries is given in White (1989) and Frank, King, and Raine (1992). X-ray binary (XRB) systems are, as their name implies, prodigious sources of X-ray emission, consisting of two stars orbiting their common centre of mass. When the mass donor star in the system is less massive than the accreting star, the system is called a *Low Mass X-ray Binary* (LMXB). When the compact object is accreting from an optical companion with a higher mass than itself, the system is called a *High Mass X-ray Binary* (HMXB). HMXB systems normally consist of a neutron star (NS) or black hole (BH), while the heavier optical companion is normally a B or O-type giant. These systems are believed to be accretion driven, where gravitational energy released during the accretion of material onto the compact object results in prodigious X-ray emission. Figure 1.3 shows an example of accretion onto a NS.

A simple estimate of the amount of gravitational potential energy that is released is given by

$$\begin{aligned}\Delta E_{acc} &= \frac{GMm}{R} \\ &= 10^{20} \left(\frac{M}{M_{\odot}}\right) \left(\frac{m}{1 \text{ g}}\right) \left(\frac{R_{\star}}{10^6 \text{ cm}}\right)^{-1} \text{ erg},\end{aligned}\tag{1.1}$$

where we consider a $1 M_{\odot}$ ($M_{\odot} \approx 2 \times 10^{33} \text{ g}$) compact object (NS) with a radius of $R_{\star} = 10 \text{ km}$. Comparison with the rest-mass energy of a similar mass ($m = 1 \text{ g}$) of material, $\epsilon_0 = mc^2 \approx 9 \times 10^{20} \text{ erg}$, implies a conversion efficiency of $\sim 10\%$ of the rest mass into energy during accretion onto a neutron star. The conversion efficiency of a non-rotating black hole is (e.g. Frank et al. (1992))

$$\begin{aligned}\Delta E_{acc} &= 0.057c^2 \text{ erg g}^{-1} \\ &= 5.12 \times 10^{19} \left(\frac{m}{1 \text{ g}}\right) \text{ erg},\end{aligned}$$

lower than in the case of a NS. This occurs because there is no hard surface onto which the material can accrete and because the last stable (non-Newtonian) orbit at $3R_{Schw}$ has a lower potential than a Newtonian orbit would have.

HMXBs are formed from short lived stellar systems, where one of the stars has already passed through its supernova (SN) phase. Usually SN events have a profound influence on the system. Not only can they increase the eccentricity of the orbit, but they also impart a proper motion to the system, relative to the galactic plane*. In the case of LS 5039, its orbital eccentricity is $e = 0.35 \pm 0.04$ (Casares et al., 2005), while its proper motion out of the galactic plane has been estimated at $v \simeq 150 \text{ km s}^{-1}$ (Ribó et al., 2002).

Accretion onto the compact object, in HMXBs, occurs through either wind accretion, where material is captured by the gravitational potential of the compact object while moving along its orbit, or through Roche lobe overflow (e.g. Frank, King, and Raine (1992) and references therein). Roche lobe overflow results in higher accretion rates onto the surface of the compact object since material is directed across the L_1 point by the effective gravity. However, in some wind accreting systems the gravitational potential of the compact object can result in the wind being preferentially directed towards it, resulting in an increased accretion rate.

The HMXB class can be divided into Be-X-ray binaries (Be-XRBs) and Supergiant X-ray binaries (SXRBs). The former consists of fast rotating B type stars, where the spin period approaches the breakup period. As a result these stars show enhanced wind outflow around their equator, that can result in a disc-like structure forming around them. An example of such an HMXB system is the pulsar PSR B1259-63 that is in a highly eccentric orbit around the Be star SS 2883 (see for example Johnston et al. (1992)). In this system, a known gamma-ray emitter (Aharonian et al., 2005), the radio pulsations become eclipsed by the disc-like outflow

*This is due to the asymmetry of the SN explosion.

from the Be star.

It is believed that the rapid rotation of the Be star is intimately tied to the evolution of the binary system. Since the accreting object (NS or BH) has already passed its supernova phase, it would at an earlier stage have been the larger of the two stars, most probably filling its Roche lobe. At that stage, the high accretion rate of matter onto the Be star could have resulted in it being spun-up to its high rotational velocity (Rappaport and van den Heuvel, 1982).

Be-XRBs belong to the III-V luminosity class[†], with orbital periods ranging between 16 and 400 days (Coe, 2000). These systems are normally very bright transient sources, a result of their eccentric orbits. Close to periastron they appear as X-ray sources where the decrease in binary separation results in an increase in accretion. The compact object in Be-XRBs is normally an accreting pulsar with a rotation period of the order of seconds. The pulsars generally show evidence of being spun-up, a phenomenon normally associated with an accretion disc (see White (1989) and references therein).

The second class of XRB, i.e. the SXRBs, consist of stars in the luminosity class I-II, and have orbital periods between about 1.4 and 41 days. The mass donor stars are supergiants, typically O and B class stars. Due to the fact that many of the optical giants in these systems fill – or nearly fill – their Roche lobes, the giants becomes elongated, resulting in ellipsoidal variations in the optical light. As with the Be-XRBs, most systems appear to contain pulsars. There are, of course, always exceptions to the rule. A number of systems are believed to be BH candidates, notably Cyg X-1 (see Webster and Murdin (1972) & Bolton (1972)). Other systems may contain pulsars, but the inclination of the rotation axis of the NS makes it impossible to observe the pulsation. This has been proposed, for example in 4U 1700-37 (Gottwald et al., 1986). In the SXRb class, systems that exhibit high luminosity normally show a slow but steady spin-up or spin-down of the pulse period, while the low luminosity systems appear to show more random changes, possibly associated with changes in the wind accretion onto the compact object.

Various HMXB systems also show jet-like structures and emissions (see e.g. Figure 1.4), i.e. the so called microquasars, because of their similarity to distant quasar systems. These fascinating objects will be the focus of attention in the next section.

1.2 Microquasars

Microquasars are HMXBs that exhibit properties and characteristics similar to those of the very distant quasars (for a detailed review see Fender (2006) and Ribó (2005)). Their similarity is not only superficial, only resembling the distant quasars, but they appear to exhibit similar properties. For this reason, it has long been hoped that microquasars can be utilized to increase our understanding of the physical processes in quasars. They are less distant and thus, in

[†]The luminosity class defines the size of a stellar object based on its total luminosity. The different classes are: I: supergiants, II: bright giants, III: giants, IV: subgiants, V: main sequence and dwarfs, and VI: subdwarfs and white dwarfs (Lang, 1974).

principle, should be easier to observe. In addition to this, microquasar events occur over a much shorter timescale than events in quasars.

There appears to be a scaling relationship with mass between the extra-galactic quasars and the galactic microquasars when the compact object in the system is a black hole. The three properties that scale with mass are:

1. The inner temperature of the accretion disc.
2. The size of the jets.
3. Emission timescales related to accretion of matter.

For the super-massive black holes ($10^6 - 10^9 M_\odot$) in quasars, the inner disc temperature is $\sim 10^5$ K, resulting in optical emission, while in microquasars, with solar mass black holes, the temperature is higher, approximately 10^7 K, resulting in a dominant X-ray emission[‡]. The size of the radio jets in microquasar systems are also much smaller, on the order of AU[§] for compact jets and up to parsecs[¶] for large jets, compared to the jets in quasars that exist on scales up to several million parsecs. The last scaling effect, the time scale, varies with the Schwarzschild radius, i.e. $\tau \simeq \frac{R_{Schw}}{c} = \frac{2GM}{c^3} \propto M$, the mass of the compact object. This timescale, i.e. the light crossing time over length scales comparable to the Schwarzschild radius, determines the duration of emission due to accretion of material across the event horizon.

Some authors, for example Fender (2006), have suggested that all HMXBs, with the exception of certain pulsar systems where accretion would be disrupted, are microquasars. This is not really quantifiable as a result of the resolution limitations of observational astronomy. While the validity of such a statement is difficult to evaluate, the total number of microquasars is currently believed to be approximately 15 out of a population of ~ 280 XRBs (see Ribó (2005) and references therein) and 130 HMXB (Liu et al., 2000).

The jets that are seen in microquasars can be characterised into three groups (Ribó, 2005) i.e.,

1. Compact jets.
2. Discrete ejection.
3. Large-scale jets.

The compact jets reach up to AU scales and have flat or inverted^{||} radio spectral indices. The discrete ejection (i.e. non-continuous) jets occur during the state transition, during which the

[‡]This is a result of how the inner temperature of an accretion disc scales with the mass of the compact object, M_X . The temperature of the disc at a radius R is given by Equation 2.25. If the last stable orbit is taken as $3R_{Schw}$ and the radius of the compact object as R_{Schw} , then it can be shown that under the assumption that the accretion rate is close to the Eddington limit that the temperature scales as $T \propto M_X^{-1/4}$.

[§]AU: The Astronomical Unit is the mean distance between the Earth and the Sun $\sim 1.5 \times 10^{13}$ cm.

[¶]parsec: A parsec is a measure of distance based on the annual parallax of stars due to the orbital motion of the Earth. 1 parsec = 3.0856×10^{18} cm, is the distance from the Sun to a point where the observed annual parallax would be 1 arc second.

^{||}A spectrum is considered inverted if $\alpha \geq 0$ when $S_\nu \propto \nu^{+\alpha}$ (Ribó, 2005).

radio spectral index becomes optically thin. This is consistent with an adiabatic expansion of electrons in the ejected material. The large scale jets extend up to parsec scales (e.g. GRS 1758-2898, (Rodríguez et al., 1992)). While there is no direct evidence for it, it is normally assumed that jets in microquasars are linked to accretion discs, since there are only a few astrophysical examples where a disc is not associated with a jet (e.g. LS 5039).

The prototype microquasar, SS 443, was originally reported by Margon et al. (1979), in an article entitled *The Bizarre Spectrum of SS 433*, as they could find no periodic pattern within their observations of the system. It was suggested by Fabian and Rees (1979) that this “bizarre” spectrum could be modelled by means of a double jet of accelerated material. Later radio interferometry of SS 433 appeared to verify this, (see e.g. Gilmore and Seaquist (1980)). Recent VLA observations of SS 433 (Figure 1.4) show the precessing of the radio jets which creates a corkscrew-shaped radio image (see for example Hjellming and Johnston (1982) & more recently Blundell and Bowler (2004)).

LS 5039 presents some similarities and differences to SS 433. For example, both systems exhibit double-sided radio jets (speed $\sim 0.26c$; see e.g. Blundell and Bowler (2004)), with a non-thermal spectrum (see e.g. Seaquist et al. (1980)). However, SS 433 is believed to be a Roche lobe filling system, with an accretion rate, $\dot{M} = 10^{-4}M_{\odot} \text{ yr}^{-1}$, and a X-ray luminosity ($L_X \sim 3 \times 10^{35} - 10^{36} \text{ erg s}^{-1}$; see Fabrika (2004) and references therein) much higher than LS 5039.

The mechanism behind the production of jets in microquasars is not certain. Numerous theories for jet formation in microquasars (e.g. Blandford and Payne (1982)) as well as other systems such as pulsar nebulae (e.g. Lyubarsky (2002)) have been proposed, some of which will be discussed later (see Section 3.3).

1.3 Observations of LS 5039

LS 5039 is a Southern Hemisphere source (Right ascension: 18h 26m 15.034s; Declination: $-14^{\circ} 50' 53.59''$), making it an excellent source to observe in South Africa. This section summarizes some of the most important observations of LS 5039. It provides a brief overview of most observations to present an overall picture of the system. The discussion will begin with the optical observations before continuing with the radio, X-ray and gamma-ray observations.

1.3.1 Optical

As mentioned earlier, LS 5039 was originally catalogued during the *Luminous Star Survey* (Stephenson and Sanduleak, 1971), where it was classified as a OB+r type star (the +r term indicates possible reddening). In 1975, Drilling (Drilling, 1975) reported on *UBV* photometry of stars with a magnitude less than 12 and a declination less than 15° , that had been listed in the *Luminous Star Survey*. The observations were performed at the Kitt Peak National Observatory using a refrigerated 1P21 photomultiplier and standard filter set. The results for LS 5039 are

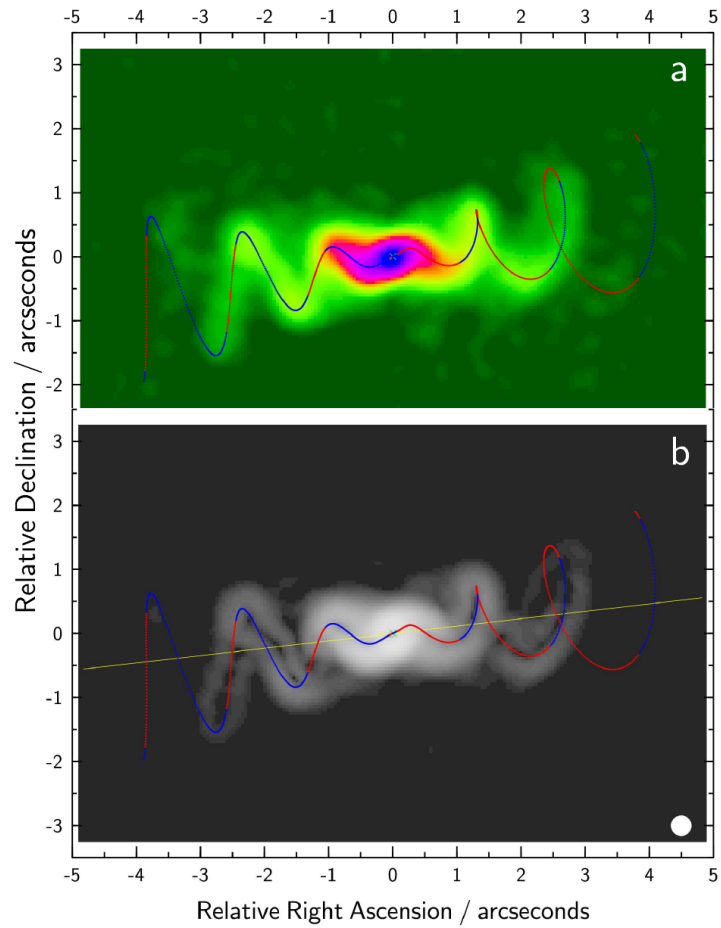


Figure 1.4: **a**: VLA observation of SS 433 (4.85 GHz, A-configuration) A dynamic model is overlaid to explain the jet shape (see Blundell and Bowler (2004) for details). **b**: Similar image to **a**, where a Sobel-filtered image is used (Blundell and Bowler, 2004).

Table 1.1: Photometric results for LS 5039 from the *Luminous Stars in the Southern Milky Way* survey (Drilling, 1975).

Star	Sp.	V	error	$B-V$	error	$U-B$	error	n
5039	OB^+r	11.23	± 0.023	0.94	± 0.009	-0.16	± 0.016	2

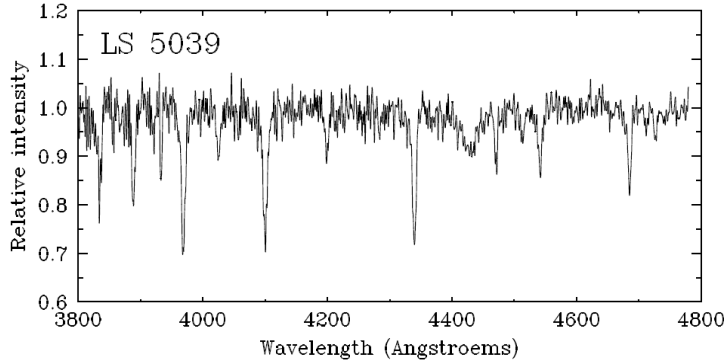


Figure 1.5: Rectified blue spectrum of LS 5039 created using the ESO-MPI 2.2 m + EFOSC2, with a 5 minute exposure time (Motch et al., 1997).

shown in Table 1.1, where *Star* is the star number in the catalogue, *Sp* is the spectral type, V , $B-V$ and $U-B$ are the magnitude and colour measurements of the star, the *error* columns are the estimated internal mean errors for each filter respectively, and n is the number of times the star was observed. LS 5039 was found to be a $V = 11.23$ magnitude star, and showed no change in magnitude in the two observations.

Spectroscopic Classification

While searching for additional X-ray binary sources, Motch et al. (1997), undertook additional optical observations of LS 5039. The authors classified the star as $O7V((f))$ based on the observed He II λ 4686 absorption and weak N III λ 4634-4642 emission found in the medium resolution blue spectrum shown in Figure 1.5.

Clark et al. (2001) reported on spectroscopic observations that occurred between 1995-2000 in optical (4100-7400 Å) and near infra-red (1.5-2.2 μ m) wavelengths. The optical spectroscopy classified the system as a O6.5 type star, due to the ratio between the He II 4541 and He I 4471 lines. The strong absorption of He II 4686 in LS 5039 showed that it is a main-sequence star, while the strong He II absorption in combination with the weak N III λ 4634-40-42 emission classified the star as an O6.5((f)) type giant. Figure 1.6 shows the blue-end spectrum of LS 5039, reported by Clark et al. (2001). The normalized flux lies between the O6V((f)) and O7V((f)) standards. Spectroscopy in the near-infrared bands H and K was not conclusive enough to classify the spectral type of the optical star, but the results were not inconsistent with the

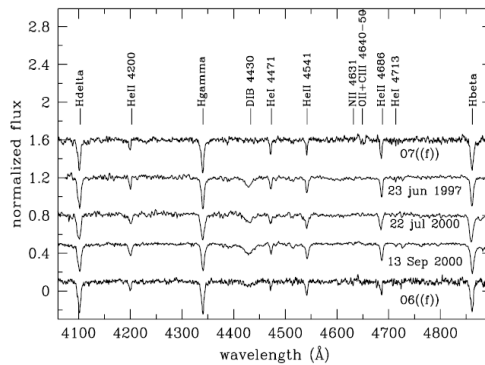


Figure 1.6: Blue end spectra of LS 5039 (4050-4950 Å) (Clark et al., 2001).

Table 1.2: Optical photometry of LS 5039 by Martí et al. (1998).

Date	<i>V</i>	<i>R</i>	<i>I</i>
2 June 1998	11.35	-	-
3 June 1998	11.33	-	-
7 June 1998	11.35	10.64	9.90
8 June 1998	11.39	10.69	9.95

O6.5((f)) classification.

Photometric Variability

With the increased interest in LS 5039 due to its classification as a radio emitting XRB, numerous observations have been performed to search for optical variability. The search by Martí et al. (1998) showed no significant change in magnitude, though they did suggest searching for further day to day variability. Their optical results were consistent with those of Drilling (1975), showing a $V \approx 11.3$ magnitude star (Table 1.2).

Clark et al. (2001) brought together archive data and recent observations by other authors with the more recent observations they had performed. This showed that the broad band spectrum between 1973 and 2001, shown in Table 1.3, displays a high degree of stability. This data includes Kilkenny et al. (1993), Spencer Jones et al. (1993) and Martí et al. (1998). The observed change in the *V* band over the 28 year period was less than 0.1 magnitude.

Observations in the *J*, *H* and *K* bands with the *Telescopio Carlos Sánchez* (1995–2000) are displayed in Table 1.4. The results show a very stable system with $J \sim 9$ mag, $H \sim 9$ mag and $K \sim 8.5$ mag and maximum variation of ~ 0.4 magnitude over a 5 year period.

Table 1.3: Broad band photometry of LS 5039 from Clark et al. (2001). Kilkenny et al. (1993) is given as K93, and Spencer Jones et al. (1993) is given as SJ93.

Observation	<i>B</i>	<i>V</i>	<i>R</i>	<i>I</i>	<i>J</i>	<i>H</i>	<i>K</i>	<i>L</i>
K93, SJ93	-	11.24±0.01	10.59±0.01	9.88±0.01	9.02±0.01	8.79±0.02	8.57±0.03	-
Oct 1996	12.18±0.02	11.33±0.02	10.65±0.02	9.87±0.02	9.05±0.02	8.75±0.02	8.60±0.02	8.69±0.05
1998 June 7	-	11.35±0.03	10.64±0.03	9.90±0.03	-	-	-	-
1998 June 8	-	11.39±0.03	10.69±0.03	9.95±0.03	-	-	-	-
2000 Sep	12.17±0.03	11.32±0.01	10.61±0.01	9.91±0.01	-	-	-	-

Table 1.4: *JKH* band observation of LS 5039 (Clark et al., 2001).

Date	<i>J</i>	<i>H</i>	<i>K</i>
14/10/95	9.06±0.01	9.04±0.01	8.93±0.03
31/7/96	9.05±0.03	8.93±0.03	8.85±0.03
19/7/97	9.06±0.01	8.91±0.01	8.88±0.01
21/7/97	9.07±0.02	8.90±0.02	8.83±0.02
26/7/99	9.04±0.02	8.91±0.02	8.82±0.01
28/7/99	9.10±0.02	9.04±0.02	9.01±0.02
31/7/99	8.97±0.02	8.71±0.02	8.58±0.02
2/10/99	9.01±0.02	8.76±0.02	8.63±0.02
7/10/99	9.02±0.02	8.74±0.02	8.55±0.02
6/7/00	8.99±0.02	8.75±0.02	8.65±0.04
17/10/00	9.05±0.02	8.81±0.02	8.65±0.01
18/10/00	8.97±0.02	8.68±0.02	8.53±0.01

System Parameters

The initial work on obtaining the system parameters for LS 5039 was performed by McSwain et al. (2001). They initially derived an orbital period of $P = 4.117 \pm 0.011$ days and an eccentricity of $e = 0.41 \pm 0.05$ in 2001. They later revised these values in 2004 (McSwain et al., 2004) to, $P = 4.4267 \pm 0.0005$ days, and $e = 0.48 \pm 0.06$. In the same paper the authors also proposed an effective temperature of $T_{eff} = 37500 \pm 1700$ K and a rotational velocity of $v \sin i = 140 \pm 8$ km s⁻¹ for LS 5039.

Casares et al. (2005) performed their own observations between 23–31 July 2002, and 1–10 July 2003, and combined the 196 data points they obtained with those reported by McSwain et al. (2001, 2004). This long time period analysis resulted in a new orbital period of 3.90603 ± 0.00017 days, an eccentricity of $e = 0.35 \pm 0.04$ and a revised mass function of $f(M) = 0.0053 \pm 0.0009 M_{\odot}$. The new spectral analysis gave revised values of $T_{eff} = 39000 \pm 1000$ K and $\log g = 3.85 \pm 0.10$ for the temperature and gravity of the star respectively.

Observations by Casares et al. (2005) of the changes in the H α line were associated with the star’s stellar wind loss (see their paper and references therein for a discussion). The authors proposed a wind mass-loss rate of $3.7 \times 10^{-7} M_{\odot} \text{ yr}^{-1}$, for the observed low state (with an upper limit of $5.0 \times 10^{-7} M_{\odot} \text{ yr}^{-1}$). For the observed high state a best fit value gave $7.5 \times 10^{-7} M_{\odot} \text{ yr}^{-1}$, with a lower and upper limit of $5.0 \times 10^{-7} M_{\odot} \text{ yr}^{-1}$ and $1.0 \times 10^{-6} M_{\odot} \text{ yr}^{-1}$ respectively.

1.3.2 Radio

As discussed in Section 1, LS 5039 was proposed as the optical counterpart to the ROSAT all sky survey source RX J1826.2-1450 by Motch et al. (1997). Radio observations of the source were followed up by Martí et al. (1998) using the VLA interferometer, producing the images seen in Figure 1.1. The radio spectrum of LS 5039 (Figure 1.7), appears to show non-thermal emission

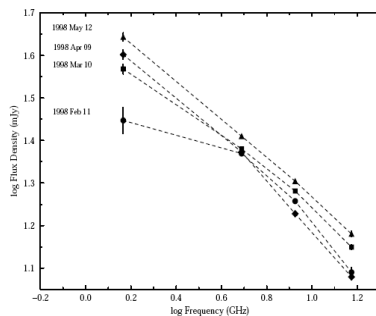


Figure 1.7: Radio spectrum of LS 5039 obtained by Martí et al. (1998). The spectrum, as discussed in the text, is typical of a non-thermal emission.

Table 1.5: Radio flux of LS 5039/RX J1826.2-1450 (Martí et al., 1998).

Date	Julian Day (JD2400000)	S20cm (mJy)	S6cm (mJy)	S3.5cm (mJy)	S2.0cm (mJy)
11 Feb 1998	50856.2	28 ± 2	23.4 ± 0.1	18.1 ± 0.1	12.3 ± 0.3
10 Mar 1998	50883.1	37 ± 1	24.0 ± 0.1	19.1 ± 0.1	14.1 ± 0.2
09 Apr 1998	50913.0	40 ± 1	23.6 ± 0.1	16.9 ± 0.1	12.0 ± 0.2
12 May 1998	50946.0	44 ± 1	25.7 ± 0.1	20.2 ± 0.1	15.1 ± 0.2

from LS 5039/RX J1826.2-1450. An example of the flux (as given by the authors) is

$$S_\nu = (52 \pm 1) \text{ mJy} \left(\frac{\nu}{1 \text{ GHz}} \right)^{-0.46 \pm 0.01}.$$

The observations showed a total integrated radio luminosity of $L_{rad} \sim 1.3 \times 10^{31} \text{ erg sec}^{-1}$ for an assumed distance of 3.1 kpc (further than the more current value of $2.5 \pm 0.1 \text{ kpc}$ (Casares et al., 2005)) and an assumption that the radio source extended from 0.1–100 GHz. Over long time periods (\sim years) the radio source was found to be persistent, though on shorter time periods (\approx 4 months – 11 Feb 98 \rightarrow 12 May 98) the flux showed significant fluctuation, particularly at the 20 cm wavelength, where it changed from $28 \pm 2 \rightarrow 44 \pm 1 \text{ mJy}$ (Table 1.5).

Martí, Paredes, and Ribó (1998), following the work of Pacholczyk (1970), assumed equipartition and believed that the total energy and magnetic strength of the radio source could be expressed by

$$E_{total} = c_{13}(1+k)^{4/7} \phi^{3/7} R^{9/7} L_{rad}^{4/7} \quad (1.2)$$

and

$$H = 4.5^{2/7} (1+k)^{2/7} c_{12}^{2/7} \phi^{-2/7} R^{-6/7} L_{rad}^{2/7}. \quad (1.3)$$

Here c_{12} and c_{13} are special functions of synchrotron theory (see Pacholczyk (1970)), R is the linear size of the synchrotron emitting region, ϕ is the fraction of that region that is covered by

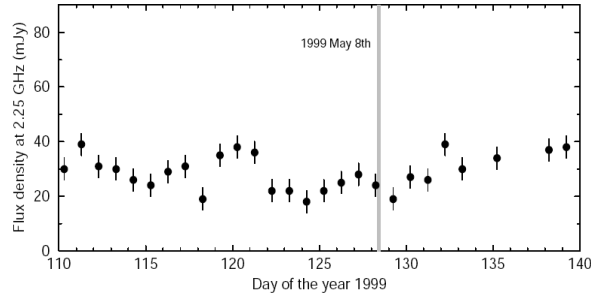


Figure 1.8: Radio flux observed with the GBI (Paredes et al., 2000). The source shows no signs of flaring and only a moderate variation in flux.

Table 1.6: Flux density at 5 GHz, measured with EVN and MERLIN (Paredes et al., 2002).

	EVN			MERLIN		
	S_5 GHz mJy	Length mas	PA °	S_5 GHz mJy	Length mas	PA °
Core	29.3	-	-	31.6	-	-
NW jet	2.6	24	-42	4.0	128	-29
SE jet	3.3	34	140	4.2	174	150

the magnetic field and k is the ratio between the electron and proton energies. Martí, Paredes, and Ribó (1998) found that the range of the energy and magnetic fields was 1.6×10^{38} erg $\leq E_{total} \leq 5.0 \times 10^{41}$ erg and 0.01 G $\leq B \leq 2.2$ G for the radio source.

The paper by Paredes et al. (2000), revealed radio jet images (Figure 1.2) taken with the VLBA. The authors estimated a 2 milliarcsecond size for the core of the system, with jets extended beyond 6 milliarcseconds with a position angle of 125° . The jets make up 20% of the measured flux of 16 mJy. Additional observation with the Green Bank Interferometer (GBI) showed no flaring events and only a small fluctuation in flux (Figure 1.8).

In 2002, Paredes et al. (2002), reported on follow up radio observations of LS 5039, done simultaneously on the European VLBI Network (EVN) and Multi-Element Radio-Linked Interferometer Network (MERLIN). The radio images show clear jet structures that extend NW and SE, with the SE jet again appearing longer in both of the EVN and MERLIN images (Figure 1.9). The measured fluxes and position angles (PA) are summarized in Table 1.6. The authors found a persistent jet with no signs of flaring. Assuming a distance of 2.9 kpc (Ribó et al., 2002) and an inclination angle of $\theta = 30^\circ$ proposed by McSwain and Gies (2002) they arrived at a true length of 200 AU and 1000 AU for the length of the SE arm and a total length of 350 AU and 1740 AU for the jet, as seen in the EVN and MERLIN images respectively.

Under the assumption that the asymmetry seen in the jet structures is the result of Doppler boosting, the authors searched for the speed of the jet by means of

$$\beta \cos \theta = \frac{\mu_a - \mu_r}{\nu u_a + \nu_r} = \frac{d_a - d_r}{d_a + d_r}, \quad (1.4)$$

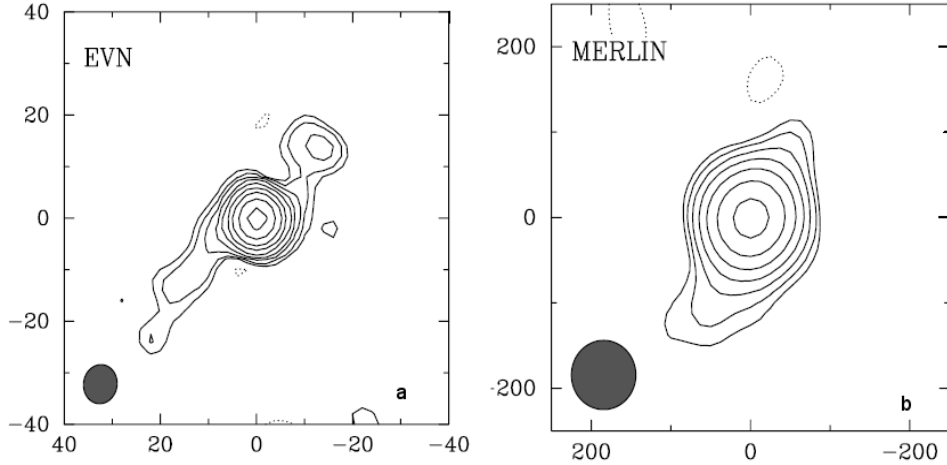


Figure 1.9: **a**: 5 GHz image of LS 5039 taken with the EVN. Synthesized beam is 7.60×6.96 mas **b**:. 5 GHz MERLIN image of LS 5039. The circular beam has a size of 81 mas. Note that the difference in resolution between the images implies that the EVN image lies well within the MERLIN image (Paredes et al., 2002).

where $\beta = v/c$, θ is the angle between the direction of the jet and line of sight, μ_a and μ_r are the proper motions of the approaching and receding jet respectively, and d_a and d_r are the measurable distances to the core. By using the measured length of the jets (Table 1.6), this gives a value of

$$\beta \cos \theta = 0.17 \pm 0.05,$$

the error being based on the errors in the measurement of the lengths. The authors estimated a velocity of $\beta = (0.20 \pm 0.06)$ based on an inclination angle of $\theta = i = 30^\circ$ (McSwain and Gies, 2002). This value would decrease slightly for the inclination of $i = 24^\circ.9 \pm 2^\circ.8$ proposed by Casares et al. (2005).

While the results of Paredes et al. (2000) (Figure 1.8) show some modulation of the radio flux, there have been insufficient radio observations to determine whether or not the radio flux is orbitally modulated. A search by Ribó et al. (1999) using data from the GBI (daily flux, 2.25 and 8.3 GHz) revealed no orbital modulation between 2 and 50 days. This does not remove the possibility of an orbital modulation since the low flux of the source and the use of an average daily flux may have hidden any modulation. The low intensity of the flux, $S_\nu \sim 29$ mJy at 5 GHz, unfortunately makes the source inaccessible to the *Hartebeesthoek Radio Astronomy Observatory*, making any South African radio observation of LS 5039 impossible at the moment.

1.3.3 X-ray

LS 5039 was proposed as the optical counter part for the ROSAT source RX J1826.2-1450 by Motch et al. (1997). This lead Ribó et al. (1999) to analyse data from the All Sky Monitor

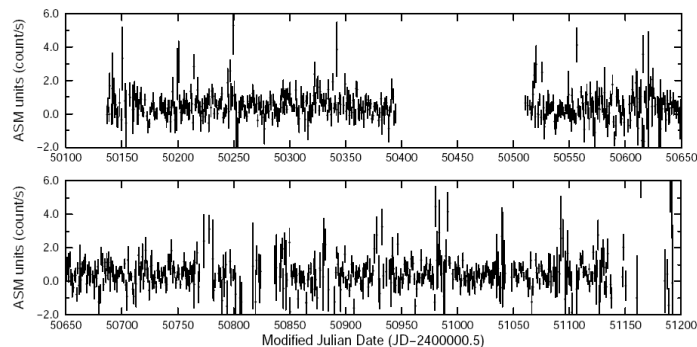


Figure 1.10: ASM data of RX J1826.2-1450/LS 5039 (1.5-12 keV) (Ribó et al., 1999). Data points represent the average flux for the day.

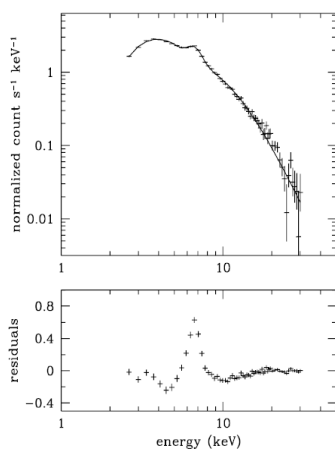


Figure 1.11: X-ray spectrum of LS 5039 (Ribó et al., 1999). The top image shows the best power law fit with a Gaussian iron component. The bottom image shows iron line when the power law component is removed.

(ASM) and Proportional Counter Array (PCA) located on the Rossi X-ray Timing Explorer (RXTE) satellite. The ASM data (1.5–12 keV) was for the period February 1996 – November 1998. Figure 1.10 shows the ASM data, where each point is the average flux for the day. No significant modulation was detected for a period of 2–200 days. The search for X-ray pulsations using the PCA data (8th and 16th February 1998; energy range 2-60 keV), revealed no pulsation between ~ 0.02 to ~ 2000 seconds.

Spectral fitting of RX J1826.2-1450/LS 5039 (Figure 1.11) showed a hard strong iron line at 6.6 keV, with no cut-off. Subsequent X-ray observations (see e.g. Bosch-Ramon et al. (2005)) have not shown this strong iron emission, suggesting that it was the result of contamination from the galactic ridge.

Observations of LS 5039 by Reig et al. (2003) with BeppoSAX covering the period of periastron showed no sign of an eclipse. The observation covered the orbital phase 0.89 - 0.11, on the

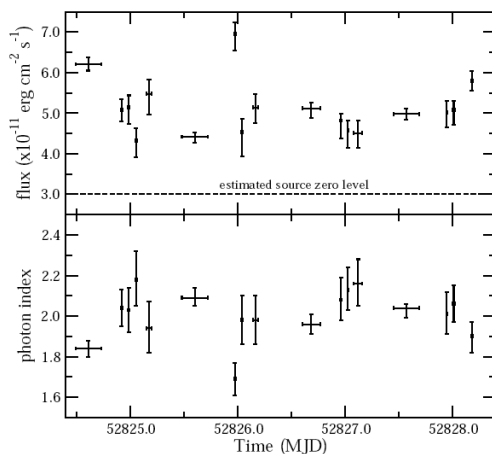


Figure 1.12: Unabsorbed X-ray flux and photon index of LS 5039 between 3-30 keV (Bosch-Ramon et al., 2005).

8th of October 2000 for ~ 2.2 hours. The observation covered the energy band between 0.1-10 keV.

The *Rossi X-Ray Timing Explorer* (RXTE) observations of RX J1826.2-1450/LS 5039 (Bosch-Ramon et al., 2005) are significant because of the detection of a possible orbital modulation in the X-ray flux. Observations took place over 17 runs between the 4th and 8th July 2003 with the flux lying between $(4.32^{+0.30}_{-0.41} - 6.95^{+0.29}_{-0.40}) \times 10^{-11}$ ergs cm⁻² sec⁻¹, and the photon index between $1.69^{+0.08}_{-0.08} - 2.18^{+0.14}_{-0.13}$ (Figure 1.12) for the energy band 3-30 keV

The authors reported on time variations in the X-ray flux when the data was folded with ~ 3.9 days (Casares et al., 2005). An orbital modulation and one hour "mini-flare" were found (Figure 1.13). The peak of the 3.9 day variation occurs at phase 0.8 just before periastron. The photon index also varies with the orbital period, hardening as the system approaches periastron. The authors found no evidence of the iron line reported by Ribó et al. (1999), and suggest that it may have originated from the Galactic ridge, observed due to the RXTE's wide field of view.

Bosch-Ramon et al. (2005) briefly considered a Bondi-Hoyle type accretion model (using $M_{opt} = 40 M_{\odot}$, $R_{opt} = 10 R_{\odot}$, $\dot{M}_{opt} = 1 \times 10^{-7} M_{\odot} \text{ yr}^{-1}$, $v_{\infty} = 2440 \text{ km s}^{-1}$, $\beta = 0.8$ and $M_X = 1.4 M_{\odot}$) to explain the X-ray luminosity and showed that the flux should vary by a factor of ≈ 10 , instead of the observed factor of ≈ 2 . This led them to suggest the presence of an accretion disc around the compact object that could smooth out the flux variation, though no line emission suggestive of an accretion disc was visible in the spectrum.

Table 1.7 shows X-ray and radio luminosities for 4 HMXBs. This shows that while the radio luminosity observed in LS 5039 is fairly typical, the X-ray luminosity is ~ 14 times less than observed from SS 433 and ~ 160 times less than observed from Cygnus X-1. The luminosity is consistent with LSI +61°303, one of the other known VHE gamma-ray emitters. This low X-ray luminosity combined with the VHE gamma-ray emission ($L_{\gamma} \sim 10^{34} \text{ erg s}^{-1}$) discussed in the

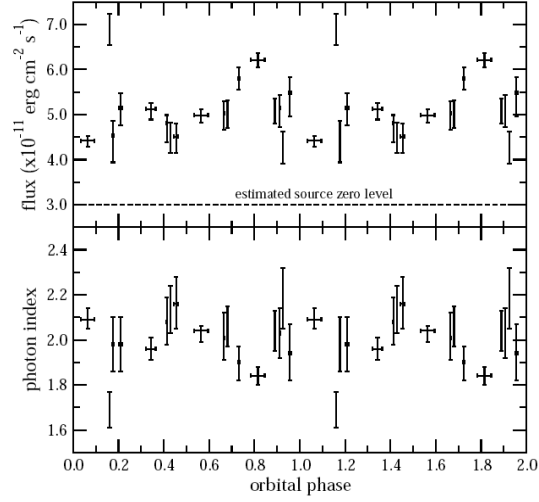


Figure 1.13: X-ray flux and photon index folded with the orbital period (Bosch-Ramon et al., 2005).

Table 1.7: Typical X-ray and radio luminosities and spectral indexes of some HMXBs. The values marked with an * are averages during quiescence (reproduced from Ribó et al. (1999)).

HMXB	L_X (1.5–12 keV) (erg s ⁻¹)	L_{rad} (0.1–100 GHz) (erg s ⁻¹)	α ($S_\nu \propto \nu^\alpha$)
LS 5039	$\sim 5 \times 10^{34}$	1.0×10^{31}	-0.5
Cygnus X-1	$\sim 8 \times 10^{36}$ (*)	1.1×10^{31}	0.1
LS I +61°303	$\sim 4 \times 10^{34}$	0.9×10^{31} (*)	-0.3(*)
SS 433	$\sim 7 \times 10^{35}$ (*)	3.2×10^{32} (*)	-0.7

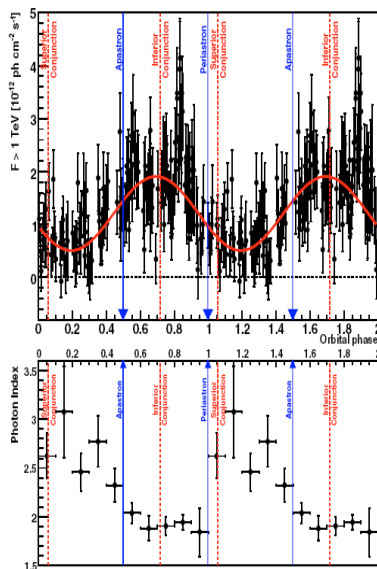


Figure 1.14: **Top** Gamma-ray flux above 1 TeV for LS 5039, folded with a 3.90603 day period. **Bottom** Fitted power law spectral index (Aharonian et al., 2006).

next section, is one of the reasons LS 5039 stands out as an extremely interesting HMXB source.

1.3.4 Gamma-ray

The original proposal that LS 5039 could be associated with the EGRET source 3EG J1824-1514 was made by Paredes et al. (2000). LS 5039 lies within the 95% confidence contour of the EGRET sources, and is the only X-ray emitter within 1° from the ROSAT All Sky Survey.

Subsequent observations of LS 5039 with the H.E.S.S. telescope in Namibia (Aharonian et al., 2006), revealed not only very high energy (VHE) gamma-ray emission from the system, but also found a 3.9 day modulation in the flux. Figure 1.14 shows the gamma-ray flux above 1 TeV and the spectral index folded with a 3.90603 day period (see Casares et al. (2005)) as observed by H.E.S.S.

The counts fluctuate between $(0.46 \pm 0.21 - 2.96 \pm 0.17) \times 10^{-12} \text{ ph cm}^{-2} \text{ s}^{-1} \text{ TeV}^{-1}$, and the spectral index between $1.84 \pm 0.25 - 3.08 \pm 0.47$ in anti-correlation to the luminosity.

The average luminosity is $7.8 \times 10^{33} \text{ erg s}^{-1}$, with a spectral index fit of 2.06 ± 0.05 , assuming the flux is fitted by the power law,

$$\frac{dN}{dE} = N E^{-\Gamma} \exp\left(\frac{-E}{E_0}\right).$$

The integrated flux over $0.45 < \phi \leq 0.9$ is $1.1 \times 10^{34} \text{ erg s}^{-1}$, with $\Gamma = 1.85 \pm 0.06$, and over $\phi \leq 0.45$ or $\phi > 0.9$ is $7.8 \times 10^{33} \text{ erg s}^{-1}$, with $\Gamma = 2.53 \pm 0.07$ (Figure 1.15). The maximum flux appears to occur around inferior conjunction ($\phi = 0.716$) and the flux minimum at $\phi \sim 0.2$

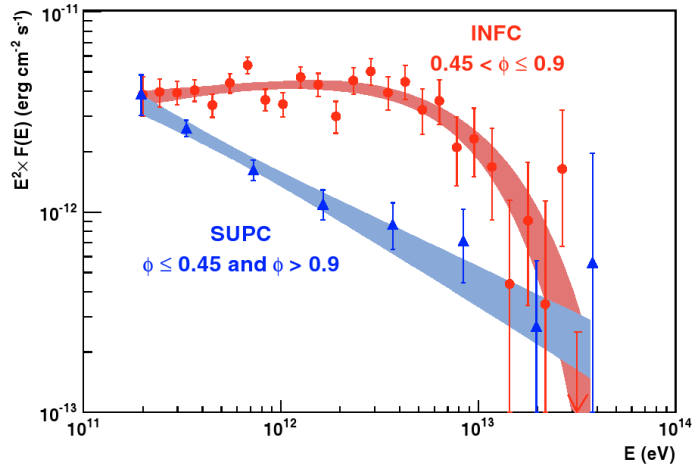


Figure 1.15: Integrated gamma-ray flux over **INFC** and **SUPC**. **INFC** = $0.45 < \phi \leq 0.9$ and **SUPC** = $\phi \leq 0.45$ or $\phi > 0.9$ (Aharonian et al., 2006).

(superior conjunction occurs at $\phi = 0.058$).

1.4 Motivation for this Study

While LS 5039 has been classed as a microquasar with compact jets, the spectral index of the radio jets is not flat nor inverted, having instead an index of $\alpha \sim -0.5$ (see e.g. Ribó et al. (1999)). The binary system is non-eclipsing, making any detection of a disc by photometry impossible. The system also shows no definitive pulses in the X-ray observations, while at the same time exhibiting no thermal disc or accretion related signature. While the radio jets appear to be non-aligned with the centre of the system, perhaps suggestive of disc warping, there are insufficient radio images to confirm the actual motion of the jets. The suggested velocity of the jet, $\sim 0.3c$ (Paredes et al., 2002), is made under the assumption that the asymmetry visible in the radio images is due to Doppler shifting effects (see Figure 1.2 and 1.16). Without additional radio interferometry, the motion of the jets is still questionable.

The reported mass of $3.7_{-1.0}^{+1.3} M_{\odot}$ for the compact object in LS 5039 (Casares et al., 2005) is made under the assumption that the system is pseudo-synchronized**. While it is believed that older systems will become synchronized the exact age of the system is unknown, since searches for the associated supernova remnant (SNR) have been unsuccessful (Ribó et al., 2002), and so it is unknown whether or not the system is old enough to have become pseudo-synchronized.

A recent paper by Dubus (2006b), proposed that the system is powered by a pulsar, and that the resulting synchrotron radiation is the result of a pulsar wind bow shock. He proposed that the radio images in LS 5039 were in fact the result of the shock front outflow mimicking jet-like

**A system is considered pseudo-synchronized if the orbital and rotational angular velocities of the optical star are “synchronized” at periastron.

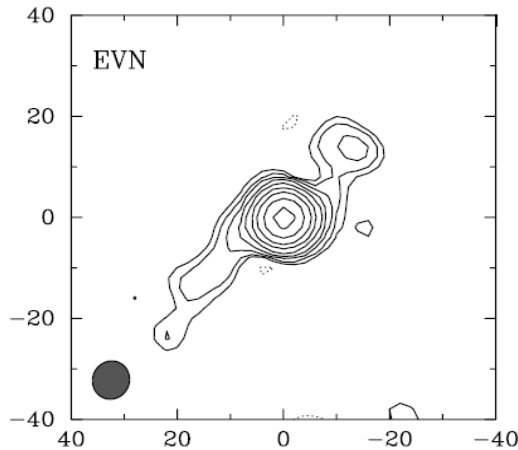


Figure 1.16: EVN image of LS 5039. The asymmetry of the radio jets is used to derive a speed of $0.3c$ for the jets (Paredes et al., 2002).

structures. While this scenario could explain the earlier radio images reported by Paredes et al. (2000) (see Figure 1.2), it is difficult to reconcile this model ($i \geq 60^\circ$) with the higher resolution images taken with the EVN array (Figure 1.16 (Paredes et al., 2002)). The jet formation, similar to that occurring in systems like the Crab Nebula and Vela pulsar was not considered in the paper.

LS 5039 has many unanswered questions that still need to be addressed. These include the method of producing the VHE gamma-ray luminosity yet fairly low X-ray luminosity, the modulation seen in the gamma-rays and, of particular importance, the nature of the compact object (neutron star or black hole). Despite the presence of radio “jet” structures, LS 5039 should not be automatically classified as a microquasar system. The three known very VHE gamma-ray binary systems are LS 5039, LSI +61°303 and PSR B1259-63, where PSR B1259-63 is a known pulsar system around a Be-type star (Aharonian et al., 2005). This suggests that a model other than an accretion driven microquasar model is required to explain LS 5039. Given the discrepancies in the system (e.g. low X-ray yet high gamma-ray luminosity), and the competing nature of the two models (microquasar or pulsar wind driven), the methodology followed in this study was to adopt a model independent approach, considering the system not as a microquasar or young pulsar, but simply looking at the system in terms of a compact object (NS or BH) orbiting an O-type giant and interacting with its stellar wind.

The rest of this study will be divided into four chapters. Chapter 2 will consider some aspects pertaining to HMXBs. This will include binary motion, accretion theory, compact object theory, and the evolution and observational properties of HMXBs. Chapter 3 will consider some aspects of the theory related to radiation mechanisms and material outflow, including possible jet formation. This will provide the foundation for the modelling that will be considered in Chapter 4. The final conclusions will be given in Chapter 5.

Chapter 2

High Mass Binary Systems

As was already mentioned, XRB systems are among some of the brightest X-ray sources in the sky. In general these systems are accretion driven, releasing the gravitational potential energy of accreted material in heat and radiation. Accretion is a field of study in itself, where concepts such as accretion discs and hot-spots need to be considered. Before discussing XRB and HMXB systems directly, the theory behind binary systems will be briefly reviewed.

2.1 Binary Systems

One of the initial challenges faced when studying binary systems is the determination of the system parameters, the main concern being the masses of the two objects. Not only do the masses determine the orbital parameters of the system (e.g. orbital separation and orbital period) but it is also an indication of the nature of the stellar objects. This is especially important in the case of compact objects that cannot be directly observed. The nature of these objects is determined from its implied mass, categorizing them as white dwarfs ($M \lesssim 1.43M_{\odot}$), neutron stars ($1.43M_{\odot} \lesssim M \lesssim 3M_{\odot}$) or black holes ($M \gtrsim 3M_{\odot}$)*. The theory behind binary motion and other relevant parameters is summarized in the next section.

2.1.1 The Two-Body Problem

Since the time of Johannes Kepler it has been known that the planets obey certain rules that dictate their motion. In 1687, Sir Isaac Newton showed that a gravitational inverse square law would satisfy these Keplerian requirements of orbital motion. This section will investigate the two-body system, discussing some relevant orbital formulae. The section will closely follow the discussion of Murray and Dermott in *Solar System Dynamics* (Murray and Dermott, 1999, Chp. 2).

*The $\sim 3M_{\odot}$ mass limit is based on the $3.2M_{\odot}$ NS mass limit proposed by Rhoades and Ruffini (1974).

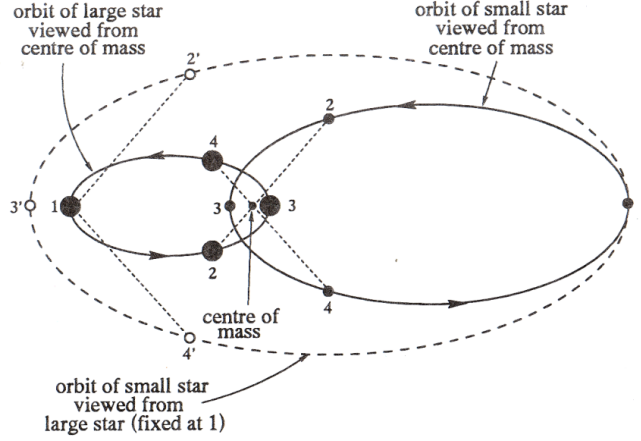


Figure 2.1: The orbit of a binary star system (Smits, 2002). The two masses follow elliptical paths around the centre of mass (the dark lines). The orbit of the smaller mass as seen by the larger (the dashed line) also follows an elliptical shape.

The three Keplerian requirements for orbital motion are:

1. The orbital motion must follow an elliptical shape, with the heavier object at one of the focus points.
2. A line joining the two objects sweeps out an area of equal size in a period of equal time.
3. The orbital period squared is proportional to the cube of the semi-major axis, $P^2 \propto a^3$.

These conditions can be satisfied mathematically by Newton's law of gravitational attraction

$$F_{grav} = \frac{GMm}{r^2},$$

where F_{grav} is the gravitational force between the objects, M and m are the masses of the two objects, defined such that $M > m$, r is the distance between the objects, and $G = 6.673 \times 10^{-8} \text{ cm}^3 \text{ g}^{-1} \text{ s}^{-1}$ is the Universal Gravitational Constant. Both masses orbit the centre of mass, following one of the four possible conics, namely the circle, ellipse, parabola or hyperbola. For two masses in a closed orbit, the orbital path will be an ellipse (or a circle in a special case) around the centre of mass (Figure 2.1). If the system is considered in a rest frame centred on one of the masses it can be shown that the resulting orbital separation also follows an elliptical shape, with the chosen mass at one focus point while the other focus point remains empty. For simplicity, the rest of this section (and study) will consider the system in the rest frame of the larger mass, M . The system is shown in Figure 2.2. The relation between the semi-major axis, a , and the semi-minor axis b is given by

$$b^2 = a^2(1 - e^2), \tag{2.1}$$

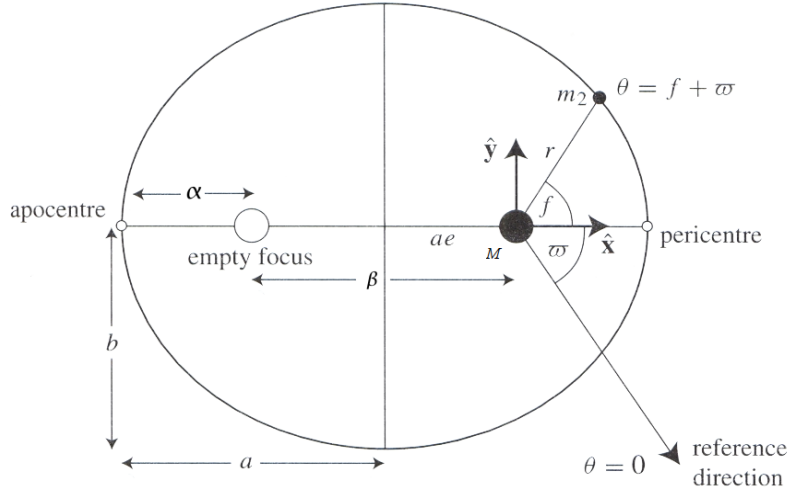


Figure 2.2: The orbital geometry of the two-body system. The larger mass, M , is centred at the one focus, while the smaller mass, m , follows the path of the ellipse. The semi-major axis is given by length a , and the semi-minor axis by b , (Murray and Dermott, 1999).

where e is defined as the eccentricity, the parameter which determines the shape of the orbit. The closer e is to 0, the closer the orbit approaches a circle, while the closer it is to 1 the more elliptical the orbit becomes. The orbit is a perfect circle in the case of $e = 0$, while in the case $e = 1$ the orbit is open[†], following a parabolic shape.

It is possible to determine the distance between the two objects at any point in the orbit. Since a closed orbit follows the path of the ellipse, the separation distance at any point is given by

$$r = \frac{a(1 - e^2)}{1 + e \cos f}, \quad (2.2)$$

where $f = \theta - \varpi$, is the true anomaly (See Figure 2.2 for the definitions of the angles).

This can be simplified when determining the special cases of the closest and furthest approach. Since the distance to the centre of the ellipse from either focus point is given by ae , it follows that the distance from the focus to the pericentre (the closest point of approach) can be defined as

$$\alpha = a(1 - e), \quad (2.3)$$

and the distance to the apocentre (the furthest point) as

$$\beta = a(1 + e). \quad (2.4)$$

[†]An open orbit is one that will not repeat its orbital path, instead it comes from infinity, curves around the object and returns to infinity.

The orbital period of the system is given by

$$P^2 = \frac{4\pi^2 a^3}{G(M+m)}, \quad (2.5)$$

while the velocity of m along the orbit is determined by

$$v^2 = G(M+m) \left(\frac{2}{r} - \frac{1}{a} \right).$$

In the special cases of periastron and apastron passage the velocities are

$$v_p = \Omega a \sqrt{\frac{1+e}{1-e}} \quad (2.6)$$

and

$$v_a = \Omega a \sqrt{\frac{1-e}{1+e}} \quad (2.7)$$

respectively, where Ω is the orbital frequency, defined as

$$\Omega = \frac{2\pi}{P}.$$

The determination of the orbital parameters in binary systems with a compact object is especially difficult since the property of only one star, the optical star, is easily observable. The mass function is extremely useful in these cases since it can be determined observationally through spectroscopy. The mass function is given by (e.g. Frank et al. (1992, pg. 168))

$$f(M) = \frac{(M_O \sin i)^3}{(M_X + M_O)^2} \quad (2.8)$$

where the mass of the compact object, M_X , can readily be determined through spectroscopy for a given inclination angle i , i.e. the angle between the line of sight and the normal to the orbital plane.

The equations above allow us to determine the most important parameters for any Newtonian system. Since the binary system in question, LS 5039, has a binary separation much larger than the Schwarzschild radius, it will obey Newtonian/Keplerian rules. Therefore it is not necessary to consider the more complicated theory of General Relativity.

2.1.2 Orbital Diagram

For the sake of clarity this section will briefly explain some of the terms that will be used in this dissertation.

The orbital phase (Figure 2.3)

$$\phi = \left(\frac{t_i - t_0}{P_{orb}} \right),$$

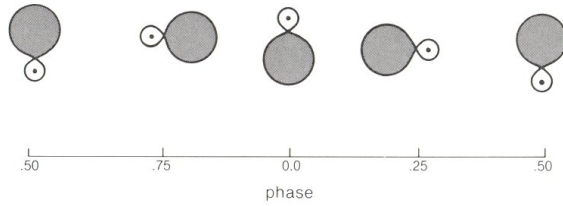


Figure 2.3: Orbital phase of an X-ray binary (Bowers and Deeming, 1984, p. 332). Phase 0/1 is normally defined as the point half way through the eclipse of the compact object.

Table 2.1: Astronomical Units.

Name	Symbol	Units
Astronomical unit	AU	1.496×10^{13} cm
Parsec	pc	3.086×10^{18} cm
Solar mass	M_{\odot}	1.989×10^{33} g
Solar radius	R_{\odot}	6.960×10^{10} cm
Solar luminosity	L_{\odot}	3.827×10^{33} erg s ⁻¹
Solar Temperature	T_{\odot}	5.780×10^3 K

is a dimensionless measure of the orbital position of an orbiting light source (usually the bright main sequence giant in HMXBs) and $\phi \in [0, 1]$. Here $\phi = 0, 1$ is usually defined as the point half way through the eclipse of the compact object.

Periastron is the distance of minimum separation and *apastron* is the distance of maximum separation during the the orbital period.

The inclination angle is defined as the angle between the line of sight and the normal to the orbital plane. In other words a binary system with an inclination of 0° is observed face on, while a system with an inclination of 90° is observed edge on.

Certain parameters will be given in terms of solar units. For example a $M = 10 M_{\odot}$ star has a mass 10 times that of the sun. Table 2.1 lists some relevant values with their units.

2.2 Accretion

Mass transfer and accretion is a fundamental process in HMXBs and binary systems in general. The accretion is not only important for powering the emission seen in XRBs, but plays an important role in the evolution of binary systems. In these systems, accretion occurs through either Roche lobe overflow or from the stellar wind. In either case accretion onto a compact object releases a large amount of energy (see Equation 1.1). This section will look at the accretion process, first considering the Roche lobe overflow and wind accretion scenarios before focusing on accretion discs and magnetically funneled accretion onto the compact object. This section

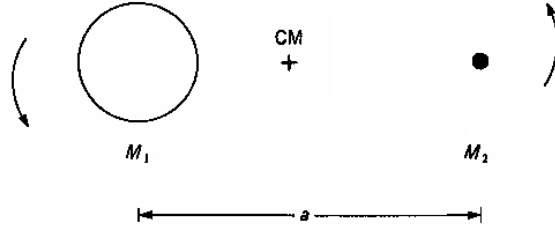


Figure 2.4: Binary system consisting of two stars of mass M_1 and M_2 such that $M_1 > M_2$. In HMXBs the compact object is less massive than that the optical companion (Frank, King, and Raine, 1992).

will closely follow the discussions of Frank, King, and Raine (1992, Chp. 4 & 5) & Lewin, van Paradijs, and van den Heuvel (1995, Chp. 11).

2.2.1 Roche Lobe Overflow

The Roche lobe derives its name from Edouard Roche, a French mathematician, and stems from his work into the motion of planetary satellites. Applied to mass transfer and accretion in a binary system, three simplifications are introduced, namely:

1. It is assumed the mass of the test object is negligible, whose motion is influenced mainly by the two dominant masses in the binary system, while not influencing their motion in return,
2. The masses of the binary system are considered to be point masses, and
3. It is assumed that the binary has a circular orbit, with both objects orbiting a common centre of mass (e.g. Figure 2.4).

In a rotating reference frame the potential experienced by a test particle is given by (e.g. Frank, King, and Raine (1992, p. 48))

$$\Phi_R(\mathbf{r}) = -\frac{GM_1}{|\mathbf{r} - \mathbf{r}_1|} - \frac{GM_2}{|\mathbf{r} - \mathbf{r}_2|} - \frac{1}{2}(\boldsymbol{\Omega} \times \mathbf{r})^2, \quad (2.9)$$

where the dominant gravitating masses are written in terms of M_1 and M_2 such that $M_1 > M_2$. Here \mathbf{r} , \mathbf{r}_1 and \mathbf{r}_2 are the distance vectors from the centre of mass to a test point, and to the centre of M_1 and M_2 respectively, and $\boldsymbol{\Omega}$ is the angular velocity of the system,

$$\boldsymbol{\Omega} = \left[\frac{G(M_1 + M_2)}{a^3} \right]^{1/2} \mathbf{e},$$

where \mathbf{e} is a unit vector normal to the orbital plane. The first two terms in the equation are the gravitational potentials of the two masses, while the last term represents the centrifugal effect as a result of the orbital motion. Figure 2.5 shows this equation sketched for a mass ratio

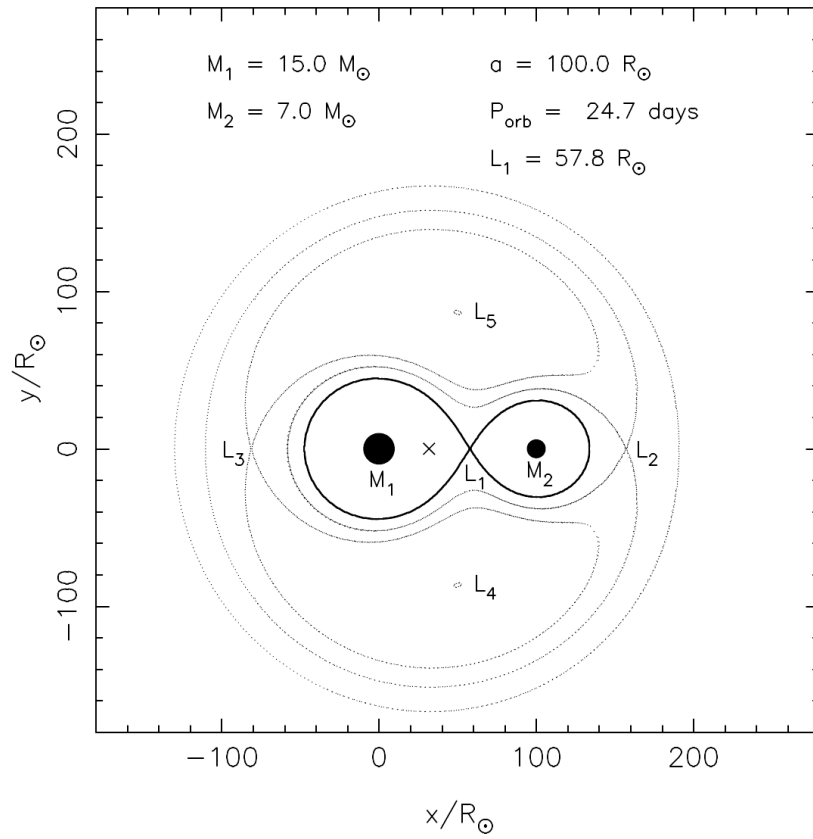


Figure 2.5: Roche lobe of a binary star system. $L_1 - L_5$ are the various Lagrange points where the effective gravity is zero (Tauris and van den Heuvel, 2003).

$q = M_1/M_2 = 15/7^\ddagger$. The most important feature of the sketch is the bold “figure 8” line surrounding the two masses, particularly the point where the lines intersect, known as the first Lagrange point[§], L_1 . If during the evolution of the system one of the stars fills its Roche lobe, the connection of the potential wells at the L_1 point allows material to be easily transferred from the star onto its companion due to the thermal motion of the gas in the photosphere of the star. In most HMXBs, a compact object (NS or BH) accretes material from a main sequence star that fills its Roche lobe. Roche lobe overflow can also occur in the case where both stars in the binary system are main sequence stars as will be discussed later in the case of HMXB evolution (Section 2.5).

The average distance to the L_1 point as shown by Eggleton (1983) is

$$R_{L_1} = \frac{0.49a}{0.6 + q^{-2/3} \ln(1 + q^{1/3})}, \quad (2.10)$$

correct for all q to within 1%, or by Paczyński (1967)

$$R_{L_1} = \frac{2}{3^{4/3}} a \left(\frac{M_1}{M_1 + M_2} \right)^{1/3}$$

which is correct to within 2% for $q \lesssim 0.8$. The mass flow is then determined by the extent to which the main sequence star fills its Roche lobe.

Mass transfer will result in a change of the system parameters since accretion increases the mass of the accreting star and decreases the mass of the donor star. In order to see how this will effect the system it is necessary to consider the orbital angular momentum. The angular momentum of the system is written as

$$J = (m_1 a_1^2 + m_2 a_2^2) M_\odot \Omega, \quad (2.11)$$

where $m_1 = M_1/M_\odot$ and $m_2 = M_2/M_\odot$, and a_1 and a_2 are the distances from the centre of M_1 and M_2 to the centre of mass respectively. These are given by

$$a_1 = \left(\frac{m_2}{m_1 + m_2} \right) a$$

and

$$a_2 = \left(\frac{m_1}{m_1 + m_2} \right) a.$$

[‡]The mass ratio q represents the ratio of the masses of the Roche lobe filling star and compact object, i.e. $q = M_1/M_2$ for HMXBs and $q = M_2/M_1$ in LMXBs.

[§]The Lagrange points are the positions where test masses will remain stationary with respect to the co-rotating reference frame. They are in effect the positions where the force due to gravity and the centrifugal force balance, i.e. where the effective gravity is zero.

Substituting these values into Equation 2.11, and simplifying the expression gives

$$J = \frac{a^2}{(m_1 + m_2)^2} m_1 m_2 M_\odot \Omega. \quad (2.12)$$

This can be simplified further by re-writing the orbital period (Equation 2.5) in terms of the angular velocity,

$$\begin{aligned} \frac{2\pi}{P} &= \Omega \\ &= \frac{(G(m_1 + m_2)M_\odot)^{1/2}}{a^{3/2}}. \end{aligned}$$

Substituting this expression into Equation 2.12 gives

$$J = m_1 m_2 \left(\frac{Ga}{m_1 + m_2} \right)^{1/2} M_\odot^{3/2}.$$

Logarithmic differentiation (with respect to time) of the above equation results in

$$\frac{\dot{a}}{a} = \frac{2\dot{J}}{J} - 2\frac{\dot{m}_1}{m_1} - 2\frac{\dot{m}_2}{m_2}.$$

For conservative mass transfer it is assumed that both angular momentum and mass are conserved within the system such that $\dot{J} = 0$ and $\dot{m}_1 + \dot{m}_2 = 0$. For mass conservation this implies that $\dot{m}_1 = -\dot{m}_2$ and the above equation simplifies to

$$\frac{\dot{a}}{a} = \frac{2\dot{J}}{J} + \frac{2(-\dot{m}_2)}{m_2} \left(1 - \frac{m_2}{m_1} \right). \quad (2.13)$$

Applying the conservation of angular momentum ($\dot{J} = 0$) then simplifies the equation further to

$$\frac{\dot{a}}{a} = \frac{2(-\dot{m}_2)}{m_2} \left(1 - \frac{m_2}{m_1} \right). \quad (2.14)$$

In the case of HMXBs, $\dot{m}_2 > 0$, implying that $\dot{a} < 0$. This results in the binary separation shrinking. This contraction of the binary system will move the mass donor closer to the centre of mass and will keep it filling its Roche lobe. As a result the Roche lobe overflow will be a sustained process for HMXBs. This is not true in LMXBs, where $\dot{m}_2 < 0$, which implies that $\dot{a} > 0$ and results in the binary system expanding. Accretion continues to occur in LMXBs due to the expansion of the optical mass donor. The constant entropy profile found in low mass stars (as would be found in LMXBs) results in an expansion of the star on the dynamic timescale once material is removed from the outer convective envelope (e.g. Hjellming and Webbink (1987); King (1988)).

The orbital and mass transfer evolution will be significantly altered for binary systems in the case where the mass transfer process is non-conservative ($\dot{J} < 0$), i.e. where significant angular momentum and mass loss ($\dot{m} < 0$) mechanisms exist in the system. Not all material that crosses the L_1 point may be accreted onto the accreting star. Material may in fact be ejected from the system by the propeller effect as occurs in systems such as AE Aquarii (Meintjes and de Jager, 2000). The amount of angular momentum lost through the L_1 point is given by (King, 1993; Wynn and King, 1995)

$$\frac{\dot{J}_{loss}}{J_{orb}} = \eta \frac{\dot{J}_{ov}}{J_{orb}} = \eta \dot{M}_2 \frac{(GM_1 R_{circ})^{1/2}}{J_{orb}},$$

where η is the fraction of angular momentum lost and \dot{J}_{ov} is the rate at which angular momentum is lost due to the transfer of material. The total amount of angular momentum loss must also take into account momentum lost through e.g. the stellar wind, magnetic braking and gravitational radiation,

$$\frac{\dot{J}}{J} = \frac{\dot{J}_{loss}}{J_{orb}} + \left(\frac{\dot{J}_{wind}}{J_{orb}} + \frac{\dot{J}_{mb}}{J_{orb}} + \frac{\dot{J}_{gr}}{J_{orb}} + K \right),$$

where K is any other potential angular momentum loss mechanism (see for example Meintjes (2002) and references therein).

Since angular momentum loss implies $\dot{J} < 0$, this would result in a more rapid decrease in the size of the binary separation in HMXBs. In LMXBs the mass ratio $q = \frac{M_2}{M_1}$, determines whether the first or second term dominates in Equation 2.13. Hence, depending on q , the system may either expand or contract.

2.2.2 Wind Accretion

If the binary separation in a system is too large, neither star will fill its Roche lobe. In this case *wind accretion* can still occur (see for e.g. Bondi and Hoyle (1944)). The scenario that arises is shown in Figure 2.6. Wind accretion occurs if material in the stellar wind passes too close to the compact object so that the absolute value of the gravitational potential energy exceeds the kinetic energy. This will occur in a volume that is approximated by a cylinder with a radius roughly defined as

$$r_{acc} \sim \frac{2GM_{acc}}{v_{rel}^2}, \quad (2.15)$$

where M_{acc} is the mass of the wind accreting object and v_{rel} is the relative wind speed. The magnitude of the relative wind speed is determined by the speed of the wind, v_w and the orbital speed of the accreting object, v_n , i.e.

$$v_{rel} \cong (v_n^2 + v_w^2)^{1/2}.$$

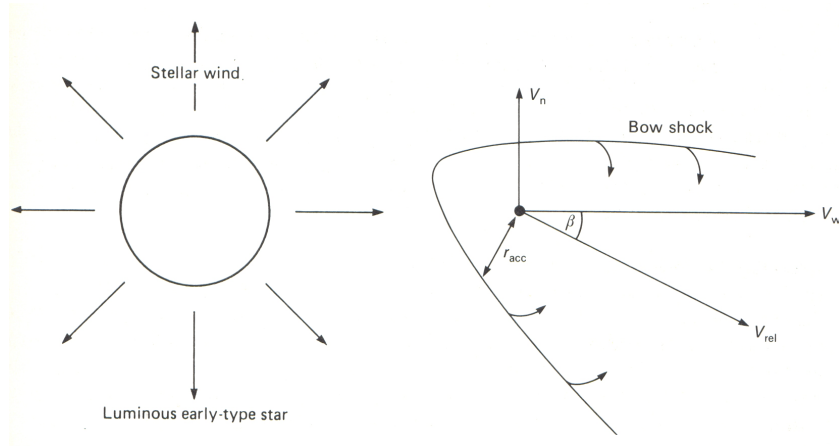


Figure 2.6: The compact star in a binary system accretes material from the stellar wind of the mass donor. This results in the formation of a bow shock around the compact object (adopted from Frank et al. (1992)).

The simplest estimate for the wind speed can be approximated by considering the escape velocity as a lower limit. This is given by

$$v_{esc}(R_{don}) = \left(\frac{2GM_{don}}{R_{don}} \right)^{1/2}, \quad (2.16)$$

where R_{don} is the radius of the mass donor. The wind speed can also be estimated by considering the wind velocity at infinity, v_∞ , approximately 2440 km s^{-1} in the case of LS 5039 (McSwain et al., 2004). The cylindrical accretion radius, r_{acc} , can be considered as a very rough parameter since material will not be captured in a cylinder but in the wake of a bow shock that will form around the accreting object (Figure 2.6).

In the simplified case that $v_w \gg v_n$, $v_{rel} \approx v_w$, and the angle β in Figure 2.6 equals zero. The mass flow from the wind of the optical mass donor can be approximated as

$$\begin{aligned} -\dot{M}_w &= \rho A_{sph} v_w \\ &= \rho 4\pi d^2 v_w, \end{aligned}$$

where A_{sph} is the area of a sphere, ρ is the density and d is the binary separation. The rate at which material enters the gravitational well surrounding the compact object is then

$$\begin{aligned} \dot{M} &= \rho A_{cap} v_w \\ &= \rho \pi r_{acc}^2 v_w, \end{aligned}$$

where A_{cap} is the area of the cap of the cylinder. An estimate of the fraction of the material

that is captured from the stellar wind is then given by

$$\frac{\dot{M}}{-\dot{M}_w} \cong \frac{\pi r_{acc}^2 v_w}{4\pi d^2 v_w} = \frac{G^2 M_{acc}^2}{d^2 v_w^4}, \quad (2.17)$$

where r_{acc} is given by Equation 2.15. This can be further simplified if we consider the more general case where the wind speed is estimated by the escape velocity (Equation 2.16),

$$\frac{\dot{M}}{-\dot{M}_w} \cong \frac{1}{4} \left(\frac{M_{acc}}{M_{don}} \right)^2 \left(\frac{R_{don}}{d} \right)^2.$$

These equations allow for an estimate of the amount of material that can be captured by the gravitational well of a star in the wind of its companion.

The mass donors in wind accretion systems do not fill their Roche lobes, but the gravitational potential of the accreting star may cause the stellar wind of the mass donor to be preferentially directed towards it (Friend and Castor, 1982). This could result in a higher mass transfer rate than predicted above, since the model assumes a spherical wind outflow from the mass donor.

2.2.3 Disc Accretion

Accretion discs in binary systems provide a mechanism for removing angular momentum during mass transfer, hence facilitating the accretion of matter. This is especially true when accretion occurs through Roche lobe overflow since the material still possesses a large amount of angular momentum. The question of accretion disc formation during wind accretion is more difficult since it is dependent on the specific angular momentum[¶] of the material when entering the accretion radius (Equation 2.15). A detailed discussion of the formation and evolution of accretion discs is beyond the scope of this study.

The discussion will follow a general approach to the formation and properties of accretion discs, not specific to X-ray binaries. The purpose is only to point out some important aspects of the theory. For details on disc formation see for example Choudhuri (1998, pp. 94-102) & Frank, King, and Raine (1992, Chp. 5) for Roche lobe filling systems, and Davies and Pringle (1980) & Shapiro and Lightman (1976) for wind accretion systems.

When material passes through the L_1 point it can possess too much angular momentum to accrete directly onto the surface of the accreting object. By way of an example the specific angular momentum of material crossing the L_1 point can be approximated by

$$l \sim r^2 \Omega = \frac{2\pi r^2}{P}.$$

In the case of LS 5039 the distance to the L_1 point by means of the Eggleton approximation is

[¶]Specific angular momentum is the angular momentum per unit mass: $l = J/m$.

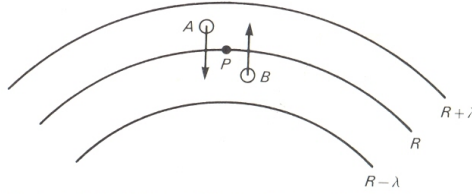


Figure 2.7: Viscous flow in an accretion disc (Frank, King, and Raine, 1992). The figure shows material moving between different velocity layers.

$R_{L_1} \approx 1.1 \times 10^{12}$ cm, which for an orbital period of 3.9 days gives

$$l \sim 2.3 \times 10^{19} \text{ cm}^2 \text{ s}^{-1}.$$

This is a huge specific angular momentum load which needs to be shed before the material can accrete onto the compact object and is similar to the angular momentum at the L_1 point in SS 433, and is much larger than in Cataclysmic Variables such as AE Aqr ($\sim 7 \times 10^{17} \text{ cm}^2 \text{ s}^{-1}$).

For a normal Roche lobe overflow scenario, once this material crosses the L_1 point, subjected to an additional Coriolis effect, it is usually deflected past the compact object, eventually settling in a ring at the so-called circularization radius R_{circ} . The circularization radius is the radius at which a Keplerian orbit has the same specific angular momentum as the material when it crosses the L_1 point. This can be approximated by (e.g. Frank, King, and Raine (1992, p. 56))

$$R_{circ} = a(1+q)(0.500 - 0.227 \log q)^4.$$

For a gravity dominated flow this material follows a circular Keplerian orbit. In the rotating frame of the orbiting fluid the centrifugal effect is balanced by gravity resulting in

$$\begin{aligned} \frac{GM_* m}{R^2} &= \frac{mv_\phi^2}{R} \\ \therefore v_\phi^2 &= \frac{GM_*}{R} \\ &= (R\Omega)^2. \end{aligned}$$

The Keplerian orbital frequency is thus given by

$$\Omega = \left(\frac{GM}{R^3} \right)^{1/2}, \quad (2.18)$$

resulting in a $\Omega \sim R^{-3/2}$ differential velocity profile. This means that material closer to the accreting object rotates faster than material further away. As a result the ring consists of different velocity layers (Figure 2.7) with a thickness $\sim \lambda$, the collisional mean free path. These layers will interact by means of thermal material transfer between the different layers; for example

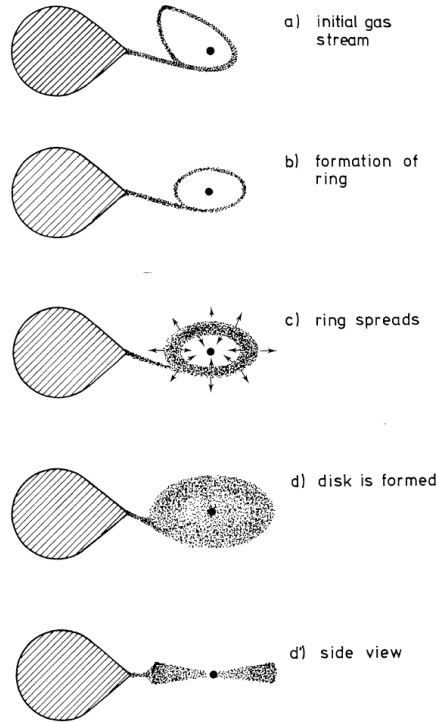


Figure 2.8: Formation of an accretion disc (Verbunt, 1982).

material can flow from B to A and vice versa. This occurs when material at B possesses an angular momentum which is characteristic of the angular momentum in the layer containing A . The material transfer between the layers occurs with the characteristic thermal speed of the particles, $\sim \tilde{v} \approx \sqrt{\frac{kT}{m}}$. This transport of angular momentum, through the motion of material, creates viscous torque. It is possible to show that the magnitude of the torque per unit area is (see for example Choudhuri (1998, p. 98))

$$G(R) = 2\pi\nu\Sigma R^3 \frac{d\Omega}{dR},$$

where $\Sigma = \rho H$ is the surface density, $\nu = \lambda\tilde{v}$ is the kinematic viscosity, and $d\Omega/dR$ is the change in the Keplerian orbital frequency with respect to radius. The viscous momentum transfer results in the ring spreading out into a disc (Figure 2.8). Viscosity can be driven by thermal motion on a microscopic scale (ineffective) or turbulence on a larger scale (Balbus-Hawley instability; see for example Hawley and Balbus (1991)). The material that loses angular momentum spirals inwards, eventually accreting onto the surface of the stellar object, while the material that gains angular momentum moves outwards to higher Keplerian orbits.

Consider the layer of material in Figure 2.9 between R and $R + dR$. It will experience a net

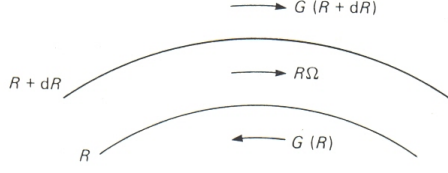


Figure 2.9: Differential viscous torque in accretion discs (Frank, King, and Raine, 1992).

torque

$$G(R + dR) - G(R) = \frac{\partial G}{\partial R} dR.$$

The rate of work done by the torque is then

$$\Omega \frac{\partial G}{\partial R} dR = \left[\frac{\partial}{\partial R} (G\Omega) - G \frac{\partial \Omega}{\partial R} \right] dR.$$

While the first term in this equation represents the total motion of rotational energy through the whole disc, the second term represents the energy that is lost from the disc at a local point. This energy dissipates away from the disc in the form of thermal and radiative energy. The dissipation rate per unit area is then

$$D(R) = \frac{G\Omega' dR}{4\pi R dR} = \frac{1}{2} \nu \Sigma (R\Omega')^2, \quad (2.19)$$

where $\Omega' = \partial\Omega/\partial R$.

It is possible to determine the dissipation rate $D(R)$ in terms of the accretion rate of material. The inflow of material in an accretion disc of height h will be

$$\begin{aligned} d\dot{M} &= \rho(-v_R) dA \\ \Rightarrow \dot{M} &= -2\pi R v_R \int_0^h \rho dh \\ &= -2\pi v_R \Sigma. \end{aligned} \quad (2.20)$$

If the accretion disc is considered as a gas governed by the time independent Navier-Stokes equations, then the equations governing the accretion disc are (e.g. Choudhuri (1998, p. 97))

$$\frac{1}{R} \frac{\partial}{\partial R} (R\Sigma v_R) = 0 \quad (2.21)$$

$$\frac{1}{R} \frac{\partial}{\partial R} (\Sigma R^3 \Omega v_R) = \frac{1}{R} \frac{\partial}{\partial R} \left(\nu \Sigma R^3 \frac{d\Omega}{dR} \right). \quad (2.22)$$

For the steady state condition the solution of Equation 2.22 has the form

$$\Sigma R^3 \Omega v_R - \nu \Sigma R^3 \frac{d\Omega}{dR} = C \quad (2.23)$$

where C is an integration constant. This can be solved by considering that close to the surface of the accreting star the material is in rigid rotation $d\Omega/dR = 0$, therefore

$$\begin{aligned} C &= \Sigma R_*^3 \Omega(R_*) \nu_R \\ &= -\frac{\dot{M}_*}{2\pi} (GM R_*)^{1/2}. \end{aligned} \quad (2.24)$$

Substituting this solution into Equation 2.23 and re-ordering gives

$$\nu \Sigma = -\frac{\dot{M}}{3\pi} \left[1 - \left(\frac{R_*}{R} \right)^{1/2} \right].$$

This shows that the mass inflow and eventual accretion rate depends on the disc viscosity, ν . Substituting this into Equation 2.19 and considering a Keplerian orbital frequency (Equation 2.18) gives the dissipation rate

$$D(R) = \frac{3GM\dot{M}}{8\pi R^3} \left[1 - \left(\frac{R_*}{R} \right)^{1/2} \right].$$

Each region of the accretion disc can be considered as a black body emitter with each face having a temperature $T(R)$ such that

$$\sigma T^4(R) = D(R).$$

Substituting the dissipation rate into the black body equation gives

$$T(R) = \left\{ \frac{3GM\dot{M}}{8\pi R^3 \sigma} \left[1 - \left(\frac{R_*}{R} \right)^{1/2} \right] \right\}^{1/4}, \quad (2.25)$$

which reduces to

$$T = T_* \left(\frac{R}{R_*} \right)^{-3/4},$$

in the case of $R \gg R_*$, and where

$$T_* = \left(\frac{3GM\dot{M}}{8\pi R_*^3 \sigma} \right)^{1/4}. \quad (2.26)$$

A rough estimate of the emitted spectrum can be made by assuming the disc radiates as a black body emitter with a typical Planck spectrum (e.g. Frank, King, and Raine (1992, p. 78))

$$I_\nu = B_\nu[T(R)] = \frac{2h\nu^3}{c^2(e^{h\nu/kT(R)} - 1)} \text{ erg s}^{-1} \text{ cm}^{-2} \text{ Hz}^{-1} \text{ sr}^{-1}. \quad (2.27)$$

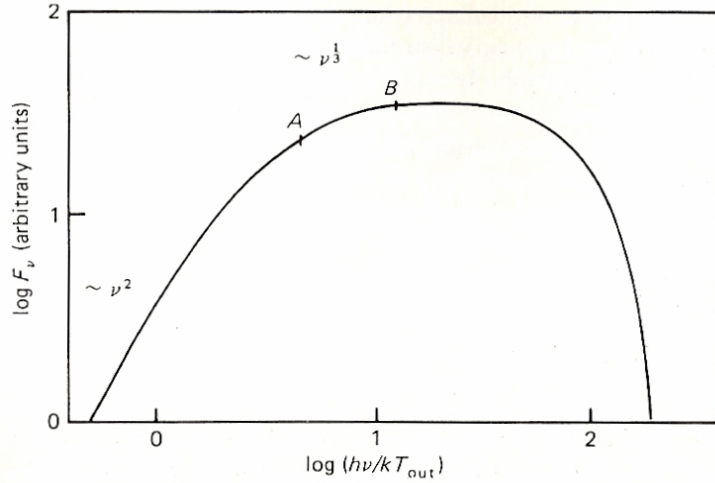


Figure 2.10: An example of a black body spectrum emitted by a disc (Equation 2.28) for $R_{out} = 250R_*$ and $T_{out} = T(R_{out})$ (Frank, King, and Raine, 1992).

The resultant flux is then

$$F_\nu = \frac{2\pi \cos i}{d_{obs}^2} \int_{R_*}^{R_{out}} I_\nu R dR,$$

where d_{obs} is the distance from an observer to the source at an inclination angle, i . Substituting Equation 2.27 into the above expression gives

$$F_\nu = \frac{4\pi h \nu^3 \cos i}{c^2 d_{obs}^2} \int_{R_*}^{R_{out}} \frac{R dR}{e^{h\nu/kT(R)} - 1}. \quad (2.28)$$

Figure 2.10 shows an example of the expected black body emission from a disc using Equation 2.28. For frequencies $\nu \ll kT(R_{out})/h$, the Planck function takes on the Rayleigh-Jeans form $2kT\nu^2/c^2$, hence (Figure 2.10)

$$F_\nu \propto \nu^2.$$

For intermediate frequencies, $kT(R_{out})/h \ll \nu \ll kT(R_*)/h$, the flux scales like (Figure 2.10)

$$F_\nu \propto \nu^{1/3},$$

which characterizes a typical disc spectrum (typically blue for standard accretion disc temperatures). It is important to note that Equation 2.28 ignores any disc corona or atmosphere that could change the shape of the observed spectrum.

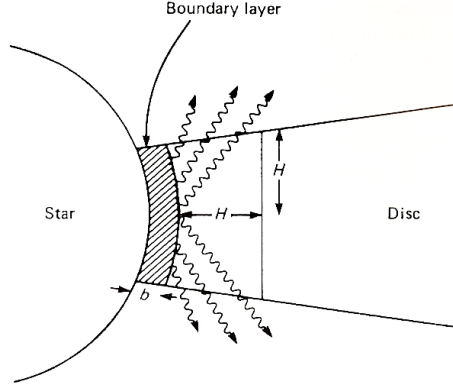


Figure 2.11: Boundary layer that can form close to the surface of a accreting non-magnetized star (Frank, King, and Raine, 1992).

2.2.4 Accretion onto a Compact Object

Since the specific angular momentum in a Keplerian disc, $l = (GMr)^{1/2}$, i.e. $j \propto r^{1/2}$, the accretion of matter onto a compact object is usually associated with substantial angular momentum loss. This accretion process will be hindered if the compact object possesses a fast rotating magnetic field which creates a centrifugal barrier that inhibits the inward accretion flow. This may well be the driving mechanism behind magnetospheric propelling, which forms the basis of disc outflow in the microquasar and pulsar winds in NS binaries. This section focuses on disc accretion of material onto a compact object.

Boundary Layer

If the compact object in a binary system has a low enough magnetic field and spin velocity, an accretion disc can form right up to the surface of the star. In these cases, if the accretion rate is high enough, an optically thick region called the boundary layer can form at the inner edge of the disc (Figure 2.11). This region has an area of $\sim 2 \times 2\pi R_* H$, where H is the height of the emitting region with a luminosity of

$$\frac{1}{2}L_{acc} = \frac{GM\dot{M}}{2R_*}.$$

As a result of the viscous dissipation rate, $(D(r) = \sigma T^4)$ near the boundary layer, this region then becomes a black body emitter with a characteristic temperature, T_{BL} , given by

$$2 \times 2\pi R_* H D(R) \approx 4\pi R_* H \sigma T_{BL}^4$$

resulting in

$$4\pi R_* H \sigma T_{BL}^4 \sim \frac{GM\dot{M}}{2R_*},$$

where R_* is the radius of the accreting star and σ is the Stefan-Boltzman constant. Comparison with the temperature of the accretion disc (Equation 2.26) shows that the temperature in the boundary layer can be written as

$$\begin{aligned} T_{BL}^4 &\sim \frac{GM\dot{M}}{8\pi R_*^2 \sigma H} \\ &= \left(\frac{3GM\dot{M}}{8\pi R_*^3 \sigma} \right) \frac{R_*}{3H} \\ \Rightarrow T_{BL} &\sim \left(\frac{R_*}{3H} \right)^{1/4} T_* \end{aligned}$$

This gives an indication of the expected black body emission from the boundary layer.

Magnetized Compact Object

In the case of accretion onto a sufficiently magnetized source, the strong magnetic field disrupts the inflow of material. If the magnetic field strength becomes high enough, the inflowing accreting material is channeled along the field lines. In some of these systems the material can be forced to flow along the field lines and accrete onto the poles (see e.g. Pringle and Rees (1972)). In the case of systems where an accretion disc is present, the inner-edge of the disc can become “warped” by the effect of the magnetic field.

An important parameter when considering accretion onto a magnetized compact object is the Alfvén radius, defined as the position where the magnetic pressure of the compact object balances the ram (and gas) pressure of the accretion flow. For a dipolar field configuration

$$B(r) \sim B_* \left(\frac{R_*}{r} \right)^3 \sim \frac{\mu}{r^3}, \quad (2.29)$$

where B_* is the magnetic field at the surface of the star and $\mu = B_* R_*^3$, the magnetic dipole moment. The resulting pressure is then

$$P_{mag} = \frac{B^2}{8\pi} = \frac{B_*^2 R_*^6}{8\pi r^6} = \frac{\mu^2}{8\pi r^6}.$$

For radial inflow, this magnetic pressure will eventually match the dominant ram pressure associated with the accreting gas. If it is assumed that the gas pressure is negligible, the Alfvén radius can be approximated by the position where

$$P_{mag}(r_{Alf}) = \rho v^2|_{r_{Alf}}, \quad (2.30)$$

where ρ is the density of the material and v is its velocity. For gas accreting along the field lines

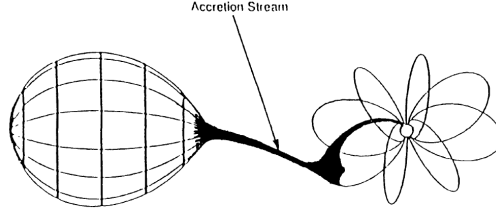


Figure 2.12: Accreting material is channeled to the poles of magnetized compact objects (adopted from Cropper (1990)).

the inflow speed will approach the free-fall speed, i.e.

$$v_{ff} = \left(\frac{2GM}{r} \right)^{1/2}.$$

If the inflow of material is approximately spherical, the momentum flux associated with the flow is

$$|\rho v| = \frac{\dot{M}}{4\pi r^2},$$

where \dot{M} is the inflow rate. Equilibrium between magnetic and ram pressures results in

$$\begin{aligned} P_{mag}(r_{Alf}) &= |\rho v|_{r_{Alf}} \times v \\ \frac{B_*^2 R_*^6}{8\pi r_{Alf}^6} &= \frac{\dot{M}}{4\pi r_{Alf}^2} \left(\frac{2GM}{r_{Alf}} \right)^{1/2} \\ &= \frac{(2GM)^{1/2} \dot{M}}{4\pi r_{Alf}^{5/2}}. \end{aligned}$$

From this equation the Alfvén radius is determined, i.e.

$$r_{Alf} = 5.1 \times 10^8 \left(\frac{\dot{M}}{10^{16} \text{ g s}^{-1}} \right)^{-2/7} \left(\frac{M_1}{M_\odot} \right)^{-1/7} \left(\frac{\mu}{10^{30} \text{ G cm}^3} \right)^{4/7} \text{ cm}. \quad (2.31)$$

The Alfvén radius is very important since any material that crosses it becomes controlled by the magnetic field of the compact object. Since the material at this stage is highly ionized and attached to the field lines through the Lorentz force ($F_L \propto v \times B/c$), the rotational velocity of the field will have a profound influence on the accretion process. This will be discussed later.

Accretion Column

Once ionized material crosses the Alfvén radius it is channeled by the magnetic field lines and must flow along them (Figure 2.12) to the poles of the compact object, creating accretion columns or accretion arcs. The accretion of matter above the poles is facilitated by the formation of a

stand-off shock where the supersonic flow makes a transition to subsonic flow. The compression of the gas behind the shock results in a high temperature which is usually associated with prodigious X-ray emission. The huge difference in the magnetic field strength between white dwarfs and NSs ($B_{WD} \sim 10^7$ G and $B_{NS} \sim 10^{12}$ G) results in noticeable differences in the accretion column for each case. This section will attempt to outline some of the more important aspects of the accretion column model for both the white dwarf and NS case. For a more detailed discussion see for example Frank, King, and Raine (1992, pp. 133–161).

The first consideration needs to be the effect of the magnetic field on the accreting material. In the case of the white dwarf, the gas pressure,

$$P_{gas} = n_e k T \sim 10^8 \left(\frac{n_e}{10^{16} \text{ cm}^{-3}} \right) \left(\frac{T}{10^8 \text{ K}} \right) \text{ dyne cm}^{-2},$$

is much less than the magnetic pressure,

$$P_{mag} = \frac{B^2}{8\pi} \sim 4 \times 10^{12} \left(\frac{B}{10^7 \text{ G}} \right) \text{ dyne cm}^{-2},$$

for typical values of the electron density $n_e \sim 10^{16} \text{ cm}^{-3}$ and temperature $T \sim 10^8$ K. Therefore the magnetic pressure plays a dominant role in the physics of these accretion columns. By considering the Larmor radius for electrons and ions in the magnetic field, it can be seen from Equation 3.6 that the Larmor radii are

$$r_{Le} \sim 2 \times 10^{-5} \left(\frac{B}{10^7 \text{ G}} \right)^{-1} \text{ cm}$$

and

$$r_{Li} \sim 10^{-3} \left(\frac{B}{10^7 \text{ G}} \right)^{-1} \text{ cm}$$

respectively. To test what influence this will have on the inflow of the electrons and ions it is necessary to consider the Debye length, λ_{Deb} , and the mean free path, λ_d . If the particle velocity is determined by thermal motion λ_{Deb} and λ_d are

$$\lambda_{Deb} \cong 7 \left(\frac{T_e}{n} \right)^{1/2} \text{ cm}$$

and

$$\lambda_d \cong 7 \times 10^5 \frac{T^2}{n \ln \Lambda} \text{ cm},$$

where n is the particle density, T_e is the electron temperature and $\Lambda = b_{max}/b_{min}$ is the ratio between the maximum and minimum values of the impact parameter. Typically $\ln \Lambda = 19$ in the

case of white dwarfs and $\ln \Lambda = 20$ in the case of NSs. For typical values this results in

$$\lambda_{Deb} \sim 7 \times 10^{-4} \left(\frac{T_e}{10^8 \text{ K}} \right)^{1/2} \left(\frac{n_e}{10^{16} \text{ cm}^{-3}} \right)^{-1/2} \text{ cm}$$

and

$$\lambda_d \sim 3.6 \times 10^4 \left(\frac{T_e}{10^8 \text{ K}} \right)^2 \left(\frac{n_e}{10^{16} \text{ cm}^{-3}} \right)^{-1} \left(\frac{\ln \Lambda}{19} \right)^{-1} \text{ cm}$$

in the case of an accreting white dwarf. These estimates imply that

$$r_{Le} \ll \lambda_d$$

and

$$r_{Li} \gtrsim \lambda_{Deb}.$$

The first relation implies that electron transport processes, such as thermal conduction, will be strongly suppressed in directions orthogonal to the field, implying that the column is one-dimensional in terms of most relevant electron transport processes. The second relation implies that the Larmor radius of the ions is confined by the Debye radius. This result implies that collisions, rather than the field, will determine the paths of the ions, i.e. they will follow a straight line path between collisions. However, both the electrons and ions will be confined by the field in the accretion column, which is implied by the small Larmor radii,

$$r_L \simeq (10^{-5} - 10^{-3}) \text{ cm}.$$

This is not true of an accretion column in a NS scenario. For a plasma density $n \sim 10^{23} \text{ cm}^{-3}$ and a magnetic field strength $B \sim 5 \times 10^{12} \text{ G}$ the Larmor radius,

$$r_{Li} \sim 1.5 \times 10^{-9} \text{ cm},$$

is less than the Debye length,

$$\lambda_{Deb} \sim 1.7 \times 10^{-7} \text{ cm},$$

resulting in the magnetic field determining the motion of the thermal plasma as a whole. Hence both the ions and electrons follow a ‘‘cork-screw’’ shaped path along the field lines.

An estimate of the particle density in NSs is possible by means of the continuity equation,

$$\begin{aligned} \dot{M} &= A\rho v \\ &= 4\pi R^2 f(-\rho v), \end{aligned} \tag{2.32}$$

where v is the inflow speed of the material and f is the fraction of the surface onto which this material accretes. Assuming that the speed is approximately the free fall speed $-v \sim v_{ff} \sim c_s/2$,

where c_s is the speed of sound, the particle concentration is

$$n \propto \dot{M} f^{-1}.$$

Substituting the continuity equation into the mean free path length

$$\lambda_d = \frac{m^2 v^4}{2\pi n e^4 \ln \Lambda}$$

gives an approximation of

$$\lambda_d \sim 5 \times 10^{11} \left(\frac{\dot{M}}{10^{16} \text{ g s}^{-1}} \right)^{-1} f \text{ cm}$$

where $v \sim c_s/2$ and $\ln \Lambda = 20$. Since the accretion luminosity, $L_{acc} = (GM\dot{M})/(R)$, cannot be much greater than the Eddington limit, $fL_{Edd} = 4\pi Gm_p c/\sigma_T$, an approximation of $\dot{M}f^{-1}$ can be made by setting $L_{acc} \approx L_{Edd}$. This then gives a limit of

$$\left(\frac{\dot{M}}{10^{16} \text{ g s}^{-1}} \right) f^{-1} \lesssim 10^2$$

implying a mean free path of

$$\lambda_d \gtrsim 5 \times 10^9 \text{ cm}.$$

This is much greater than any relevant length scale in the system which implies that any shock that forms in a NS accretion column must be collisionless.

For collisional shocks, the shock width is of the order of the mean free path, where as for collisionless shocks the shock width is usually significantly less than the mean free path. Therefore, for collisional shocks, collisions set up a thermal equilibrium manifesting in a Maxwellian distribution, i.e. a distribution of maximum entropy. Since collisions do not play a role in establishing an equilibrium in collisionless shocks, one usually finds a lack of collisional coupling between ions and electrons, which results in independent electron and ion temperature profiles. For collisional shocks the post-shock region is optically thick resulting in a black body signature in contrast to an optically thin cooling region for collisionless shocks.

Figure 2.13 shows a sketch of the accretion of material onto the surface of a compact object – specifically a white dwarf in this case. The supersonic inflow, which possesses a kinetic energy $\frac{1}{2}v_{ff}^2 = GM/R$ per unit mass, is decelerated to subsonic flows in a stand-off shock above the surface, allowing the material to settle onto the surface of the compact object. Because particles in free fall have the same velocity, the more massive particles will carry the bulk of the kinetic energy. Since $m_i \gg m_e$ this means that the energy is carried mainly by the ions in the inflow.

The position of the shock front becomes very important since this will determine the radiation zone associated with the shock. If the shock occurs below the photosphere, i.e. within a region of

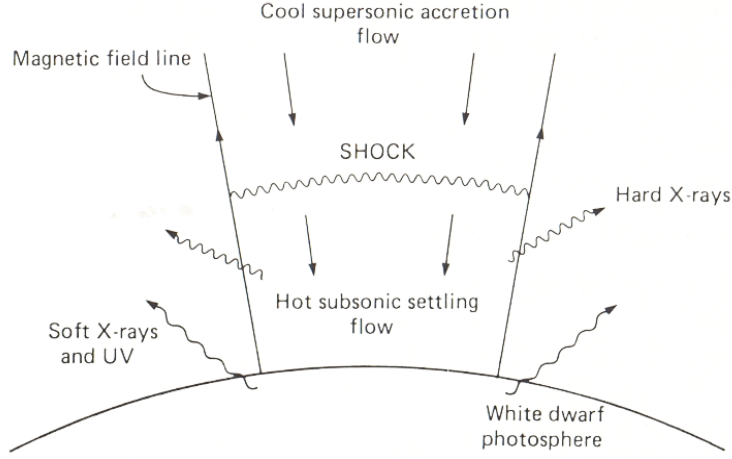


Figure 2.13: Accretion column in a white dwarf (Mason, Watson, and White, 1986). The supersonic inflow is decelerated to subsonic flows in a stand-off shock above the surface, allowing the material to settle onto the surface of the compact object.

high optical depth, the emission will be mainly black body, soft X-ray and UV photons, while if it occurs above the photosphere, the emission will be mainly hard X-rays. The shock will occur where the ram pressure of the inflowing material,

$$P_{ram} = \rho v^2,$$

equals the gas pressure of the post-shock material,

$$P_b = \frac{\rho_b k T_b}{\mu m_H},$$

where the subscript b specifies the boundary or shock point. Here μ is the mean molecular weight, m_H the mass of hydrogen, ρ is the density of the inflow before the shock, v is the inflow speed and ρ_b is the post-shock density. The temperature of the post-shock photospheric region is then

$$\begin{aligned} T_b &= \left(\frac{L_{acc}}{4\pi R^2 f \sigma} \right)^{1/4} \\ &= 1 \times 10^5 \left(\frac{\dot{M}}{10^{16} \text{ g s}^{-1}} \right)^{1/4} \left(\frac{f}{10^{-2}} \right)^{-1/4} \left(\frac{M_1}{M_\odot} \right)^{1/4} \left(\frac{R}{10^9 \text{ cm}} \right)^{-3/4} \text{ K}. \end{aligned} \quad (2.33)$$

An estimate of P_{ram} can be made by estimating ρv from the continuity equations (Equation 2.32) and assuming the inflow velocity is approximately the free-fall velocity $v = v_{ff} \sim \sqrt{2GM/R}$. This gives

$$\begin{aligned}
|P_{ram}| &= (\rho v)v_{ff} \\
&= \left(\frac{\dot{M}}{4\pi R^2 f} \right) v_{ff} \\
&= 4 \times 10^7 \left(\frac{\dot{M}}{10^{16} \text{ g s}^{-1}} \right) \left(\frac{f}{10^{-2}} \right)^{-1} \left(\frac{M_1}{M_\odot} \right)^{1/2} \left(\frac{R}{10^9 \text{ cm}} \right)^{-1/2} \text{ dyne cm}^{-2}.
\end{aligned} \tag{2.34}$$

Assuming that $P_{ram} = P_b$ behind the shock allows for an estimate of the post-shock density, i.e.

$$\begin{aligned}
\rho_b &= \frac{\mu m_H}{kT_b} P_{ram} \\
&= 3 \times 10^{-6} \left(\frac{\dot{M}}{10^{16} \text{ g s}^{-1}} \right)^{3/4} \left(\frac{f}{10^{-2}} \right)^{-3/4} \left(\frac{M_1}{M_\odot} \right)^{1/4} \left(\frac{R}{10^9 \text{ cm}} \right)^{-7/4} \text{ g cm}^{-3}.
\end{aligned} \tag{2.35}$$

Equations 2.33 and 2.35 provide estimates of the post-shock temperature and density. To determine whether this is above or below the photosphere, T_b and ρ_b will be used to estimate the opacity of the material. The Rosseland mean opacity for this temperature and density range is given by (see e.g. Frank, King, and Raine (1992, p. 135))

$$\kappa_R \cong 5 \times 10^{24} \rho_b T_b^{-7/2} \text{ cm}^2 \text{ g}^{-1},$$

which implies a photon mean free path length

$$\begin{aligned}
\lambda_{ph} &= \frac{1}{\kappa_R \rho_b} \\
&= 7 \times 10^3 \left(\frac{\dot{M}}{10^{16} \text{ g s}^{-1}} \right)^{1/8} \left(\frac{f}{10^{-2}} \right)^{-1/8} \left(\frac{M_1}{M_\odot} \right)^{3/8} \left(\frac{R}{10^9 \text{ cm}} \right)^{-7/8} \text{ cm}.
\end{aligned}$$

A proton that enters into a plasma with a velocity much higher than the plasma thermal velocity will move a distance

$$\lambda_S = \frac{m_e E_p^2}{2\pi n e^4 \ln \Lambda m_p}, \tag{2.36}$$

where E_p is the kinetic energy of the proton and $nm_p \simeq \rho_{pls}$ is the plasma mass density, before the speed reduces to the average thermal velocity of the plasma (e.g. Frank, King, and Raine (1992, p. 32)). For the shock described above, this distance is

$$\lambda_S \approx 3 \left(\frac{\dot{M}}{10^{16} \text{ g s}^{-1}} \right)^{-3/4} \left(\frac{f}{10^{-2}} \right)^{3/4} \left(\frac{M_1}{M_\odot} \right)^{7/4} \left(\frac{R}{10^9 \text{ cm}} \right)^{-1/4} \text{ cm}$$

for $\ln \Lambda = 19$. The difference in lengths, $\lambda_S \ll \lambda_{ph}$, implies that the protons and ions are stopped before reaching the photosphere, implying the shock forms well above the stellar surface

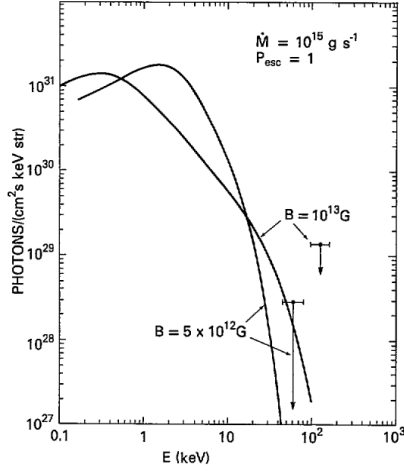


Figure 2.14: The emitted spectrum of an accretion column in the case where no shock forms. The energy is released through multiple Coulomb collisions (Meszaros et al., 1983).

or photosphere. The resulting shock temperature is then

$$T_S = 3.7 \times 10^8 \left(\frac{M_1}{M_\odot} \right) \left(\frac{R}{10^9 \text{ cm}} \right)^{-1} \text{ K.} \quad (2.37)$$

The flow after the shock will be subsonic with a characteristic speed

$$\begin{aligned} -v_2 &= \frac{v_{ff}}{4} \\ &= 1.3 \times 10^8 \left(\frac{M_1}{M_\odot} \right)^{1/2} \left(\frac{R}{10^9 \text{ cm}} \right)^{-1/2} \text{ cm s}^{-1} \\ &= 1300 \left(\frac{M_1}{M_\odot} \right)^{1/2} \left(\frac{R}{10^9 \text{ cm}} \right)^{-1/2} \text{ km s}^{-1}, \end{aligned} \quad (2.38)$$

where the subscript 2 indicates the post-shock region.

The situation is more complicated in the NS case where there is uncertainty about the collisionless shock and where the observed high X-ray luminosity can approach the Eddington limit. This high luminosity requires that radiation pressure must be considered when modelling the accretion column. Systems where the luminosity does not exceed the Eddington limit are called *subcritical* and the radiation pressure can be ignored. If material in the column accretes onto a subcritical NS where a shock does not form, the energy is released through multiple Coulomb collisions (for a discussion of this see e.g. Frank, King, and Raine (1992, pp. 152–154) and Meszaros et al. (1983)). Figure 2.14 shows an example of a calculated spectrum in such a case. In the case where a collisionless shock forms, the accretion column is similar to the white dwarf case discussed above. The important difference is that the post-shock temperature of the ion

and electron populations is different, i.e.

$$\begin{aligned} T_i &= \frac{3\mu m_H}{16k} v_{ff}^2 \\ &\approx 3.7 \times 10^{11} \left(\frac{M_1}{M_\odot} \right) \left(\frac{R}{10^6 \text{ cm}} \right)^{-1} \text{ K} \end{aligned}$$

and

$$\begin{aligned} T_e &= \frac{5m_e}{16k} v_{ff}^2 \\ &\approx 5.5 \times 10^8 \left(\frac{M_1}{M_\odot} \right) \left(\frac{R}{10^6 \text{ cm}} \right)^{-1} \text{ K} \end{aligned} \quad (2.39)$$

for ions and electrons respectively. In systems where the radiation pressure is important, the inflow material is slowed by Thomson scattering of the electrons, which results in a slowing of the ion population because of the coupling due to Coulomb forces between them. If it is assumed that the shock front is close enough to the surface so that curvature considerations can be ignored, the magnetic field can be considered as constant and the radiation energy density, U_{rad} , as isotropic. This allows simple approximations to be made for these systems.

This section will end by considering a possible steady state solution to the accretion column problem, and some of the properties that can be determined from it. In order to have a steady state solution, the rate at which energy is released from the post-shock region must equal the rate at which it reaches the shock. The energy is removed from the post-shock region via cooling mechanisms, for example through radiation and particle transport. In the white dwarf case the cooling process takes place mainly through free-free (bremsstrahlung) emission in the post shock material. The characteristic time scale of this cooling is (e.g. Frank, King, and Raine (1992, p. 138))

$$\begin{aligned} t_{rad} &\sim 2 \times 10^{11} \frac{T_e^{1/2}}{n_e} \text{ sec} \\ &\sim 7 \left(\frac{\dot{M}}{10^{16} \text{ g s}^{-1}} \right)^{-1} \left(\frac{f}{10^{-2}} \right) \left(\frac{M_1}{M_\odot} \right) \left(\frac{R}{10^9 \text{ cm}} \right) \text{ sec}, \end{aligned}$$

for $T_e = T_S$ (Equation 2.37) and $n_e = n_2$, the post-shock electron density, which is typically

$$n_2 = 5.9 \times 10^{14} \left(\frac{\dot{M}}{10^{16} \text{ g s}^{-1}} \right) \left(\frac{f}{10^{-2}} \right)^{-1} \left(\frac{M_1}{M_\odot} \right)^{-1/2} \left(\frac{R}{10^9 \text{ cm}} \right)^{-3/2} \text{ cm}^{-3}.$$

These values are estimated from the continuity equation (Equation 2.32) and the post-shock velocity (Equation 2.38). This allows for an estimate of the shock height if free-free radiation is

the only cooling mechanism;

$$D_{rad} \sim -v_2 t_{rad} \\ \simeq 9 \times 10^8 \left(\frac{\dot{M}}{10^{16} \text{ g s}^{-1}} \right)^{-1} \left(\frac{f}{10^{-2}} \right) \left(\frac{M_1}{M_\odot} \right)^{3/2} \left(\frac{R}{10^9 \text{ cm}} \right)^{1/2} \text{ cm.}$$

Other cooling mechanisms (e.g. Compton scattering and cyclotron radiation) are much less effective in white dwarf accretion columns than free-free radiation. Since the system is considered to be one dimensional, where the vector \mathbf{z} is perpendicular to the surface, the equations governing the continuity, momentum and energy are

$$\rho v = \text{constant},$$

$$\rho v \frac{dv}{dz} + \frac{d}{dz} \left(\frac{\rho k T}{\mu m_H} \right) + g \rho = 0,$$

and

$$\frac{d}{dz} \left[\rho v \left(\frac{3kT}{2\mu m_H} + \frac{v^2}{2} + g \rho \right) + \frac{\rho v k T}{\mu m_H} \right] = a \rho^2 T^{1/2}$$

where

$$a = 2 \times 10^{-27} m_H^{-2}.$$

Solutions to these equations show that the shock height is

$$D = k T_S^{1/2} \frac{-v_2}{\mu m_H a \rho_2}.$$

The hard X-ray emission in these systems originates from the heated shock front ($kT_S \sim 60$ keV) and post-shock material. The energy is provided by the cooling of the post-shock material so that at any point in the column, with temperature T , the energy that has been released is proportional to $T_S - T$. Secondary soft emission originates from absorbed and re-emitted emission from the surface of the white dwarf. Figure 2.15 shows the X-ray emission from AM Herculis, showing both hard and soft x-ray emission.

In the post shock of the accretion columns in NSs, cooling occurs through free-free and cyclotron radiation. Cyclotron radiation in the case of the NS accretion column will have a fundamental frequency of

$$\nu_{cyc} = \frac{eB}{2\pi m_e c} \\ = 2.8 \times 10^{18} \left(\frac{B}{10^{12} \text{ G}} \right) \text{ Hz.}$$

Due to the high magnetic field, cyclotron radiation is a more effective cooling mechanism than free-free radiation in NSs, and therefore the cooling and observed emission is mainly the result

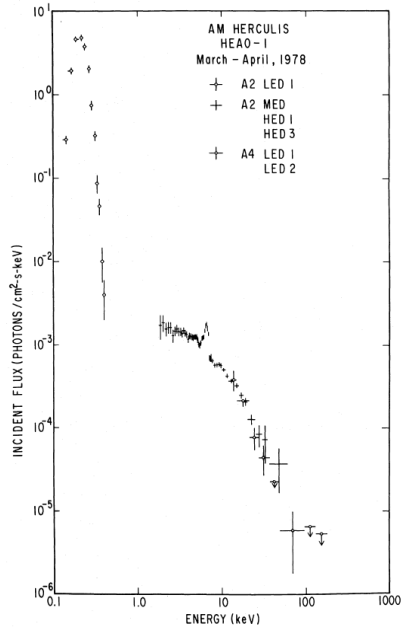


Figure 2.15: X-ray spectrum of AM Herculis (Rothschild et al., 1981).

of cyclotron radiation. Figure 2.16 shows a theoretical curve for the observed emission for such an accretion column.

2.3 Neutron Stars/Pulsars

When considering XRB systems it is necessary to consider the nature of the compact object, i.e. whether it is a white dwarf, NS or BH. In the case of HMXBs the compact object is normally a NS or BH. Before considering HMXBs it is necessary to consider some of the properties of the compact objects in general. For a more detailed review of NSs see for example Kawaler et al. (1996, pp. 97-232).

Once a star has run out of nuclear fuel for the fusion reactions within its core, gas pressure alone is unable to sustain its enormous weight ($\sim M_{\odot} = 1.99 \times 10^{33}$ g). The star must then collapse. If the core is light enough, this collapse will eventually be halted by electron degeneracy pressure, becoming what is known as a white dwarf. White dwarfs, while no longer releasing energy through nuclear fusion, are still hot and emit energy through black body radiation. There is a limit to how massive white dwarfs can become as was initially shown by Chandrasekhar (1931). What is now known as the Chandrasekhar limit (e.g. Phillips (1994)),

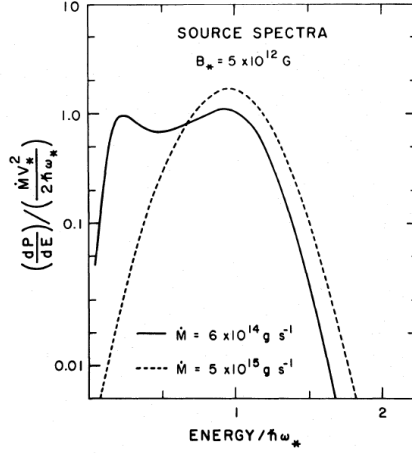
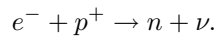


Figure 2.16: Emission spectra for an accretion column with a collisionless shock (Langer and Rappaport, 1982b).

$$\begin{aligned}
 M_{CH} &\approx \left(\frac{27}{2\pi^2} \right)^{1/2} \left(\frac{Y_e}{m_H} \right)^2 \left(\frac{hc}{4G} \right)^{3/2} \\
 &\approx 4.3 Y_e^2 M_\odot \\
 &\approx 1.4 M_\odot,
 \end{aligned}$$

shows that the mass of a white dwarf cannot exceed $1.4 M_\odot$ as the electron degeneracy pressure can no longer support the mass. Here Y_e is the number of electrons per nucleon and m_H is the mass of a hydrogen atom. In stars that exceed the Chandrasekhar limit, the core collapses and the density becomes so high that electrons and protons recombine to form a neutron and a neutrino in a process called β decay;



The collapsed core is then supported by neutron degeneracy. The possibility of NSs was initially proposed by Lev Landau in the 1930s but was only detected in 1967 as a pulsating radio source (Hewish et al., 1968). Since that first detection the number of known pulsars has grown to more than 1500 (Manchester et al., 2005) (Figure 2.17).

2.3.1 Properties of Neutron Stars

The properties of a NS are in many ways dependent on its internal structure, as well as the equation of state which is mainly determined by the nature of the exotic matter in the interior (see Figure 2.18). As a result, many of the questions surrounding NSs remain unanswered. While

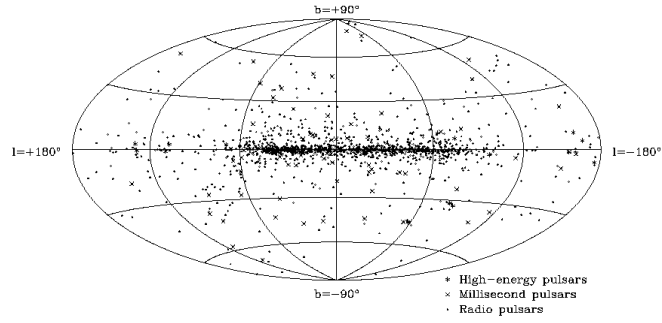


Figure 2.17: Map of known pulsars in galactic co-ordinates (Manchester et al., 2005).

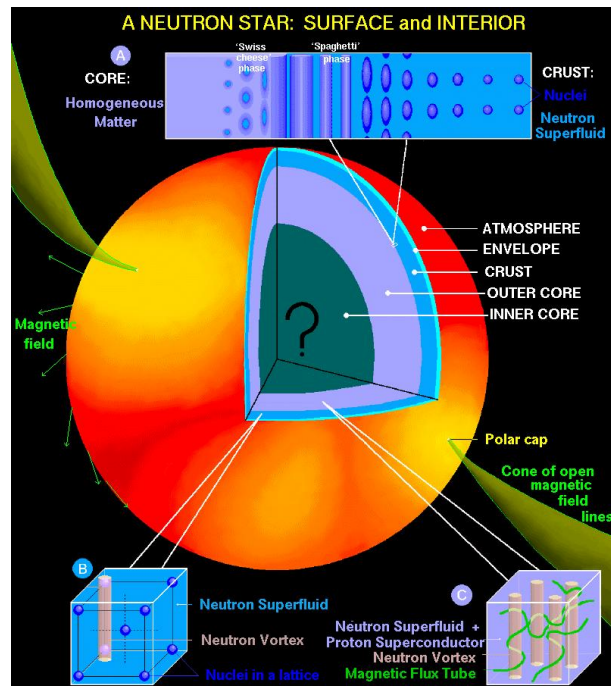


Figure 2.18: Interior structure of a NS (http://www.astroscu.unam.mx/neutrones/NS-Picture/NStar/NStar_1.gif).

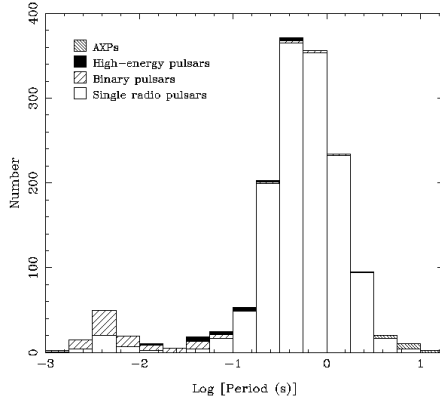


Figure 2.19: Pulse period of all known pulsars (Manchester et al., 2005).

much work still needs to be done, certain parameters are considered to be known to some degree of certainty. Figure 2.18 shows the structure of a neutron star. The following is a list of typical values for the parameters of NSs:

Mass: The Mass of the neutron star is $\sim M_{\odot}$. NSs are assumed to have a mass greater than the Chandrasekhar limit of $1.4 M_{\odot}$ and an upper mass limit defined by the Oppenheimer-Volkoff equations (Oppenheimer and Volkoff, 1939). The Oppenheimer-Volkoff equations are dependent on the unknown nature of NS material and so it is not possible to find an exact numerical value for this limit. Compact objects with masses above $3.2 M_{\odot}$ are generally considered to be black holes (Rhoades and Ruffini, 1974).

Radius: The radius of a NS is $\sim 10 - 12$ km.

Density: The density is considered to be roughly that of the atomic nucleus $\sim 10^{14} \text{ g cm}^{-3}$

Magnetic Field: The magnetic field strength of NSs/pulsars vary with age. They range from $B \sim 10^9$ G for radio pulsars, up to greater than 10^{15} G for magnetars. A value of $B \sim 10^{12}$ G is usually considered as a typical value.

Spin period: The pulsars spin period is the most accurately measured property, varying from milliseconds to hundreds of seconds (Figure 2.19).

Temperature: The temperature is approximately 10^6 K.

Models for the internal structure of NSs is beyond the scope of this study. Instead the observable properties will be considered.

2.3.2 The Pulsar Wind

Shortly after the discovery of the first pulsar, a paper by Goldreich and Julian (1969) proposed the existence of a pulsar wind. These authors considered the scenario of a rotating NS within

its SNR remnant. They showed that the electric field for a NS with a spin frequency Ω , an inclination of the magnetosphere to the spin axis θ , and poloidal magnetic field \mathbf{B}_p would be

$$\mathbf{E} = \frac{-\Omega r \sin \theta}{c} \hat{\phi} \times \mathbf{B}_p,$$

at a distance r , where $\hat{\phi}$ is a unit vector in the azimuthal direction. For a NS with a mass M , spin period P , magnetic field strength B , and radius R , the effect of the electromagnetic field would be

$$\alpha = \frac{F_{e,e}}{F_g} \approx 8 \times 10^{11} \left(\frac{B}{10^{12} \text{G}} \right) \left(\frac{R}{10^6 \text{cm}} \right)^3 \frac{\cos^2 \theta}{PM} \quad (2.40)$$

and

$$\alpha = \frac{F_{e,p}}{F_g} \approx 5 \times 10^8 \left(\frac{B}{10^{12} \text{G}} \right) \left(\frac{R}{10^6 \text{cm}} \right)^3 \frac{\cos^2 \theta}{PM} \quad (2.41)$$

times greater than the gravitational force exerted on an electron and a proton respectively. This effectively shows that it is impossible for a rotating NS to be surrounded by a vacuum and that the electromagnetic forces must drive a wind of charged particles. (Later work has shown that it is unlikely for ions to leave the surface because of binding energy in the crust – see for example Ruderman and Sutherland (1975) and references therein). Pulsar winds are now considered to consist of accelerated electrons and positrons. The magnetosphere, as modelled by Goldreich and Julian, is divided into three sections, the *near zone*, the *wind zone* and the *boundary zone*.

Near and Wind Zone

The near zone is the section of the magnetosphere where particles are trapped by the magnetospheric field inside the light cylinder. The light cylinder is defined as the radius at which the rotational velocity of the field lines reaches the speed of light, i.e.

$$r \sin \theta = \frac{c}{\Omega}. \quad (2.42)$$

Beyond the light cylinder, the magnetic field lines can be considered open, constituting the wind zone. Particles flow away from the NS along these open field lines, creating the pulsar wind. Figure 2.20 shows the near and wind zone.

The Goldreich-Julian model assumes that the electric potential is highest at the equator and decreases towards the poles. As a result there will be a point on the surface of the NS where the electric potential is equal to the electric potential of the interstellar medium (ISM). The field line that joins this point to the ISM is known as the *critical line* and marks a boundary in the wind zone. Positive particles are trapped and stream out of the system below the critical line while negative particles leave the system above it (Figure 2.20).

In the near zone, where the plasma is trapped in the closed field lines (inside the light cylinder), the force-free condition requires $\mathbf{E} \cdot \mathbf{B} = 0$, i.e. no magnetic field aligned E-fields exist that can accelerate charged particles. However in the wind zone this condition is violated. There

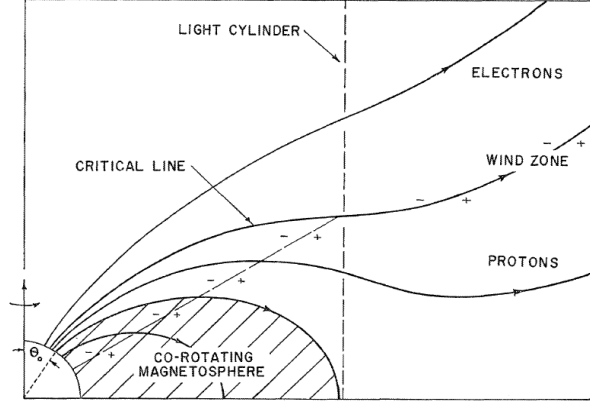


Figure 2.20: The near and wind zone of a rotating neutron star (Goldreich and Julian, 1969). Beyond the light cylinder particles flow away from the NS along open field lines creating the pulsar wind.

exists a flux of relativistic particles that accelerate along the field lines originating from the poles. In the wind zone (outside the light cylinder) charged particles may also be accelerated in the fields associated with the outward propagating magnetic dipole wave. In this region, $|E| \rightarrow |B|$, and the maximum energy charged particles can reach immediately outside the light cylinder, $R_L = c/\Omega_*$, is (ignoring radiative energy losses for illustrative purposes)

$$\begin{aligned} \epsilon_{max} &\leq eER_L \\ &\lesssim 5 \times 10^9 eB_L P_* . \end{aligned}$$

Here B_L represents the magnetosphere field in the wave zone, just outside the light cylinder. Assuming $B_* \sim 10^{12}$ G, it can be shown that for $P_* = 1$ sec, the magnetospheric field at

$$R_L \approx 5 \times 10^9 \left(\frac{P_*}{1 \text{ sec}} \right) \text{ cm},$$

is $B_L \approx 10$ G. Then

$$\epsilon_{max} \leq 10^{14} \left(\frac{B_L}{10 \text{ G}} \right) \left(\frac{P_*}{1 \text{ sec}} \right) \text{ eV}.$$

This estimate, although elementary, illustrates that a travelling magnetic dipole wave from a fast rotating NS can be a very effective particle accelerator.

Boundary Zone

After the SN explosion that created the pulsar, all ISM material is evacuated up to a distance D , known as the SN cavity. It has been proposed that the boundary zone makes up $\sim 90\%$ of the SN cavity, beginning at $r \sim D/10$ and extending up to D (Figure 2.21). Most of the acceleration of the pulsar wind occurs in this region. Crossing of electric and magnetic fields in the wind and

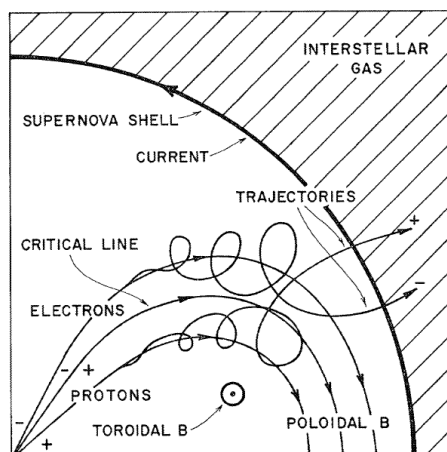


Figure 2.21: The *Boundary zone* (Goldreich and Julian, 1969). The boundary zone makes up $\sim 90\%$ of the SN cavity, beginning at $r \sim D/10$ and extending up to D , the radius of the SN cavity.

boundary layer, i.e.

$$\mathbf{F} = \frac{1}{c} \mathbf{E} \times \mathbf{B},$$

pushes all particles out of the SN cavity, preventing material from the ISM streaming along field lines and accreting onto the NS.

2.3.3 Pulsar Spin-Down Power

Observations of pulsars reveal that the spin period changes with time. The pulsar is either “spinning-down” resulting in a longer pulse period, or it is “spinning-up” resulting in a shorter pulse period. Spin-up is considered evidence of an accretion disc surrounding the pulsar (see e.g. Rappaport et al. (1978)). This occurs when the magnetic field lines connecting the pulsar to the accretion disc attach at a distance where the Keplerian orbit is shorter than the spin period. If the magnetic field lines connect at a distance where the Keplerian orbit is longer than the spin period, the pulsar will be spun down. The spinning down of isolated pulsars is evidence of rotational energy loss, which powers the pulsar wind and nebula.

Since isolated pulsars within a SNR are spinning down, there is a connection between its spin period and its age. The spin down luminosity of a pulsar is given by

$$\begin{aligned} \dot{E} &= -\frac{dE_{rot}}{dt} \\ &= -\frac{d}{dt} \left(\frac{1}{2} I \Omega_*^2 \right) \\ &= 4\pi^2 I \frac{\dot{P}}{P^3} \end{aligned} \tag{2.43}$$

where $I \approx 10^{45} \text{g cm}^2$ is the moment of inertia and $\dot{P} = dP/dt$ is the change in spin period.

If it is assumed that the pulsar is spinning down with a constant braking index, n , such that $\dot{\Omega} = -k\Omega^n$, the age of the pulsar, τ , can be determined for $n \neq 1$ by

$$\begin{aligned} \int_{\Omega_0}^{\Omega} \Omega^{-n} d\Omega &= -k \int_0^{\tau} dt \\ \therefore \tau &= \frac{1}{1-n} \frac{\Omega^n}{\dot{\Omega}} [\Omega^{-n+1} - \Omega_0^{-n+1}]. \end{aligned}$$

Rewriting this in terms of the period, P , gives

$$\tau = \frac{P}{(n-1)\dot{P}} \left[1 - \left(\frac{P_0}{P} \right)^{n-1} \right], \quad (2.44)$$

where P_0 is the initial spin period of the pulsar (see e.g. Gaensler and Slane (2006) and references therein). Unfortunately the value of n has only been accurately determined for four pulsars (see Livingstone et al. (2005) and references therein) showing that the spin down of pulsars is more complicated than a constant braking index. Under the assumption that $P \gg P_0$, Equation 2.44 simplifies to

$$\tau = \frac{P}{(n-1)\dot{P}}.$$

The characteristic age of a pulsar is then defined as

$$\tau_c \equiv \frac{P}{2\dot{P}}, \quad (2.45)$$

where $n \simeq 3$ is assumed. Since the characteristic age is dependent on the two above mentioned assumptions (constant braking index n and $P \gg P_0$), the accuracy of Equation 2.45 is questionable.

If it is assumed that the pulsars have a dipole magnetic field, the strength of that field at the equator is dependent on the period of rotation, such that (e.g. Bhattacharya and van den Heuvel (1991) and references therein)

$$\begin{aligned} B_p &= \left(\frac{3c^3 I}{8\pi^2 R^6} P \dot{P} \right)^{1/2} \\ &\simeq 3.2 \times 10^{19} (\dot{P} P)^{1/2} \text{ G}, \end{aligned} \quad (2.46)$$

for $R = 10^6$ cm. Thus both the energy released and the magnetic field strength of a pulsar can be considered in terms of its spin period and the variation thereof.

2.4 Black Holes

For a more detailed review of the BH structure and equations see e.g. Kawaler et al. (1996, 237-327) and Schutz (1985), and for accretion onto a BH see e.g. Frank, King, and Raine (1992, pp. 166–169).

While there is no definite numerical value to the Oppenheimer-Volkoff equations (Oppenheimer and Volkoff, 1939), a mass limit of $\sim 3 M_{\odot}$ for NSs is normally assumed (Rhoades and Ruffini, 1974). A compact object with a mass above this is considered to be a BH. The mass of a BH progenitor is not well understood, with arguments ranging from $10 M_{\odot}$ up to $\geq 40 M_{\odot}$ (see e.g. van den Heuvel and Habets (1984)).

There are three different kinds of BHs, namely,

1. Stellar mass BHs that result from the collapse of a star,
2. Supermassive BHs that exist in the centre of galaxies, and
3. Primordial BHs that could have come into existence shortly after the big bang.

Since it is believed that some HMXBs and microquasars are powered by accretion processes onto stellar mass black holes, the properties of these bizarre objects will be briefly reviewed. The discussion will be restricted to stellar mass non-rotating and rotating BHs.

2.4.1 Non-Rotating Black Holes

The boundary defining the edge of a non-rotating or Schwarzschild BH is the Schwarzschild radius, i.e.

$$R_{Schw} = \frac{2GM}{c^2}. \quad (2.47)$$

Material that crosses the Schwarzschild radius is “lost to the universe”. This is a very small region of space. If we consider a BH with a mass M this translates to a Schwarzschild radius of

$$\begin{aligned} R_{Schw} &= \frac{2GM}{c^2} \\ &\approx 3 \left(\frac{M}{M_{\odot}} \right) \text{ km.} \end{aligned}$$

The effects of GR only become important at a radius of a few R_{Schw} , and for any radius $R \gg R_{Schw}$ the binary system can be considered as classical.

There is no stable circular orbit within a radius of $3 R_{Schw}$ and any material reaching that point quickly falls past the Schwarzschild radius. This occurs very quickly as material in free fall will flow from $3 R_{Schw}$ to R_{Schw} in a time

$$t_{ff} \sim \left(\frac{R_{Schw}^3}{GM} \right)^{1/2} \sim 10^{-4} \text{ seconds,}$$

for a $3 M_{\odot}$ BH. As a result very little energy is lost while the material is in the final non-Keplerian region.

2.4.2 Kerr Black Holes

As discussed above, the effect of general relativity is usually not significant when considering accretion onto non-rotating BHs. While this argument still holds true for rotating or Kerr BHs, the effect of frame dragging has been proposed as a possible mechanism for launching jets in microquasar systems. For this reason, the Kerr BH will briefly be discussed. It is neither the aim to explain nor to examine the details of the equations governing the Kerr BH, and so only the most important results will be mentioned.

The geometry of a Kerr BH is determined by the mass, M , and the angular momentum, J . The resulting line element, in units $G = c = 1$, is then given by (Boyer and Lindquist, 1967)

$$\begin{aligned} ds^2 &= \frac{\Delta - a^2 \sin^2 \theta}{\rho^2} dt^2 + 2a \frac{2Mr \sin^2 \theta}{\rho^2} dt d\phi \\ &- \frac{(r^2 + a^2)^2 - a^2 \Delta \sin^2 \theta}{\rho^2} \sin^2 \theta d\phi^2 \\ &- \frac{\rho}{\Delta} dr^2 - \rho^2 d\theta^2, \end{aligned}$$

where

$$\begin{aligned} \Delta &= r^2 - 2Mr + a^2, \\ \rho^2 &= r^2 + a^2 \cos^2 \theta \end{aligned}$$

and

$$a = \frac{J}{M}.$$

Here ϕ is the azimuthal angle around the rotation axis and r and θ can be considered as standard spherical coordinates.

The fact that

$$g_{t\phi} = \frac{2am_r \sin^2 \theta}{\rho^2} \neq 0,$$

in the space-time metric of a rotating object has far reaching consequences. It can be shown that a natural consequence of this is *frame dragging*, resulting in space-time swirling in the vicinity of a rotating mass with an angular velocity

$$\omega(r, \phi) = \frac{d\phi}{dt} = \frac{g^{\phi t}}{g^{tt}}.$$

Therefore, any particle entering this space-time tornado will rapidly gain a velocity

$$v_{\phi}(r, \phi) = r\omega(r, \phi).$$

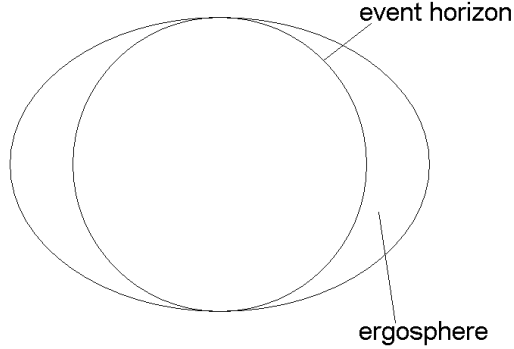


Figure 2.22: The ergosphere surrounding a Kerr black hole.

The outer boundary to the frame dragging is found to lie at a distance

$$r_{ergo}^+ = M + \sqrt{M^2 - a^2 \cos^2 \theta}$$

where the super-script + indicates that this is the positive solution to the equation. The distance to the event horizon is,

$$r_h^+ = M + \sqrt{M^2 - a^2},$$

which means, that with the exception of at the poles where $\cos \theta = 1$, $r_{ergo} > r_h$ (Figure 2.22). Within this region of space nothing can be stationary, and it is therefore known as the ergo-zone or ergo-sphere^{||}. Since this region lies outside of the event horizon it is possible for particles to enter this region, gain angular momentum, and leave the region again. This provides a mechanism for extracting rotational kinetic energy from a BH.

2.5 Evolution of High Mass X-ray Binaries

The evolution of XRBs is directly determined by the evolutionary path followed by a single star. This determines the matter transfer in the system which determines the evolution of the binary system. Accretion plays a prominent role in HMXB evolution and occurs through either Roche lobe overflow or wind accretion (see Sections 2.2.1 & 2.2.2). Since the evolution of the binary system is dependent on the life cycle of stars, it is necessary to first consider some aspects of this. A more detailed review on the evolution of stars is given by e.g. Phillips (1994) and the evolution of HMXBs by e.g. Lewin et al. (1995, pp. 464-476).

^{||}Ergo means energy or work.

Table 2.2: Fusion process in stars (Phillips, 1994, p. 26).

Fuel	Required Temp (K)	Required Mass (M_{\odot})
Hydrogen	1×10^7	
Helium	1×10^8	
Carbon	5×10^8	> 8
Neon	1×10^9	
Oxygen	2×10^9	
Silicon	3×10^9	> 11

2.5.1 Stellar Evolution

A star is considered as a self-gravitating gas held in hydrostatic equilibrium by gas and radiation pressure, i.e.

$$\frac{d}{dr} \left[\left(\frac{\rho k T}{\mu m_p} \right)_{gas} + \left(\frac{1}{3} a T^4 \right)_{rad} \right] = - \frac{GM(r)\rho(r)}{r^2},$$

where ρ is the density, k is Boltzmann's constant, T the temperature, μ the mean molecular weight and

$$a = \frac{8\pi^5 k^4}{15h^3 c^3} = 7.565 \times 10^{-16} \text{ J K}^{-4} \text{ m}^{-3}$$

with h representing Planck's Constant. Nuclear fusion within the core of the star supplies the radiative energy and heat to keep the star stable.

Initially this energy is supplied through hydrogen fusion. Once the hydrogen fuel is depleted and hydrogen fusion ceases, the core of the star will begin to contract. This contraction results in an increase in temperature and pressure which causes the outer envelope of the star to expand. If the core possesses sufficient mass, the temperature in the core will eventually become hot enough for helium fusion to begin. The energy released in the helium burning process expands the non-degenerate core, causing a lowering of temperature and pressure which results in a slight contraction of the outer envelope. After helium burning, the star will progress through cycles of nuclear fusion, continuing with carbon, neon, oxygen and finally silicon burning. For each of these stages to occur, the core of the star requires sufficient mass to generate enough heating during the core contraction (Table 2.2). During each of these fusion cycles, the envelope of the star goes through a period of expansion and contraction, occurring on the thermal timescale (Lewin et al., 1995)

$$\tau_t \simeq \frac{GM^2}{RL} \simeq 3 \times 10^7 \left(\frac{M}{M_{\odot}} \right)^2 \frac{R_{\odot}}{R} \frac{L_{\odot}}{L} \text{ yrs.}$$

This expansion and contraction determines at what point during the evolution of the binary system the star will fill its Roche lobe.

If a star is massive enough to evolve to the point that silicon burning occurs, it is left with an iron core. Since iron fusion is an endothermic process, this marks the end point for nuclear

Table 2.3: The initial masses of different HMXB progenitors (Lewin et al., 1995, p. 465).

Initial mass	He core mass	Final Product	
		Single star	Binary member
$< 3M_{\odot}$	$< 0.45M_{\odot}$	CO white dwarf	He white dwarf
$3 - 8M_{\odot}$	$0.5 - 1.9M_{\odot}$	CO white dwarf	CO white dwarf
$8 - 11M_{\odot}$	$1.9 - 2.9M_{\odot}$	neutron star	O-Ne-Mg white dwarf or neutron star
$11 - 40M_{\odot}$	$2.9 - 17.5M_{\odot}$	neutron star	neutron star
$> 40M_{\odot}$	$> 17.5M_{\odot}$	black hole	black hole

burning and the star is no longer able to produce energy to support its weight. The result is that the core collapses into a neutron star or black hole, producing a shock wave that blows away the outer envelopes. Table 2.3 lists the required initial masses for certain binary systems. The uncertainty of these values should be noted given the the many unanswered questions of stellar evolution.

A qualitative discussion of the most relevant aspects of HMXB evolution will now be presented.

2.5.2 The Conservative HMXB Binary Evolution

This section will briefly discuss how a binary system can evolve from a system consisting of two main-sequence stars to an HMXB that contains a NS or BH. The problem is greatly simplified if it is assumed that the system is conservative, i.e. there is conservation of angular momentum and mass in the system. This means that *all* the mass that is lost from one star must accrete onto its companion. In reality this will not occur since stars will lose matter and angular momentum through their stellar wind, but if it is assumed that the progenitor systems of HMXBs exchange mass mainly through Roche lobe overflow, then the material lost to the stellar wind can be considered insignificant. Figure 2.23 shows an example of conservative binary evolution. The system begins with two main sequence stars, the more massive of which is known as the primary, and the less massive as the secondary. The more massive of these two stars (the primary) will evolve along the main sequence faster and at some point will fill its Roche lobe. The time at which this occurs depends on the masses of the stars and the binary separation between them. In order to illustrate the problem, an example with mass values of $M_p = 20 M_{\odot}$ and $M_s = 6 M_{\odot}$ is presented (Bowers and Deeming, 1984, pp. 325-327). After $\sim 6.16 \times 10^6$ years, the primary star will have depleted its hydrogen core, and expands until it fills its Roche lobe**. Once the star fills its Roche lobe, mass transfer onto its companion star will be initiated. Since material is being transferred from the more massive to the less massive star, this results in the shortening

**This is specific to the example presented here. For systems with different mass ratios, the primary star may have to under go additional burning phases before it expands enough to fill its Roche lobe.

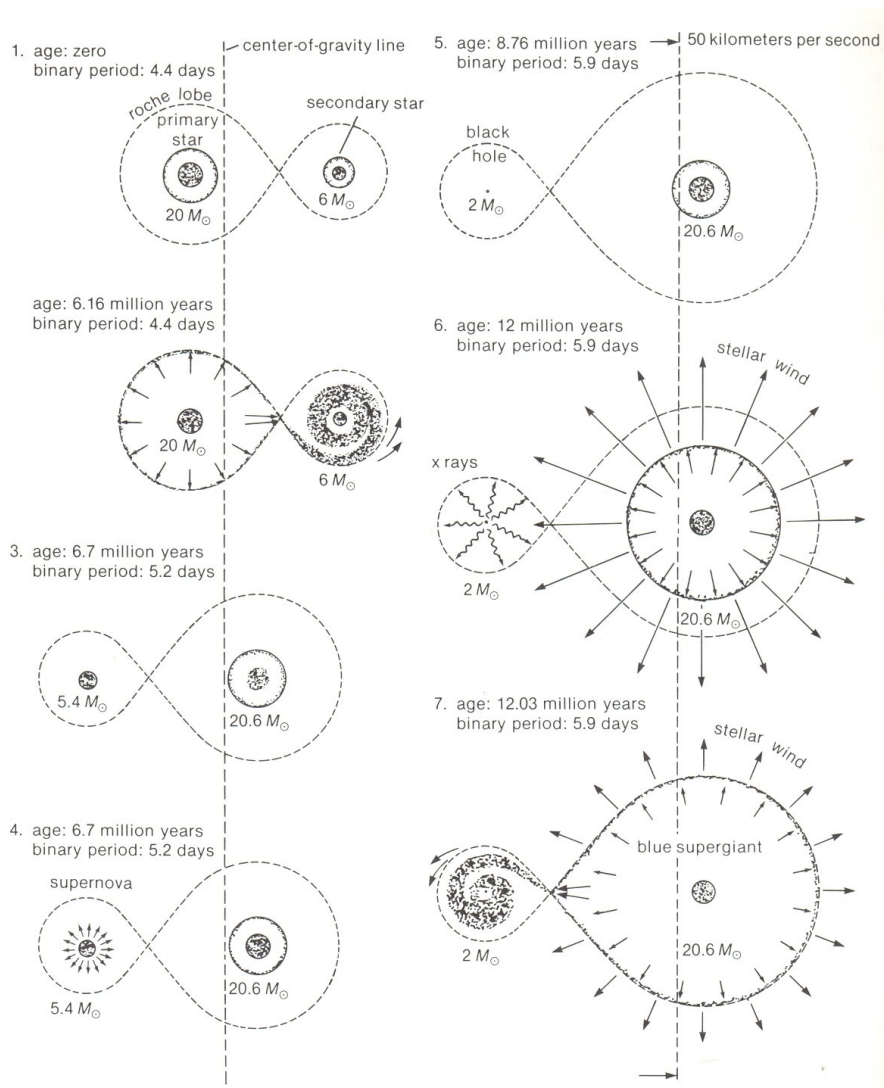


Figure 2.23: The conservative evolution of a binary system (Bowers and Deeming, 1984). See the text for an explanation.

of the orbital period (see Equation 2.14)^{††}. A physical explanation of this is that more mass is placed further away from the centre of mass. Conservation of angular momentum of the binary requires the orbit to shrink.

At some point during the mass transfer process, enough material will have been transferred to the secondary star that the mass ratio reverses, i.e. the mass donor becomes the lighter of the two stars. The orbital period will then begin to increase. Mass transfer is a rapid process, lasting only $\sim 2 \times 10^4$ years, in the example considered.

The primary (the initial mass donor) is now the less massive of the two stars ($M_p = 5.4 M_\odot$) and the companion has been transformed into a hydrogen rich supergiant on the main sequence ($M_s = 20.6 M_\odot$). The less massive primary then continues to progress through stages of helium ($\sim 6 \times 10^5$ years), carbon, oxygen and silicon burning. Since it has lost most of its mass to the secondary, it does not fill its Roche lobe again. The companion star evolves as a young star on the main sequence, slowly burning its hydrogen core. The evolution up till this point has taken 6.7×10^6 years.

The rapidly evolving primary, after silicon burning, ends up with an iron core, which is unable to generate sufficient energy to sustain the star. Core collapse triggers a SN explosion, removing a significant amount of material, ΔM , from the binary, where M is the total mass of the binary system before the SN explosion. The SN explosion radically changes the shape of the orbit.

The eccentricity for the post-SN eccentricity is determined by (e.g. Boersma (1961) and Kawaler et al. (1996, p. 473))

$$e = \frac{\Delta M}{M_p + M_s - \Delta M}, \quad (2.48)$$

where M_p and M_s are the masses of the objects before the SN, and ΔM is the mass lost during the SN. In this scenario the orbital distance of the circular pre-SN orbit becomes the periastron distance in the new more eccentric post-SN orbit. Equation 2.48 places a limit on the amount of material that can be lost from the system while still retaining a closed orbit ($e < 1$). Equation 2.48 shows that $e \leq 1$ if the change in mass $\Delta M \leq 0.5$. It is for this reason that the models for binary evolution assume that there is a period of mass transfer before the SN. If the progenitor of the NS or BH in an HMXB had not lost most of its mass to its companion star, the SN explosion would remove too much mass from the system and the orbit would “break”. There is observational evidence for this in the form of the Be stars. HMXBs, such as the system containing the radio pulsar PSR B125963, (see for e.g. Aharonian et al. (2005) for the recently detected gamma-ray emission), is eclipsed by the disc-like outflow of the rapidly rotating optical companion. The Be star has a spin period close to its break-up speed because high mass transfer during the evolution of the system has resulted in spin-up due to angular momentum transfer.

The optical star in the binary system now changes roles. No longer does material accrete onto it, but now it becomes the mass donor, supplying the material for accretion onto the compact object. This is what is now considered a HMXB, with a less massive compact object accreting

^{††}If this change is extreme, the orbit could shrink so much that the less massive star could enter the outer envelope of the mass donor. This would radically change the orbit of the binary system.

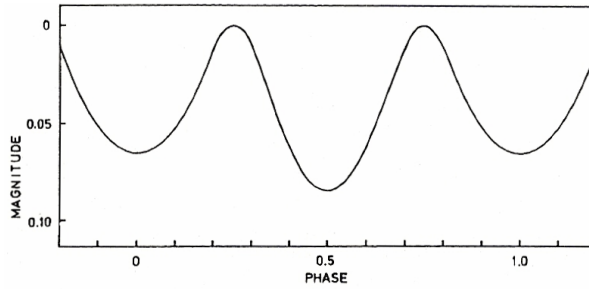


Figure 2.24: Theoretical ellipsoidal optical light curve for an HMXB (see Lewin et al. (1995, Chp. 2) and references therein).

mass from a more massive optical star.

The optical companion also proceeds along its evolutionary path, growing in size until it explodes in a SN. The result is a binary system consisting of two compact objects. The first such system, a binary pulsar PSR 1913+16, was discovered by Hulse and Taylor (1975).

2.6 Observational Properties of HMXBs

2.6.1 Optical Observations

HMXBs are dominated in the optical wavelength by the optical stars. The observations show that the properties of these stars are very similar to the properties of single stars. The HMXBs can be divided into two groups (discussed in Section 1.1) based on the optical companions, i.e. the O-type and Be-type stars.

The gravitational pull (effective gravity) of the compact mass accretor on the more massive mass donor which fills, or nearly fills, its Roche lobe, results in a pear-shaped distortion of the mass donor. This results in a (so-called) ellipsoidal variation of the optical light curve with two maxima and minima for each orbital period. Figure 2.24 shows the theoretical light curve. This shape occurs because the elongation of the optical companion means that during the binary orbit there is a variation in the area that is observed. Since the area is proportional to the luminosity, this relates to an observed variation. The minimum at phase 0.5 is less luminous than that at phase 0/1 because the increase in distance and the decrease in surface gravity at the L_1 point results in a decrease in the optical luminosity. Since the effect is only dependent on the orbital period and the shape of the optical star, the scaling effect can be modelled in terms of M_{opt} , a , i and L_{bol} (the bolometric luminosity), and the shape can be modelled by q , Ω and i .

The x-ray emission from the compact object influences the star by heating it. This heating of the star can disrupt the stellar wind and outer atmosphere. The X-ray emission is partly reflected and partly absorbed and then re-emitted at lower frequency. This has the effect of heating up the region of the star near the L_1 point (Figure 2.25). As a result the observed luminosity will be higher at phase 0.5 than predicted, as the heating of the stellar surface will

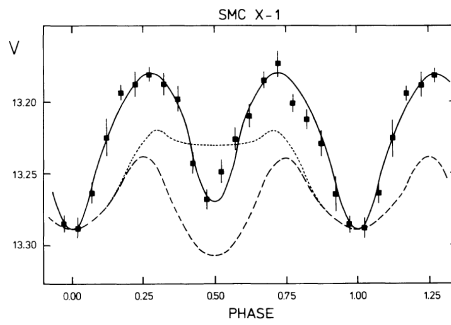


Figure 2.25: V band light curve for SMC X-1. The dashed line represents the theoretical ellipsoidal orbital modulation, the dotted line includes the effect of X-ray heating, while the solid line takes into account X-ray heating and the effect of an accretion disc (Tjemkes et al., 1986).

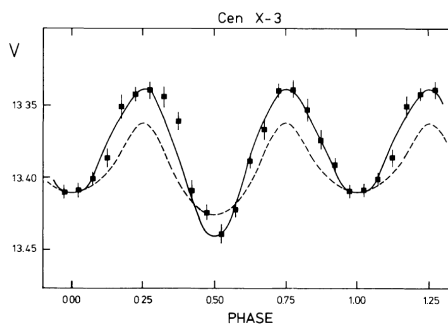


Figure 2.26: V band light curve for Cen X-3. The dashed line represents the theoretical ellipsoidal orbital modulation, while the solid line takes into account X-ray heating and the effect of an accretion disc (Tjemkes et al., 1986).

increase the luminosity.

The ellipsoidal shape is also influenced by accretion discs, where additional light from the disc and an eclipse of the star can increase or decrease the luminosity respectively.

As way of an example Figures 2.25 and 2.26 show the V band light curve of SMC X-1 and Cen X-3/V779 Cen respectively. Both exhibit a double wave shape that is not completely ellipsoidal, but which can be modelled by taking into account the effects of X-ray heating and the accretion disc (Tjemkes et al., 1986). For a more detailed review of the ellipsoidal model see Lewin et al. (1995, pp. 63-67) and references therein.

2.6.2 Spectroscopic

Spectroscopically HMXBs are dominated by the optical mass donor, but the effect of the X-ray source can affect the stellar wind of the companion, influencing the spectroscopy. A large number of HMXBs (see Lewin et al. (1995, pp. 68-70) and references therein) show He II $\lambda 4686$ emission lines, an emission line only associated with Of type stars (Conti and Alschuler, 1971).

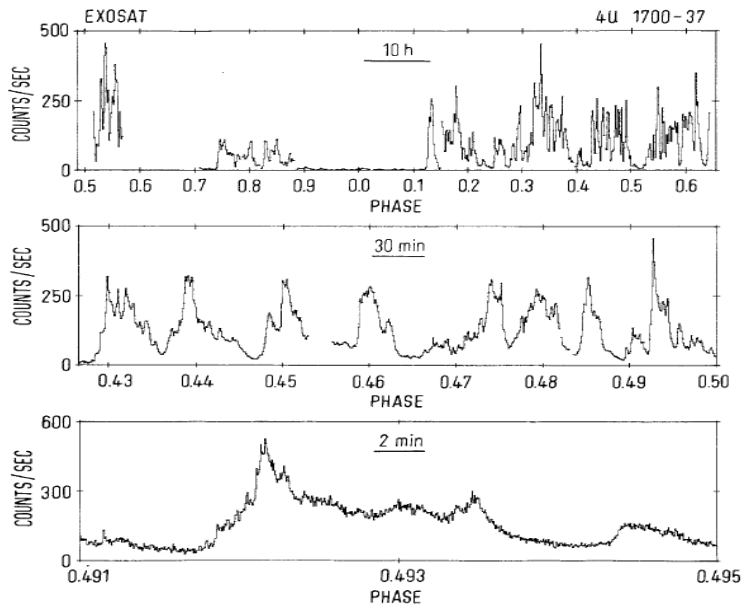


Figure 2.27: EXOSAT observation of X1700-37 (2 – 10 keV) (Gottwald et al., 1986).

Observations show that this emission must occur within the Roche lobe but lies slightly behind the accretion stream because of the observed phase shift in arrival time.

A second emission line $H\alpha$ is associated with the wind in HMXBs. Variations of the $H\alpha$ have been used to estimate changes in the stellar wind density. For a recent example of a wind loss model based on the $H\alpha$ line see Puls et al. (1996).

2.6.3 X-ray Observations

The X-ray emission from HMXBs is dependent on a number of factors. Since the systems are powered by accretion X-ray emissions from HMXBs are dependent on this. Especially in wind accretion systems a large amount of information about the stellar wind is available from this emission. This section will look at some of the observed X-ray properties. For a more detailed discussion see for example White (1989).

Supergiant X-ray binaries

The lower luminosity SXRBs tend to show flaring activities in the X-ray emission. An example is X1700-37 (Figure 2.27) that shows clear flaring events. The absence of data between phase 0.6–0.7 is due to a lack of observation points while the eclipse is clearly visible between 0.9 and 0.1. These flaring events and the luminosity can be explained in terms of inhomogeneous stellar wind accretion (Conti, 1978; White et al., 1983).

The observed absorption properties also revealed characteristic properties of this binary.

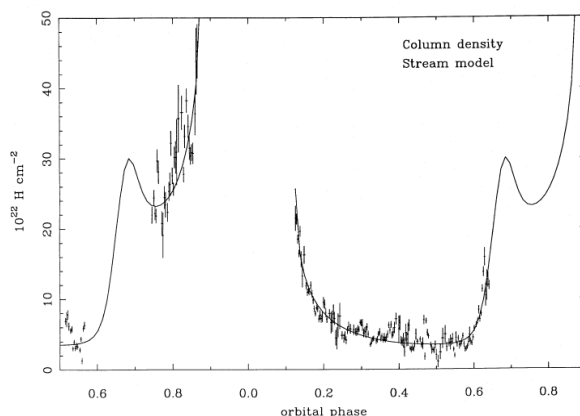


Figure 2.28: The absorption profile of X1700-37 (Haberl, White, and Kallman, 1989). The solid line is a fit using the CAK velocity law (Castor, Abbott, and Klein, 1975).

Figure 2.28 shows the absorption seen in the X-ray observations of X1700-37 plotted against orbital phase. These observations show a higher absorption before the eclipse begins (phase 0.9) as compared to the absorption after the eclipse (phase 0.1). This has been explained in terms of a gas stream that may be slightly behind the compact object and a CAK velocity law (Castor, Abbott, and Klein, 1975).

The higher luminosity systems appear to have very steady X-ray luminosities, for example Cen X-3 (Figure 2.29). With the exception of the eclipse around phase 0, the X-ray flux is very stable. This is not consistent with a wind accretion system where flaring events are expected to occur as a result of the variation in the accretion rate (Conti, 1978). This appears to point to the presence of an accretion disc, which due to the smoothing effect it would have on accretion, could explain the very stable X-ray emission. While these systems do not exhibit flaring events, they do show periods of high and low states, where the luminosity of the system can change by several orders of magnitude.

In systems like Cen X-3 the absorption spectrum is dominated by the effect of the accretion disc on the emission.

Be-type X-ray Binaries

Be-type XRBs show outbursts in the X-ray emission. These have been classified into Type I outbursts that repeat with orbital period and Type II outbursts that are single events. Type I outbursts show increases in luminosity > 100 while Type II outbursts show increases in luminosity of $100 - 1000$. It is believed that these outbursts are caused by periods of increased accretion.

The purpose of the discussion presented in this chapter was to put into context some of the basic properties of XRBs. The next chapter will review the most relevant radiation processes and additional theoretical considerations required to evaluate the modelling presented in this study.

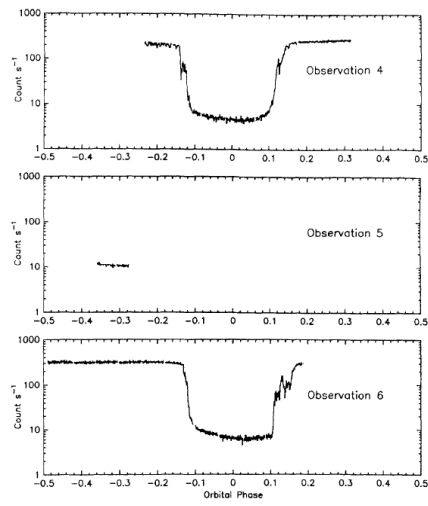


Figure 2.29: EXOSAT observation of Cen X-3 (2–7 keV) (Day, 1988).

Chapter 3

Radiation and Mass Outflow Theory

3.1 Radiation Theory

The broad multi-wavelength emission profile of LS 5039 (Figure 4.1), which apart from the black body component associated with the optical star, is dominated by non-thermal synchrotron radiation, with a possible inverse Compton (IC) contribution at energies $\epsilon \gtrsim 1$ GeV. In order to properly interpret this broad multi-wavelength profile, since the compact object can be either a BH or a NS, a rather broad discussion related to relevant radiation and mass outflow scenarios will be presented. The purpose of this discussion is to provide a broad theoretical framework against which the model calculations (Chapter 4) can be evaluated.

The radiation mechanisms are summarized following the discussion presented in Lang (1974, pp. 21-39, 450, 453, 467-468). This discussion is then followed by a brief review of outflow mechanisms relevant to both NS and BH binaries.

3.1.1 Black Body Radiation

The Rayleigh-Jeans solution to the black body problem predicted an emission spectrum

$$u(\nu) d\nu = \frac{2n_\nu^2 \nu^2 kT}{c^2},$$

where n_ν is the index of refraction, and ν is the frequency. This proved to be incompatible with the observed black body emission since the solution implies $I \propto \nu^2$, suggesting that the intensity will increase as ν^2 instead of falling away to zero for $\nu \rightarrow \infty$. The solution to this *ultraviolet catastrophe*, as it was known, was provided by Max Planck. His solution implied that the photon

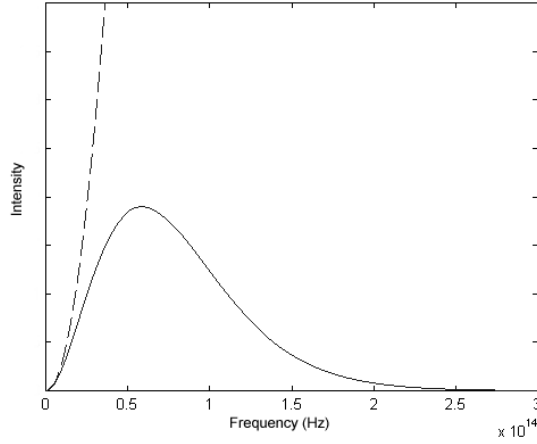


Figure 3.1: The Planck (solid line) and Rayleigh-Jean (dashed line) black body curves plotted together for $T = 1000$ K.

energy emitted by a black body in thermal equilibrium only exists in discrete quanta given by

$$\epsilon = nh\nu \quad n = 0, 1, 2, \dots$$

where $h = 6.626 \times 10^{-27}$ erg sec, is Planck's constant. The intensity profile of such a black body can be characterized by the Planck spectrum, i.e.

$$I = \frac{2h\nu^3}{c^2(e^{h\nu/kT(R)} - 1)} \quad \text{erg s}^{-1} \text{ cm}^{-2} \text{ Hz}^{-1} \text{ sr}^{-1}. \quad (3.1)$$

Since $e^{h\nu/kT(R)} \rightarrow \infty$ for $h\nu \gg kT$, this results in $I \rightarrow 0$ (Figure 3.1). Planck's equation allows for an accurate prediction of the black body spectrum from a body at temperature T .

The flux density measured on Earth from an astronomical object located at a distance d , is related to its intensity by (Swihart, 1968, p. 246)

$$F_\nu = \pi I(\nu) \left(\frac{R}{d} \right)^2.$$

This implies that for an astronomical source where the radius, distance and surface temperature are known, the flux density is

$$\nu F_\nu = 2\pi \left(\frac{R}{d} \right)^2 \frac{h}{c} \frac{\nu^4}{e^{h\nu/kT} - 1}.$$

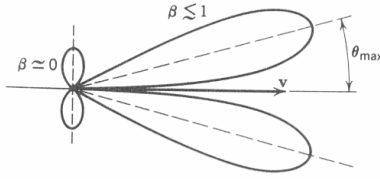


Figure 3.2: Radiation beaming for $\beta \approx 1$ and $\beta \lesssim 1$. Note that $\beta \lesssim 1$ is scaled by a factor 10^2 (Jackson, 1998, p. 669).

3.1.2 Synchrotron Radiation / Cyclotron Radiation

Particles in motion in a magnetic field spiral around the magnetic field lines and radiate energy. This is known as cyclotron radiation when the particles are non-relativistic, and synchrotron radiation when the particles are relativistic. The total power that is radiated by a single particle is

$$\frac{dP}{d\Omega} = \frac{e^2 \dot{v}^2}{4\pi c^3} \frac{\sin^2 \theta}{(1 - \beta \cos \theta)^5} \quad (3.2)$$

per solid angle, where $\beta = v/c$, v is the velocity of the particle, \dot{v} is the acceleration, and θ is the angle between the line of sight and the direction of v , defined as $\hat{v} = \frac{v}{|v|}$. At non-relativistic velocities, $\beta \rightarrow 0$, and Equation 3.2 reduces to the classical Larmor power distribution. For relativistic velocities the distribution is beamed and focused into a narrow cone of size (Figure 3.2)

$$\theta = \gamma^{-1} = mc^2 E^{-1} = 8.2 \times 10^{-7} E^{-1} \text{ radians,}$$

where E is the relativistic energy of the particle. For an electron spiralling in a magnetic field, the gyration frequency is given by

$$\omega_H = \frac{eH}{\gamma mc} \sin \psi, \quad (3.3)$$

where H is the magnetic field strength, e is the charge of the electron, and ψ is the pitch angle, defined as the angle between \hat{H} and \hat{v} . The radius of the circular path followed by the electron is given by

$$r_H = \frac{v}{\omega_H} = \frac{\gamma mc}{eH} \frac{v}{\sin \psi} \quad (3.4)$$

or

$$r_H \approx 2 \times 10^9 EH^{-1} \text{ cm}$$

when $v \approx c$ and $\sin \psi \approx 1$. For non-relativistic particles, $\gamma \rightarrow 1$, and Equations 3.3 and 3.4 reduce to the Larmor frequency and radius, i.e.

$$\omega_L = \frac{qB}{mc} \quad (3.5)$$

and

$$r_L = \frac{v_\perp}{\omega_L}. \quad (3.6)$$

It is interesting to note that the Larmor frequency can be written independently of the radius and can be solved in terms of the magnetic field strength, charge, mass and speed of light.

The critical frequency is defined as the frequency at which the emission spectrum reaches a maximum. In the case of synchrotron radiation this is given by

$$\begin{aligned} \nu_c &= \frac{3}{4\pi} \frac{eH}{mc} \gamma^2 \sin \psi \\ &\approx 6.266 \times 10^{18} H E^2 \sin \psi \text{ Hz}, \end{aligned} \quad (3.7)$$

where $E = \gamma m_e c^2$ is the energy of the electron.

It can be shown that the total power per frequency interval ν to $\nu + d\nu$ radiated by a single particle is then

$$P(\nu) = \frac{\sqrt{3}e^3}{mc^2} H_\perp \frac{\nu}{\nu_c} \int_{\nu/\nu_c}^{\infty} K_{5/3}(\eta) d\eta \quad \text{erg s}^{-1} \text{ Hz}^{-1}, \quad (3.8)$$

where $\eta = \nu/\nu_c$. This translates, for the different regimes, i.e. $\eta \gg 1$ and $\eta \ll 1$, to

$$P(\nu) \approx 5.04 \times 10^{-22} H_\perp \left(\frac{\nu}{\nu_c} \right)^{1/3} d\nu \quad \text{erg sec}^{-1} \text{ Hz}^{-1} \quad \text{for } \nu \ll \nu_c$$

and

$$P(\nu) \approx 2.94 \times 10^{-22} H_\perp \left(\frac{\nu}{\nu_c} \right)^{1/2} e^{-\nu/\nu_c} d\nu \quad \text{erg sec}^{-1} \text{ Hz}^{-1} \quad \text{for } \nu \gg \nu_c$$

where H_\perp is the component of H that is perpendicular to \hat{v} , and $K_\nu(\nu)$ is the modified Bessel function of the second kind (e.g. Arfken (1985, pp. 610-615)). To determine the emission from an ensemble of synchrotron radiating electrons it is necessary to consider the volume emissivity*

$$\varepsilon(\nu) = \int P(\nu) N(E) dE, \quad (3.9)$$

where $N(E) dE$ is the number of electrons per unit volume per unit solid angle along the line of sight whose energies lie between E and $E + dE$. It is generally assumed that the distribution for synchrotron radiation follows the power law

$$N(E) dE = K E^{-\gamma} dE, \quad (3.10)$$

where K is a constant and γ is known as the power index. Combining Equations 3.8, 3.9 and

*The volume emissivity is defined as the power per frequency per volume per solid angle.

3.10 gives the intensity of the emission

$$\begin{aligned}
I(\nu) &= l\varepsilon(\nu) = Kl\alpha(\gamma)\frac{\sqrt{3}}{8\pi}\frac{e^3}{mc^2}\left[\frac{3e}{4\pi m^3c^5}\right]^{(\gamma-1)/2}H_{\perp}^{(\gamma+1)/2}\nu^{-(\gamma-1)/2} \\
&\approx 0.933\times 10^{-23}\alpha(\gamma)KlH_{\perp}^{(\gamma+1)/2}\left(\frac{6.26\times 10^{18}}{\nu}\right)^{(\gamma-1)/2}\text{erg sec}^{-1}\text{cm}^{-2}\text{Hz}^{-1}\text{rad}^{-2},
\end{aligned}
\tag{3.11}$$

where l is the dimension of the radiating region along the line of sight and

$$\alpha(\gamma) = 2^{(\gamma-3)/2}\frac{\gamma + \frac{7}{3}}{\gamma + 1}\Gamma\left(\frac{3\gamma - 1}{12}\right)\Gamma\left(\frac{3\gamma + 7}{12}\right),$$

valid for $\gamma > \frac{1}{3}$, and Γ is the standard Gamma function (see for example Arfken (1985, Chp. 10)). Equation 3.11 implies that

$$I \propto \nu^{\alpha},$$

where

$$\alpha \equiv -\frac{\gamma - 1}{2},$$

is the spectral index.

It is also possible to determine the strength of the magnetic field by considering the circular polarization of the synchrotron radiation, i.e.

$$\begin{aligned}
\pi_0 &= \sqrt{\frac{8}{3}}\frac{\cot\vartheta}{F(\nu/\nu_c)}\left(\frac{\nu_H \sin\vartheta}{\nu}\right)^{1/2}\left\{\left(\frac{\nu}{\nu_c}\right)^{3/2}K_{1/3}\left(\frac{\nu}{\nu_c}\right)\right. \\
&\quad \left.+ \left[2 + \frac{\varphi'(\vartheta)}{\varphi(\vartheta)}\tan\vartheta\right]\left(\frac{\nu}{\nu_c}\right)^{-1/2}\left[\left(\frac{\nu}{\nu_c}\right)K_{2/3}\left(\frac{\nu}{\nu_c}\right) - \frac{1}{2}F\left(\frac{\nu}{\nu_c}\right)\right]\right\}
\end{aligned}$$

where $\vartheta = \psi - \delta$. Here ψ is the pitch angle, δ is the angle between the line of sight and \hat{v} , $\varphi(\theta)$ is the number of electrons within the solid angle $d\Omega = 2\pi\sin\theta d\theta$, for the range θ to $\theta + d\theta$, $\varphi'(\theta) = \frac{d}{d\theta}\varphi(\theta)$, $K_{\nu}(\nu)$ is the modified Bessel function of the second kind and $F(x)$ is

$$F(x) = x \int_x^{\infty} K_{5/3}(\eta) d\eta.$$

Table 3.1 show solutions to $F(x)$ for certain values of x .

3.1.3 Inverse Compton Scattering

In the Compton effect, as was originally shown by A.H. Compton, a photon collides with an electron and imparts energy to it (Figure 3.3). In the case of a stationary electron the change in the incident photon's wavelength is

$$\Delta\lambda = \frac{h}{mc}(1 - \cos\phi),$$

Table 3.1: Solution to the function $F(x) = x \int_x^\infty K_{5/3}(\eta) d\eta$ and $F_n(x) = xK_{2/3}(x)$ (Ginzburg and Syrovatskii, 1965).

x	$F(x)$	$F_n(x)$	x	$F(x)$	$F_n(x)$
0.00000	0.00000	0.00000	0.90000	0.69400	0.52100
0.00100	0.21300	0.10700	1.00000	0.65500	0.49400
0.00500	0.35800	0.18400	1.20000	0.56600	0.43900
0.01000	0.44500	0.23100	1.40000	0.48600	0.38600
0.02500	0.58300	0.31200	1.60000	0.41400	0.33600
0.05000	0.70200	0.38800	1.80000	0.35400	0.29000
0.07500	0.77200	0.43800	2.00000	0.30100	0.25000
0.10000	0.81800	0.47500	2.50000	0.20000	0.16800
0.15000	0.87400	0.52700	3.00000	0.13000	0.11100
0.20000	0.90400	0.56000	3.50000	0.08450	0.07260
0.25000	0.91700	0.58200	4.00000	0.05410	0.04700
0.29000	0.91800	0.59200	4.50000	0.03390	0.02980
0.30000	0.91800	0.59600	5.00000	0.02140	0.01920
0.40000	0.90100	0.60700	6.00000	0.00850	0.00770
0.50000	0.87200	0.60300	7.00000	0.00330	0.00310
0.60000	0.83200	0.59000	8.00000	0.00130	0.00120
0.70000	0.78800	0.57000	9.00000	0.00050	0.00047
0.80000	0.74200	0.54700	10.00000	0.00019	0.00018

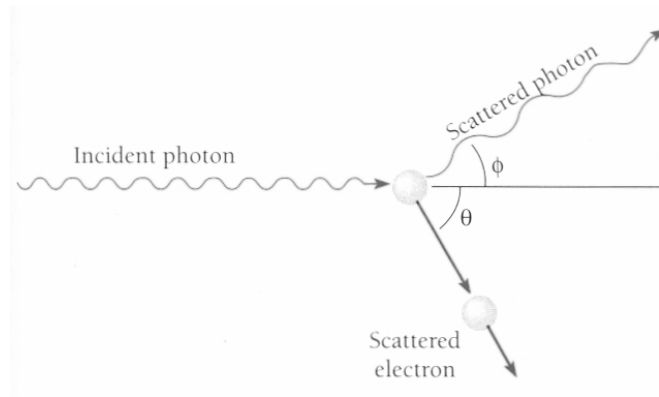


Figure 3.3: Geometry of Compton scattering for a stationary electron (adapted from Beiser (2003, p. 75)).

where the angle ϕ is defined as the photon's deflection from its original trajectory (see Figure 3.3). In IC scattering the reverse occurs and the energy of a relativistic electron is imparted to a photon. This results in a loss of energy of the electron along the path dx given by,

$$-\frac{dE_e}{dx} = \int \sigma_c(E'_\gamma, E_\gamma) N(E_\gamma) E'_\gamma dE'_\gamma dE_\gamma.$$

Here $E_e = \gamma m_e c^2$ is the initial energy of the electron, $E_\gamma = h\nu$ and $E'_\gamma = h\nu'$ are the initial and final energies of the photon respectively, $\sigma_c(E'_\gamma, E_\gamma)$ is the scattering cross section and $N(E_\gamma)$ is the number density of photons of energy E_γ such that the photon energy density is $U \approx h\nu N(h\nu)$. Using the ratio $q = (\gamma h\nu)/(m_e c^2)$, the proper relativistic expression for the IC cross section, i.e. the so-called Klein-Nishina expression, is

$$\begin{aligned} \sigma_c &= \frac{3}{4} \sigma_T \left\{ \frac{1+q}{q^3} \left[\frac{2q(1+q)}{1+2q} - \ln(1+2q) \right] + \frac{1}{2q} \ln(1+2q) - \frac{1+3q}{(1+2q)^2} \right\} \\ &\approx \sigma_T \left(1 - \frac{2\gamma h\nu}{m_e c^2} \right) \quad \text{for } q \ll 1 \\ &\approx \frac{3}{8} \sigma_T \frac{m_e c^2}{\gamma h\nu} \left[\frac{1}{2} + \ln \left(\frac{2\gamma h\nu}{m_e c^2} \right) \right] \quad \text{for } q \gg 1, \end{aligned} \quad (3.12)$$

where σ_T is the Thomson scattering cross section, i.e.

$$\sigma_T = \frac{8\pi e^4}{3m_e^2 c^4} \approx 6.65 \times 10^{-25} \text{ cm}^2.$$

The resulting maximum energy for the scattered photon is

$$E'_\gamma \approx \gamma^2 h\nu \quad \text{for } q \ll 1$$

and

$$E'_\gamma \approx \gamma m_e c^2 \quad \text{for } q \gg 1, \quad (3.13)$$

with the appropriate cross section. This translates to a resultant frequency of the scattered photon (ν') relative to the initial photon (ν), which is

$$\nu' \approx \gamma^2 \nu \quad \text{for } q \ll 1$$

and

$$\nu' \approx \frac{\gamma m_e c^2}{h} \quad \text{for } q \gg 1 \quad (3.14)$$

respectively.

These expressions show that in the Thomson regime ($q \ll 1$) the energy of the scattered photon increases by a factor γ^2 with respect to the incident photon. In the ultra-relativistic case ($q \gg 1$), the electron is believed to transfer all its kinetic energy to the scattered photon

resulting in $\epsilon_\gamma \propto \gamma m_e c^2$.

3.1.4 Gamma-ray absorption

While gamma-ray absorption is not a radiation mechanism, it directly effects the observed emission in systems like LS 5039 where the gamma-ray emission passes through a dense photon field. The result is a high opacity at gamma-ray wavelengths. This effect must be considered when modelling phenomena such as the orbital modulation of the high energy gamma-ray emission.

Pair production through photo-photon collision

If two photons possess sufficient energy, a collision between them can result in the production of an electron-positron pair (rest mass energy of $E = m_e c^2 \approx 8.19 \times 10^{-7}$ ergs $\approx 5.11 \times 10^5$ eV). The required energy is angular dependent. Consider two photons with energies E_1 and E_2 moving in the directions $\hat{\mathbf{e}}_1$ and $\hat{\mathbf{e}}_2$ respectively, the required energy for pair production is then (e.g. Dubus (2006a); Gould and Schröder (1967))

$$E_1 E_2 \geq \frac{2(m_e c^2)^2}{(1 - \hat{\mathbf{e}}_1 \cdot \hat{\mathbf{e}}_2)}.$$

The cross section for this to occur is (e.g. Lang (1974, p. 450))

$$\sigma(E_1, E_2) = \frac{\pi r_0^2}{2} (1 - \xi^2) \left[2\xi(\xi^2 - 2) + (3 - \xi^4) \ln \left(\frac{1 + \xi}{1 - \xi} \right) \right],$$

where

$$r_0 = \frac{e^2}{mc^2} \approx 2.818 \times 10^{-13} \text{ cm}$$

is the classical electron radius, and

$$\xi = \frac{v}{c} = \left[1 - \frac{(m_e c^2)^2}{E_1 E_2} \right]^{1/2},$$

is the velocity in the centre of mass reference frame of the electron after production.

Figure 3.4 shows calculations done by Dubus (2006a) on gamma-ray absorption around a $T = 40000$ K, $R = 10 R_\odot$ star, parameters which are consistent with LS 5039.

Pair Cascade

Pair cascade, while not being examined, should be mentioned here. After pair production the electron-positron pair that has been created can possess sufficient energy to up-scatter additional photons through IC scattering. These up-scattered photons may have enough energy to repeat the process. This lowers the opacity around optically dense regions such as in Figure 3.4.

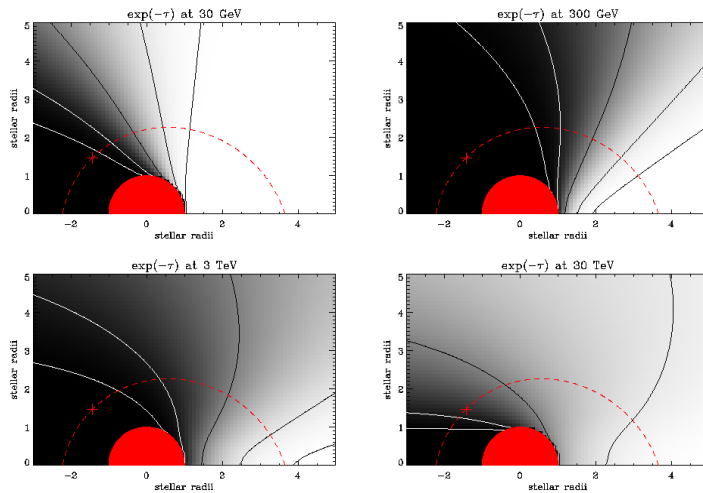


Figure 3.4: Gamma-ray absorption in a massive star with temperature 40000K and radius $10R_{\odot}$, for four different gamma-ray energies. The grey-scale is an indication of the gamma-ray absorption, the darker the region the more absorption occurs. The contour lines show the position of 1%, 10%, 50%, 90% and 99% absorption. The dotted line represents the orbital path of LS 5039 (Dubus, 2006a).

Since the H.E.S.S.[†] source LS 5039, based upon its jet-like outflow, has been classified as a microquasar system, a brief discussion of mass outflow processes of relevance for all types of HMXBs will be presented. The purpose of this discussion is to indicate that outflows are associated with NS and BH binaries and caution against the classification of a system based upon this phenomenon. The discussion is initiated with an introduction to outflows from isolated pulsars, from where it is extended to disc accreting pulsars and BHs.

3.2 Pulsar Wind Nebula

The PWN model was developed to explain how isolated pulsars, in particular the Crab pulsar, interacted with the nebula surrounding it. Since then, additional PWN candidates have been found and there are currently 40 – 50 known systems in the Milky Way and Magellanic Clouds. Additional variations to the standard PWN model have been introduced over the years, most importantly the bow shock nebulae created by high velocity pulsars moving through their SNR or through the ISM.

These models were initially applied and calibrated to the Crab Nebula with a large degree of success. Observations of the Crab Nebula show that the energy required to power the observed radiation and expansion of the nebula is very similar to the energy loss due to spin-down. This

[†]H.E.S.S.: The High Energy Spectroscopic System, is a gamma-ray telescope in Namibia.

confirmed the idea that the central pulsar is powering the nebula. The PWN model provides a mechanism for connecting the spin-down power with the properties of the observed nebula. The basic assumption of this model is that a relativistic positronic wind is created by the pulsar which terminates in a shock at a distance R_S , creating a cooling nebula of synchrotron radiation.

This section will consider some of the aspects of the PWN model, and examine specifically its application to HMXBs. It will begin by considering some of the standard models of an isolated pulsar in a SNR, including the pulsar wind, the Kennel-Coroniti model and the formation of bow-shocks, before proceeding to their application in HMXBs. The formation of jets in PWNe will be considered in the section on jet formation (Section 3.3.3). For details on the initial models of PWN see for example Rees and Gunn (1974) and Kennel and Coroniti (1984a,b), and for a recent review paper of PWNe see Gaensler and Slane (2006).

3.2.1 The Pulsar Wind

While the pulsar wind model can explain much of the observable features of pulsar nebulae, the exact cause of the pulsar wind is unclear. The Goldreich-Julian equations (Equations 2.40 & 2.41) show that a pulsar will not exist in a vacuum and that it must be surrounded by a “charge atmosphere”. The model implies that charged particles will flow from the surface of the pulsar along open magnetic field lines out to the boundary zone. This process forms the basis of all pulsar wind models.

Rees and Gunn (1974) expanded on the idea of the “oblique rotator”[‡] (Ostriker and Gunn, 1969; Pacini, 1968) and assumed that the spin-down power is lost in three forms, namely; L_{wave} , a low frequency electromagnetic wave, L_{wind} , a positronic wind, and L_{mag} , which results from magnetohydrodynamic dissipation through a toroidal field which connects the pulsar with the nebula surrounding it.

In general these models are more concerned with the interaction at the shock radius than the details of the acceleration mechanism. As such the pulsar wind is often simply considered as a parameter of the model. Despite this, highly accurate models of the observed emission have been developed.

It is currently believed that the acceleration of the pulsar wind occurs in the collapse of charge-separated gaps ($\mathbf{E} \cdot \mathbf{B} \neq 0$) in the region around the pulsar. These occur near the poles or in regions near the light cylinder. For an aligned rotator the maximum potential across these gaps has been shown to be (Goldreich and Julian, 1969)

$$\begin{aligned} \Delta\Phi &= \frac{1}{2} \frac{\Omega^2 R^3 B_*}{c^2} \\ &\approx 6.6 \times 10^{12} \left(\frac{B_*}{10^{12} \text{ G}} \right) \left(\frac{R}{10^6 \text{ cm}} \right)^3 \left(\frac{P}{1 \text{ sec}} \right)^{-2} \text{ V}, \end{aligned}$$

[‡]An *aligned rotator* is defined as a pulsar where the axis of the magnetic field is aligned with the spin axis. An *oblique rotator* is a pulsar where this does not occur.

where B_* is the surface magnetic field (more specifically the magnetic field at the poles).

A standard parameter of pulsar wind models is the magnetization ratio which is the ratio of the Poynting flux to the particle flux in the pulsar wind, i.e. the ratio of magnetic to kinetic energy (e.g. Dubus (2006b)),

$$\sigma = \frac{B_1^2}{4\pi n_1 \gamma_p^2 m_e c^2}$$

where B_1 [§] is the magnetic field, n_1 is the density, $m \approx m_e$ if it is assumed that the wind consists mainly of electrons and positrons, and γ_p is the Lorentz factor of the electrons/positrons. Models of the Crab Nebula require that σ is a fairly small term just upstream of the shock (e.g. Kennel and Coroniti (1984b) found a best fit of $\sigma = 0.003$).

3.2.2 The Nebula

The basis of the PWN model is that the pulsar wind terminates in a shock front that occurs when the ram pressure of the wind equals the pressure of the surrounding nebula. By considering the energy density, given by

$$\begin{aligned} \langle u \rangle &= \frac{F}{c} \\ &= \frac{\dot{E}}{4\pi R^2} \times \frac{1}{c}, \end{aligned}$$

and by equating this energy density to pressure, $P \sim \langle u \rangle$, the shock radius is found at a distance (e.g. Gaensler and Slane (2006))

$$R_S = \left(\frac{\dot{E}}{4\pi\omega c P_{Neb}} \right)^{1/2}.$$

Here \dot{E} is the spin-down luminosity of the pulsar (Equation 2.43), P_{Neb} is the pressure of the nebula and ω is the equivalent filling factor. At the shock front the particles are thermalized and cooled via synchrotron radiation.

A diagram of the model for the PWN as proposed by Kennel and Coroniti (1984a,b) is shown in Figure 3.5. In the model there are 6 regions or layers surrounding the pulsar (Kennel and Coroniti, 1984a):

- I The pulsar magnetosphere, defined as the region within the light cylinder, is represented by the central black dot.
- II Beyond the light cylinder the pulsar wind accelerates along the magnetic field lines until terminating at the shock front.

[§]A subscript 1 represents a parameter upstream of the shock, while a subscript 2, as will be used later in this discussion, represents a post-shock parameter.

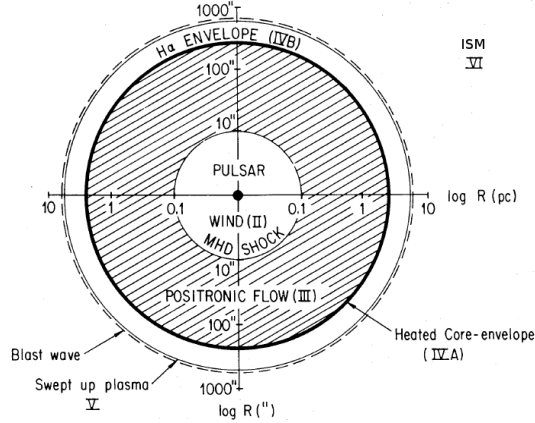


Figure 3.5: Diagram of region surrounding a pulsar up to its SNR (Kennel and Coroniti, 1984a, see the text for explanation).

III The bulk flow decelerates but the shock accelerates a fraction of the particles to high energies. Since the magnetic fields are not homogeneous behind the shock, these “heated” particles are trapped and radiate through the synchrotron process.

IV The SNR, consisting of an inner envelope (A) heated by the positronic flow and a cooling outer H_α envelope (B).

V This is surrounded by a layer of material that is left over from the SN blast wave.

VI The PWN is then surrounded by the ISM.

The emission in the positronic flow is connected to the break frequency (Ginzburg and Syrovatskii, 1965)

$$\nu_b = 10^{21} \left(\frac{B_{Neb}}{10^{-6} \text{ G}} \right)^{-3} \left(\frac{t}{10^3 \text{ years}} \right)^{-2} \text{ Hz},$$

where B_{Neb} is the magnetic field strength in region III, and t is the synchrotron life time. The higher the frequency radiated by a particle is above ν_b , the less the distance it flows towards the ISM. The result is that the observed size of the nebula shrinks with increasing frequency. This is clearly seen in the Crab Nebula (Figure 3.6) where the X-ray region is much smaller than the radio region. This effect is not as visible in systems such as PWN 3C 58 where B_{Neb} has a lower value (Figure 3.7).

The Dubus (2006b) application of the PWN model to high mass binary systems relies on a number of assumptions made in the Kennel and Coroniti (1984a,b) model. As such, a few of the most important concepts will be briefly discussed.

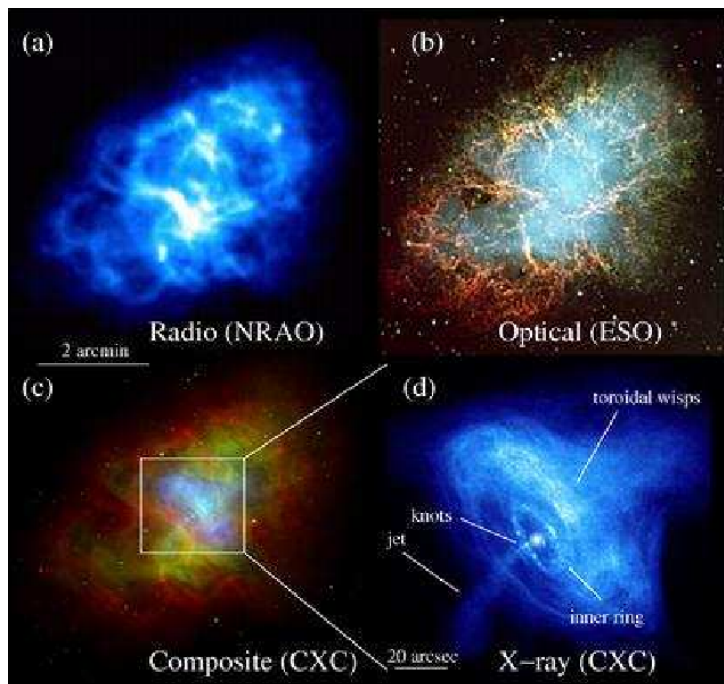


Figure 3.6: Crab Nebula in **a.** radio, **b.** optical and **d.** X-ray. **c.** shows a composite image of the three wavelengths (reproduced from Gaensler and Slane (2006)). Note that **d.** is scaled differently.

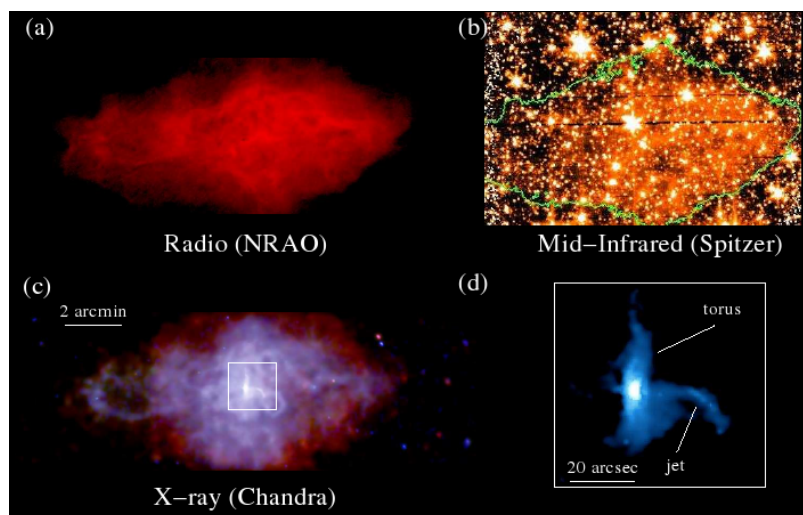


Figure 3.7: PWN 3C 58 in multiple wavelengths (reproduced from Gaensler and Slane (2006)). (a) Radio emission (Reynolds and Aller, 1988). (b) Infrared synchrotron emission. (c) X-ray emission; blue is the synchrotron emission and red is the thermal emission. (d) Magnified image of the jet and torus (Slane et al., 2004).

3.2.3 Kennel-Coroniti Model

Calculations by Kennel and Coroniti (1984b) show that the magnetohydrodynamic (MHD) wind shock occurs at a distance $R_S = 3 \times 10^{17}$ cm in the Crab Nebula, at which point the flow is thermalized and follows a power-law energy spectrum distribution, e.g. Kennel and Coroniti (1984b) & McCray et al. (1977). The post-shock plasma and magnetic fields then flow out to the edge of the nebula at non-relativistic speeds. By assuming the shock front obeys the Rankine-Hugoniot equations, the authors describe their model in terms of six parameters, i.e.

1. L : the pulsar luminosity
2. R_S : the shock radius
3. R_n : the radius of the nebula
4. σ : ratio of Poynting flux to particle energy flux
5. u_1 : wind four velocity
6. $2\alpha + 1$ spectral index of the downstream particle energy distribution.

In the case of the Crab Nebula, it is possible to measure or estimate a number of these parameters. Since the pulsar and SNR are visible, the pulsar luminosity, L , shock radius, r_s , and radius of the nebula, r_n , are directly measurable. It is then also possible to find a good approximation for the ratio σ (approximately 0.003 in this case). In the upstream region the magnetic field strength is

$$B_1 = \left[\frac{L}{cR_S^2} \frac{\sigma}{1 + \sigma} \right]^{1/2}.$$

In the remainder of the discussion of the Kennel-Conroniti model the energy of the particles is given in terms of

$$\epsilon = \frac{E}{mc^2}$$

and ϵ' and ϵ'' are defined as the minimum and maximum energy the particle obtains. Certain distances will also be written in terms of a normalized distance

$$z = \frac{R}{R_S}$$

and velocities in terms of

$$u(z) = u_2 v.$$

Total Luminosity

By assuming that the power radiated from a single electron/positron is

$$p(\epsilon, \theta) = \frac{2}{3} \left(\frac{e^4}{m^2 c^3} \right) \epsilon^2 B^2 \sin^2 \theta,$$

Kennel and Coroniti (1984b) showed that the volume emissivity is

$$j(z) = J(\alpha) \frac{z^2}{(vz^2)^{3+(2\alpha/3)}} \int_{\epsilon'}^{\epsilon''} \left(\frac{1}{\epsilon} - \frac{1}{\epsilon_\infty} \right)^{2\alpha-1} d\epsilon,$$

where ϵ_∞ is the maximum possible energy in the system[¶], and

$$J(\alpha) = \frac{4}{9} \left(\frac{e^4}{m^2 c^3} \right) (\gamma_2 n_2 B_2^2) K(\alpha)$$

where γ_2 and n_2 are in the observers frame and

$$K(\alpha; \epsilon'_2, \epsilon''_2) = \frac{2\alpha(\epsilon'_2 \epsilon''_2)^{2\alpha}}{(\epsilon''_2)^{2\alpha} - (\epsilon'_2)^{2\alpha}}.$$

The total synchrotron luminosity for the PWN is given by

$$\begin{aligned} L_S &= 4\pi R_S^3 \int_1^{R_n/R_S} j(z) z^2 dz \\ &= \hat{L}(\alpha) \int_1^{R_n/R_S} \frac{z^4}{(vz^2)^{3+(2\alpha/3)}} dz \int_{\epsilon'}^{\epsilon''} \left(\frac{1}{\epsilon} - \frac{1}{\epsilon_\infty} \right)^{2\alpha-1} d\epsilon \end{aligned} \quad (3.15)$$

where

$$\hat{L}(\alpha) = \frac{4}{9} \frac{e^4}{m^3 c^7} \left(\frac{L^2}{r_S u_1} \right) \frac{\sigma}{(1+\sigma)^2} \left(\frac{\gamma_2}{u_2} \right)^3 K(\alpha) \quad (3.16)$$

if $\epsilon''_2 \gg \epsilon'_2$ and $K(\alpha) \approx 2\alpha(\epsilon'_2)^{2\alpha}$. Figure 3.8 shows an example of the luminosities dependence on σ for $\alpha = 1$.

Spectral Distribution

The final consideration is the distribution of the synchrotron spectrum. The radiation frequency at a specific spatial point is determined by the range of energies of the particles and the field strength at that point. Since the critical frequency is given by (Equation 3.7)

$$\nu_c = \frac{3}{4\pi} \frac{eB}{mc} \epsilon^2 \sin \theta \text{ Hz},$$

the range of frequencies lies between $\nu_c(\epsilon') \leq \nu \leq \nu_c(\epsilon'')$, for $\sin \theta = 1$.

The luminosity at a certain frequency is determined by the volume of material radiating at that specific frequency. The authors show that under the assumption that a particle with energy ϵ , only emits synchrotron radiation at the critical frequency, so that the power radiated is

$$p_\nu(\epsilon, \theta) = \frac{2}{3} \frac{e^4}{m^2 c^3} B^2 \epsilon^2 \sin^2 \theta \delta(\nu - \nu_c),$$

[¶]This should not be confused with ϵ'' which is the maximum energy a particle obtains; ϵ_∞ is the absolute maximum energy allowable.

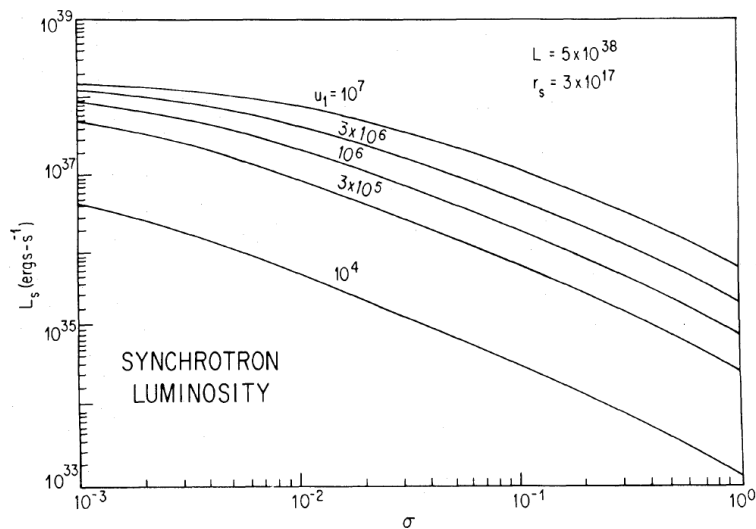


Figure 3.8: Total synchrotron luminosity for $\alpha = 1$ (Kennel and Coroniti, 1984b). The figure shows the luminosity plotted for various values of u_1 and for $R_n/R_S = 20$ and $L = 5 \times 10^{38} \text{ erg s}^{-1}$.

the spectral distribution is then given by

$$\nu L_\nu = \hat{L}(\alpha) \left(\frac{3f_{c2}}{2\nu} \right)^{\alpha-1} \int_{z_{min}}^{z_{max}} \frac{z^{3+\alpha} M(\alpha, z)}{(vz^2)^{2+(5\alpha/3)}},$$

where f_{c2} is the cyclotron frequency in the post-shock region and

$$M(\alpha, z) = \frac{3}{2} \int \frac{\alpha}{4\pi} (\sin \theta)^{\alpha+1} \left[1 - \left(\frac{\nu}{\nu(\epsilon_\infty)} \right)^{1/2} \right]^{\alpha-1} d\Omega.$$

Figure 3.9 shows an example of luminosity spectrum for $\alpha = 1$.

3.2.4 Bow Shocks

Due to the energy “kick” that occurs during the SN explosion, the pulsar normally has a proper motion relative to the SNR. This results in the PWN taking on a bow shock appearance once the pulsar has moved a sufficient distance within the SN cavity (Figure 3.10) or is already moving through the ISM (Figure 3.11).

The shock now occurs at the point where the ram pressure of the wind is balanced by the ram pressure due to the pulsar’s motion. In the direction of motion this occurs at a distance R_{w0} defined by (e.g. Gaensler and Slane (2006))

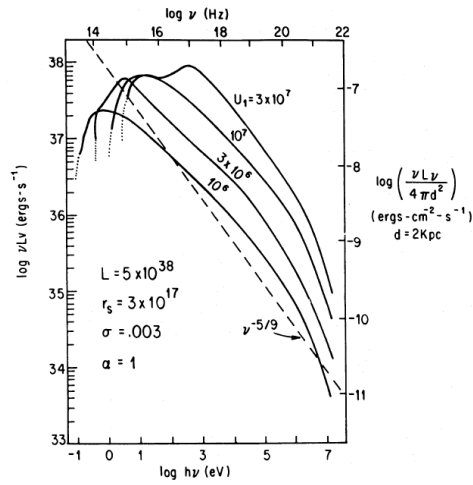


Figure 3.9: Example of a calculated luminosity spectrum for a PWN (Kennel and Coroniti, 1984b).

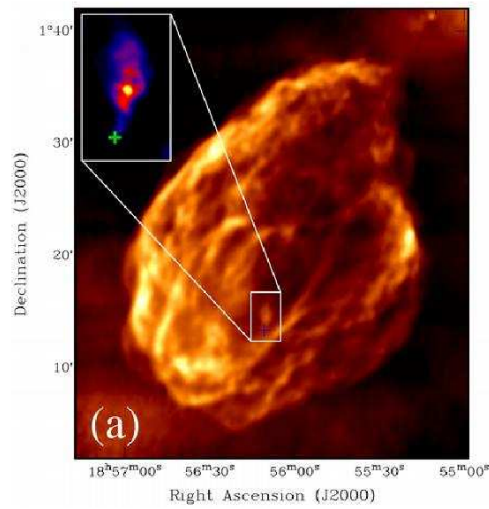


Figure 3.10: VLA image (1.4 GHz) of SNR W44 (Giacani et al., 1997). The pulsar has formed a bow-shock while moving through the SNR.

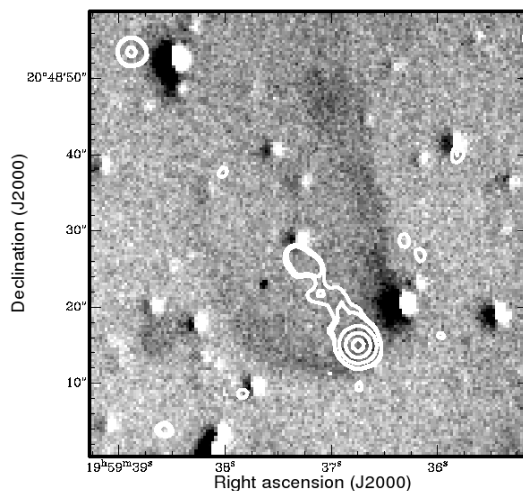


Figure 3.11: *Chandra* image (0.3-10 keV energy range) of the “Black Window” pulsar, PSR B1957+20, overlaid with H_α emission taken at the Anglo Australian Telescope (Stappers et al., 2003). The image shows the formation of a bow-shock around a pulsar moving through the ISM.

$$\left(\frac{\dot{E}}{4\pi\omega R_{w0}^2} \right) \times \frac{1}{c} = \langle u \rangle = (\rho v^2)_{ram}$$

$$\therefore \frac{\dot{E}}{4\pi\omega R_{w0}^2 c} = \rho_0 V_{PSR}^2,$$

where ρ_0 is the density of the medium through which the pulsar moves and V_{PSR} is its speed. For a thin-layer shock this has been shown to occur in any direction at a distance (Wilkin, 1996)

$$R_w(\theta) = R_{w0} \csc \theta \sqrt{3(1 - \theta \cot \theta)},$$

where θ is the polar angle to the symmetry axis. Unfortunately this solution is not for a double-layer shock as is expected in PWNe. For an example of such a process see Gaensler et al. (2004).

3.2.5 Application to High Mass Binaries

The paper by Dubus (2006b) proposed that the PWN model could be applied to gamma-ray producing HMXB systems. The paper compared three HMXB systems, namely PSR B1259-63, LS 5039 and LSI +61° 303. Of these, PSR B1259-63 is a known 48 ms radio pulsar in orbit around a Be star, SS 2883, with an observed pulsar eclipse. The orbit is highly eccentric ($e \sim 0.87$, $P \sim 3.4$ year), while the disc of the Be star is at a $\sim 90^\circ$ angle with respect to the orbital plane, resulting in the pulsar passing through it twice every orbital period. LSI +61° 303

is classified as a microquasar, with an orbital period of 26.4960 ± 0.0028 days (Gregory, 2002) and has been observed from radio to gamma-ray frequencies (e.g. optical: Mendelson and Mazeh (1989); X-ray: Paredes et al. (1997) and gamma-ray: Massi (2004)).

Dubus' model proposes that a pulsar in a high mass binary system could interact with the stellar wind of its optical companion in a similar way to the interaction that occurs within a SNR or the ISM. It is assumed that the majority of the spin-down power is given to the electron/positron wind, with only a small fraction going to the toroidal magnetic field. The author proposes a scaling model for the three binary systems mentioned above based on three parameters, namely

1. R_s : The shock radius,
2. d_s : The orbital separation in the binary system, and
3. $\sigma \dot{E}$: A "combined" parameter, that uses the magnetization ratio, σ , and the spin-down luminosity, \dot{E} .

Since the pulsar is in orbit around a main sequence star, it is assumed that a bow shock will form, similar to the bow shocks seen in pulsars moving through the ISM (Figure 3.11).

The spin-down luminosity and magnetization ratio are an adapted version of those used by Kennel and Coroniti (1984a,b), and are defined as

$$\frac{\dot{E}}{4\pi R_S^2 c} = \frac{B_1^2}{4\pi} \left(\frac{1 + \sigma}{\sigma} \right)$$

and

$$\sigma = \frac{B_1^2}{4\pi n_1 \gamma_p^2 m_e c^2},$$

where γ_p is the Lorentz factor of the electron/positron wind. Similarly the shock radius, R_S , is determined by the position where the ram pressure of the stellar and pulsar winds balance, i.e.

$$\frac{\dot{E}}{4\pi R_S^2 c} = \rho_w (v_w - v_p)^2,$$

where ρ_w is the stellar wind density, v_w is the stellar wind speed and v_p is the orbital speed of the pulsar. Under the assumptions that $v_w = v_\infty$ (the wind's terminal velocity), that v_p is negligible and that $P_w \gg \dot{E}$ where $P_w = \dot{M}_w v_\infty c$ (\dot{M}_w is the mass loss rate of the optical star), the shock radius can be estimated as

$$R_S \approx \frac{d_s}{1 + (P_w/\dot{E})^{1/2}},$$

where d_s is the orbital separation. In the case of LS 5039, $\dot{M}_w \approx 10^{-7} M_\odot \text{ yr}^{-1}$, $d_s \approx 0.1 \text{ AU}$ (at

periastron) and $v_\infty \approx 2000 \text{ km s}^{-1}$, implying a shock distance from the pulsar of

$$R_s \approx 1.5 \times 10^{11} \left(\frac{d_s}{0.1 \text{ AU}} \right) \left(\frac{P_w}{10^{38} \text{ erg s}^{-1}} \right)^{-1/2} \left(\frac{\dot{E}}{10^{36} \text{ erg s}^{-1}} \right)^{1/2} \text{ cm.} \quad (3.17)$$

The estimate of the spin-down luminosity $\dot{E} \approx 10^{36} \text{ erg s}^{-1}$ is based on the assumption that the system will be similar to PSR B1259-63 where $\dot{E} = 8 \times 10^{35} \text{ erg s}^{-1}$. This shock radius, while fairly large in terms of the orbital separation of the system, still lies within the system, and is much closer than the shock fronts seen in other PWNe, e.g. $R_S \approx 3 \times 10^{17} \text{ cm}$ in the Crab Nebula.

Lorentz Factor of the Wind

It is necessary to obtain an estimate of the maximum Lorentz factor of the electrons/positrons in the pulsar wind. This will show the maximum possible emission seen from the system, allowing for the calibration of the parameters in the model. The approach used by Dubus (2006b) is to consider the maximum energy a particle can be accelerated to, by balancing the acceleration and radiation timescales of the particle. This gives an upper estimate for the maximum Lorentz factor of the particle wind. The acceleration timescale for the gyroradius is

$$t_{acc} \approx \frac{\gamma m_e c}{eB} \text{ sec,}$$

which, by substituting in the post-shock magnetic field (Kennel and Coroniti, 1984a,b),

$$\begin{aligned} B_2 &= 3(1 - 4\sigma) \left(\frac{\dot{E}}{cR_S^2} \frac{\sigma}{1 + \sigma} \right)^{1/2} \\ &\approx 5 \left[\left(\frac{\dot{E}}{10^{36} \text{ erg s}^{-1}} \right) \left(\frac{\sigma}{10^{-3}} \right) \right]^{1/2} \left(\frac{R_S}{10^{11} \text{ cm}} \right)^{-1} \text{ G,} \end{aligned} \quad (3.18)$$

gives an estimate of

$$t_{acc} \approx 0.01 \left(\frac{\gamma}{10^6} \right) \left[\left(\frac{\dot{E}}{10^{36} \text{ erg s}^{-1}} \right) \left(\frac{\sigma}{10^{-3}} \right) \right]^{1/2} \left(\frac{R_S}{10^{11} \text{ cm}} \right) \text{ sec.}$$

The synchrotron timescale is

$$\begin{aligned} t_{sync} &= \frac{9 m_e^3 c^5}{4 e^4 \gamma B^2} \\ &\approx 30 \left(\frac{\gamma}{10^6} \right)^{-1} \left[\left(\frac{\dot{E}}{10^{36} \text{ erg s}^{-1}} \right) \left(\frac{\sigma}{10^{-3}} \right) \right]^{-1} \left(\frac{R_S}{10^{11} \text{ cm}} \right)^2 \text{ sec.} \end{aligned} \quad (3.19)$$

It is possible to find the maximum Lorentz factor, γ_{max} , by requiring that $t_{acc} < t_{sync}$. Therefore

$$\begin{aligned}\gamma^2 &< \frac{9 m_e c^4}{4 e^3 B} \\ \therefore \gamma_{max} &\approx 5 \times 10^7 \left(\frac{B}{5 \text{ G}}\right)^{-1} \quad \text{or} \\ &\approx 5 \times 10^7 \left[\left(\frac{\dot{E}}{10^{36} \text{ erg s}^{-1}}\right) \left(\frac{\sigma}{10^{-3}}\right) \right]^{-1/4} \left(\frac{R_S}{10^{11} \text{ cm}}\right)^{1/2}.\end{aligned}\quad (3.20)$$

Similarly the IC scattering timescale is

$$t_T = \frac{9 m_e^3 c^5}{4 e^4 \gamma} \frac{1}{8\pi U_\star} \text{ sec}, \quad (3.21)$$

in the Thomson limit ($\gamma h\nu \ll m_e c^2$), and

$$t_{KN} \approx 5.2 \left(\frac{\gamma}{10^6}\right) \left(\frac{3\text{eV}}{kT_\star}\right)^2 \left(\frac{d_s}{R_\star}\right)^2 \left[\ln \left(\frac{4\gamma kT_\star}{m_e c^2}\right) - 1.98 \right]^{-1} \text{ sec}, \quad (3.22)$$

in the Klein-Nishina limit ($\gamma h\nu \gg m_e c^2$). Here R_\star and T_\star are the radius and temperature of the optical companion, and U_\star is the stellar photon energy density given by

$$U_\star = \frac{\sigma_B T_\star^4}{c} \left(\frac{R_\star}{d_s}\right)^2.$$

For values typical of the three high mass binary systems under consideration ($T_\star = 40000 \text{ K}$ and $R_\star = 10 R_\odot$) Equations 3.21 & 3.22 gives values of

$$t_T \approx 40 \left(\frac{\gamma}{10^3}\right)^{-1} \left(\frac{d_s}{0.1\text{AU}}\right)^2 \left(\frac{T_\star}{40000\text{K}}\right)^{-4} \left(\frac{R_\star}{10R_\odot}\right)^{-2} \text{ sec}$$

and

$$t_{KN} \approx 20 \left(\frac{\gamma}{10^6}\right) \left(\frac{d_s}{0.1\text{AU}}\right)^2 \left[\ln \left(\frac{\gamma}{10^6}\right) + 1.3 \right]^{-1} \left(\frac{T_\star}{40000\text{K}}\right)^{-2} \left(\frac{R_\star}{10R_\odot}\right)^{-2} \text{ sec}.$$

IC scattering will enter the Klein-Nishina regime when $\gamma > \frac{m_e c^2}{h\nu}$. For an average energy for the stellar photon $2.7kT_\star$, this occurs at $\gamma_{KN} \cong 6 \times 10^4$.

The question now is whether the highest Lorentz factor in the post-shock region is set by the synchrotron or IC radiation. One way to determine this is to consider which radiation process allows for the highest Lorentz factors. Using Equations 3.19 and 3.22 and solving for γ , a rough estimate shows that $t_{KN} > t_{sync}$ when

$$\gamma > \gamma_S \approx 1.2 \times 10^6 \frac{R_{11}}{d_{0.1}} \left[\left(\frac{\dot{E}}{10^{36} \text{ erg s}^{-1}}\right) \left(\frac{\sigma}{10^{-3}}\right) \right]^{1/2} \left(\frac{T_\star}{40000\text{K}}\right) \left(\frac{R_\star}{10R_\odot}\right). \quad (3.23)$$

where

$$d_{0.1} = \frac{d_s}{0.1 \text{ AU}},$$

and

$$R_{11} = \left(\frac{R_S}{10^{11} \text{ cm}} \right).$$

Since Equation 3.23 is less than Equation 3.20, this implies that the maximum Lorentz factor that can be reached is set by the synchrotron radiation (for $\gamma > 10^6$). In this regime $t_{sync} < t_{KN}$, implying that synchrotron radiation is a more effective radiation process than IC scattering at such high Lorentz factors.

Spectral Shape

The spectral shape of the emission is characterized by the three energies γ_{min} , γ_S (Equation 3.23) and γ_{max} (Equation 3.20). An estimate of γ_{min} can be made by (Dubus, 2006b; Kennel and Coroniti, 1984b)

$$\begin{aligned} \gamma_{min} \ln \left(\frac{\gamma_{max}}{\gamma_{min}} \right) &\approx \frac{\gamma_p}{\sqrt{2}} \\ \therefore \gamma_{min} &\approx 0.1 \gamma_p \quad \text{for } \gamma_{max} \gg \gamma_{min} \end{aligned}$$

where γ_p is the Lorentz factor of the pulsar wind before the shock. Substituting Equation 3.18 into Equation 3.7 gives a characteristic frequency for the synchrotron radiation (Dubus, 2006b)

$$h\nu \approx 100 \left(\frac{\gamma}{10^6} \right)_2 \left[\left(\frac{\dot{E}}{10^{36} \text{ erg s}^{-1}} \right) \left(\frac{\sigma}{10^{-3}} \right) \right]^{1/2} \left(\frac{R_S}{10^{11} \text{ cm}} \right)^{-1} \text{ keV}, \quad (3.24)$$

Substituting in the values for γ_{min} , γ_S and γ_{max} then gives

$$\begin{aligned} h\nu_{sync,min} &\approx 1 \left(\frac{\gamma}{10^6} \right)^2 \left(\dot{E}_{36} \sigma_{-3} \right)^{1/2} \left(\frac{R_S}{10^{11} \text{ cm}} \right)^{-1} \text{ keV} \\ h\nu_{sync,S} &\approx 150 \left(\dot{E}_{36} \sigma_{-3} \right)^{-1/2} \left(\frac{T_\star}{40000 \text{ K}} \right)^2 \left(\frac{R_\star}{10 R_\odot} \right)^2 \left(\frac{R_{11}}{d_{0.1}^2} \right) \text{ keV} \\ h\nu_{sync,max} &\approx 250 \text{ MeV}, \end{aligned}$$

where

$$\dot{E}_{36} \sigma_{-3} = \left(\frac{\dot{E}}{10^{36} \text{ erg s}^{-1}} \right) \left(\frac{\sigma}{10^{-3}} \right).$$

The power spectrum is a hard power law $\nu F_\nu \sim \nu^{0.7}$ for $1 \text{ keV} \lesssim \epsilon_\nu \lesssim 100 \text{ keV}$ while for the range $100 \text{ keV} \lesssim \epsilon_\nu \lesssim 250 \text{ MeV}$, $\nu F_\nu \sim \text{constant}$. For the IC radiation the frequency is given by Equation 3.14 in the Klein-Nishina regime. Substitution of γ_{min} , γ_S and γ_{max} then gives

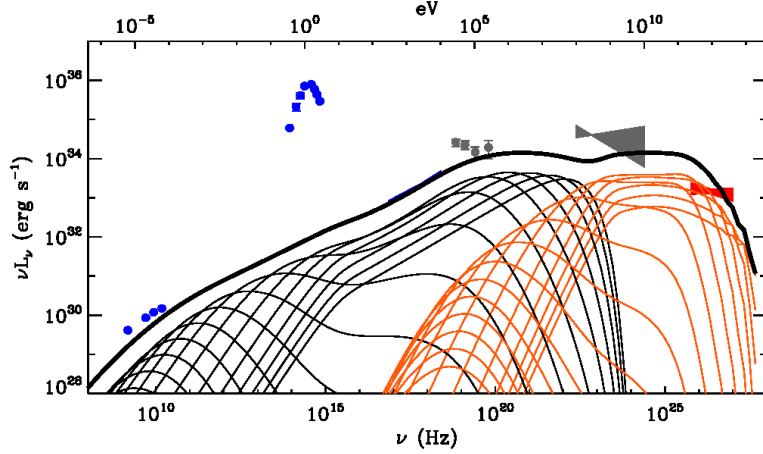


Figure 3.12: Evolution of pulsar nebula in LS 5039 (Dubus, 2006b). The black lines represent the synchrotron radiation and the orange lines the IC radiation. They are calculated for increasing values for z : $z_1 = 1$, $z_5 \approx 1.5$, $z_{10} \approx 15$ and $z_{15} \approx 1000$. The integrated spectrum is shown by the thick black line.

$$\begin{aligned}
 h\nu_{IC,min} &\approx 50 \text{ GeV} \\
 h\nu_{IC,S} &\approx 0.6 \left(\dot{E}_{36} \sigma_{-3} \right)^{-1/2} \left[\left(\frac{T_\star}{40000\text{K}} \right) \left(\frac{R_\star}{10R_\odot} \right) \right] \left(\frac{R_{11}}{d_{0.1}^2} \right) \text{ TeV} \\
 h\nu_{IC,max} &\approx 25 \left(\dot{E}_{36} \sigma_{-3} \right)^{-1/4} \left(\frac{R_S}{10^{11} \text{ cm}} \right)^{1/2} \text{ TeV}.
 \end{aligned}$$

The electron spectrum is γ^{-2} for $\nu F_\nu \lesssim \nu_{IC,S}$. For $\epsilon_\nu \gtrsim \gamma_S m_e c^2$ this spectrum steepens to γ^{-3} (Moderski et al., 2005).

Numerical Calculations

For details on the numerical calculations see Dubus (2006b). This section will present a summary of the results.

Figure 3.12 shows the numerical calculation for the evolution of the emission from the bow-shock for LS 5039, superimposed on the observational data (the example ignores orbital modulation). Using a normalized parameter $z = R/R_S$, the spectrum is shown for increasing values of z : $z_1 = 1$, $z_5 \approx 1.5$, $z_{10} \approx 15$ and $z_{15} \approx 1000$, where the subscript indicates the lines. As the pulsar follows the orbital path around the optical companion, a bow-shock forms behind it. The result is an outflowing spiral (Figure 3.13), radiating at progressively lower frequencies. Figure 3.14 shows the evolution of the radio image at 5 GHz for LS 5039, smoothed with a Gaussian kernel to mimic observational data. The author points to the similarity between the images for orbital phase 0.00 and 0.25 and the radio image by Paredes et al. (2000) (Figure 1.2).

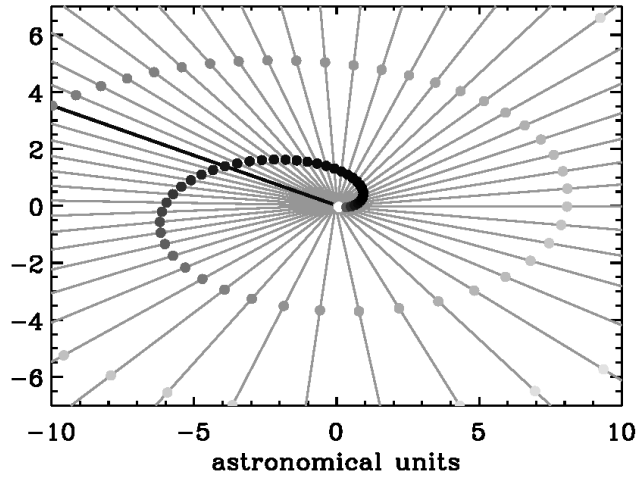


Figure 3.13: Emission from LS 5039 at periastron (Dubus, 2006b). The grey-scale is an indication of the intensity (at 5 GHz) and the lines represent equal time segments, with $i = 120^\circ$.

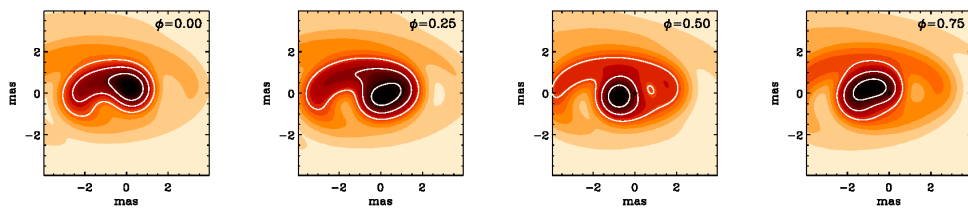


Figure 3.14: Evolution of the radio image at 5 GHz for LS 5039 (Dubus, 2006b).

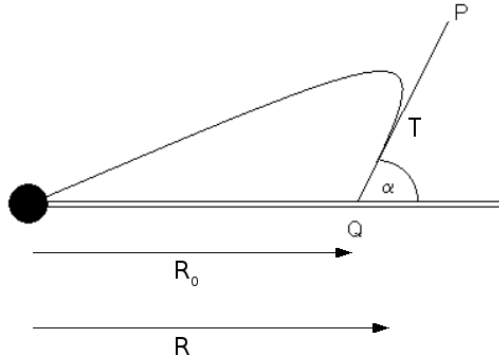


Figure 3.15: Geometry of disc outflow. The line segment PQ represents a magnetic field line anchored in the disc.

3.3 Jets and Disc Outflow

Jets have been observed in numerous systems, from quasars on the edge of the visible universe, to galactic pulsars and microquasars. A number of different mechanisms have been proposed for the creation of these jet structures, some of which will be discussed in this section.

3.3.1 Accretion Disc Mass Outflow

Jets are normally associated with discs in accretion driven systems. Presented below is a discussion of mass outflow from an accretion disc around a magnetic object (Blandford and Payne (1982); see Choudhuri (1998, pp. 312–314) for a general discussion). In this scenario the disc can also be magnetized as a result of the possible diffusion of the magnetic fields of the compact object into the disc.

If an accretion disc forms around a magnetized compact object (white dwarf or NS), the disc corona plasma is attached to the magnetic field lines and must co-rotate with the compact object. In a rotating reference frame the effective gravitational potential experienced by the particle will be

$$\Phi_{eff} = \Phi_{grav} - \frac{1}{2} (|\mathbf{\Omega} \times \mathbf{R}|^2), \quad (3.25)$$

where the second term is due to centrifugal acceleration. For a Keplerian orbit the orbital frequency will be

$$\Omega_K = \left(\frac{GM}{R_0^3} \right)^{1/2},$$

where R_0 is the radial distance from the centre of the compact object to the foot of the field line anchored in the disc (see Figure 3.15). Consider a point T , above the plane of the disc but connected to a magnetic field line that connects at R_0 . The gravitational potential at T

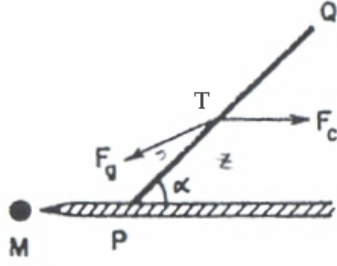


Figure 3.16: Geometry of outflow (adapted from Choudhuri (1998)).

(Figure 3.15) is given by

$$\begin{aligned}\Phi &= -\frac{GM}{r} \\ &= -\frac{GM}{(R^2 + z^2)^{1/2}},\end{aligned}$$

and the centrifugal potential by

$$\begin{aligned}\Phi(R, z) &= -\frac{1}{2}(|\boldsymbol{\Omega} \times \mathbf{R}|^2) \\ &= -\frac{1}{2}\left(\frac{GM}{R_0^3}\right)R^2,\end{aligned}$$

where R represents the radial distance, in the orbital plane, from the centre of the compact object to T (Figure 3.15). This results in an effective gravitational potential of

$$\Phi(R, z) = -\frac{GM}{R_0} \left[\frac{1}{2} \left(\frac{R}{R_0} \right)^2 + \frac{R_0}{(R^2 + z^2)^{1/2}} \right].$$

Rewriting this in terms of the difference $R' = R - R_0$ the effective potential can be approximated by

$$\Phi(R, z) = -\frac{GM}{R_0} \left[\frac{3}{2} + \frac{3}{2} \left(\frac{R'}{R_0} \right)^2 - \frac{1}{2} \left(\frac{z}{R_0} \right)^2 \right],$$

where certain higher order terms have been ignored in the approximation. Consider the geometry in Figure 3.16. The lengths R' and z can be rewritten in terms of the angle α such that

$$\begin{aligned}\cos \alpha &= \frac{R'}{s} \\ \sin \alpha &= \frac{z}{s},\end{aligned}$$



Figure 3.17: Outflow and magnetic collimation example from Matsumoto et al. (1998).

which results in

$$\Phi(s, z) = -\frac{GM}{R_0} \left[\frac{3}{2} + \frac{3}{2} \frac{s^2}{R_0^2} \cos^2 \alpha - \frac{1}{2} \frac{s^2}{R_0^2} \sin^2 \alpha \right].$$

Here s represents a line element along PQ extending from the disc along the field line. The effective gravitation along the line element s , is then

$$\begin{aligned} g_{eff} &= -\frac{d}{ds} \Phi(s, z) \\ &= \frac{GMs}{R_0^3} [3 \cos^2 \alpha - \sin^2 \alpha]. \end{aligned} \quad (3.26)$$

Here $g_{eff} < 0$ represents an effect gravity dominated by the centrifugal effect, resulting in the centrifugal expulsion of particles along the path s , away from the disc. From Equation 3.26 this will occur when

$$\begin{aligned} 3 \cos^2 \alpha - \sin^2 \alpha &< 0 \\ \Rightarrow \alpha &< 60^\circ. \end{aligned}$$

This implies that for field lines crossing the accretion disc at angles $\alpha < 60^\circ$ material will experience an effective acceleration that will drive the material away from the disc. This will continue until the material crosses the Alfvén radius, at which point the kinetic energy will dominate over the magnetic energy. After the Alfvén radius the material can orbit at frequencies less than Ω_K , which will cause the magnetic field lines to twist around the rotation axis. This can result in the collimation of the outflow material, creating jet outflows (Figure 3.17).

3.3.2 Blandford-Znajek Model

The Blandford-Znajek model (Blandford and Znajek, 1977) provides a way to extract rotational energy from a Kerr BH. This discussion will follow Frank, King, and Raine (1992, pp. 236–242).

Consider a magnetized accretion disc that has formed around a compact object, and that the magnetic field lines are frozen into the disc. The magnetic energy must not be so large that it disrupts disc formation. If the system is considered in a cylindrical coordinate system, then it is possible to break the magnetic and electric field lines into their toroidal ($\hat{\mathbf{e}}_\phi$) and poloidal ($\hat{\mathbf{e}}_r, \hat{\mathbf{e}}_z$) components. The result is

$$\mathbf{B} = \mathbf{B}_T + \mathbf{B}_P = (0, B_\phi \hat{\mathbf{e}}_\phi, 0) + (B_z \hat{\mathbf{e}}_z, 0, B_r \hat{\mathbf{e}}_r)$$

and similarly for \mathbf{E}

$$\mathbf{E} = \mathbf{E}_T + \mathbf{E}_P.$$

This section will search for a stationary and axisymmetric solution. Since the solution is independent of time, the *emf* due to magnetic flux, Φ , through a circle around the rotation axis is (Faraday's law of induction)

$$\begin{aligned} emf &= \oint \mathbf{E}_T \cdot d\mathbf{l} = -\frac{d\Phi}{dt} \\ &= -\frac{1}{c} \int_s \frac{dB}{dt} \cdot \mathbf{n} da \\ &= 0, \end{aligned}$$

since $\frac{dB}{dt} = 0$. Therefore

$$\begin{aligned} \mathbf{E}_T &= 0 && \text{and} \\ \mathbf{E} &= \mathbf{E}_P. \end{aligned}$$

Since the solution is axisymmetric

$$\nabla \cdot \mathbf{B}_T = \frac{dB_\phi}{d\phi} \hat{\mathbf{e}}_\phi = 0,$$

and to satisfy the condition that $\nabla \cdot \mathbf{B} = 0$, i.e.

$$\begin{aligned} \nabla \cdot \mathbf{B}_P &= \nabla \cdot \mathbf{B} - \nabla \cdot \mathbf{B}_T \\ &= 0. \end{aligned}$$

This implies that the field lines can be thought of being separately connected with the toroidal or poloidal fields, both satisfying $\nabla \cdot B = 0$. If Ferraro's law of isorotation is considered under the condition that $\mathbf{E} \cdot \mathbf{B} = 0$ (force-free), it is required that that the force on a charged particle

in a co-rotating reference frame, K' is zero, i.e,

$$\begin{aligned}\mathbf{F}' = 0 &= q(\mathbf{E}' + \frac{1}{c}\mathbf{v}' \times \mathbf{B}') \\ &= q\mathbf{E}' \quad \text{since } \mathbf{v}' = 0 \text{ in } K' \\ \Rightarrow \mathbf{E}' &= 0.\end{aligned}$$

Transforming \mathbf{E}' to a non-rotating reference frame gives

$$\begin{aligned}\mathbf{E}' &= \gamma(\mathbf{E} + \frac{1}{c}(\mathbf{v} \times \mathbf{B})) \\ &\approx (\mathbf{E} + \frac{1}{c}\mathbf{v} \times \mathbf{B}) \quad \text{for } \gamma \approx 1 \\ \Rightarrow \mathbf{E}_{\mathbf{P}} &= -\frac{1}{c}((\boldsymbol{\Omega} \times \mathbf{r}) \times \mathbf{B})\end{aligned}\tag{3.27}$$

since $\mathbf{E} = \mathbf{E}_{\mathbf{P}}$ and $\mathbf{v}_{\phi} \times \mathbf{B}_{\mathbf{T}} = 0$ (here $\boldsymbol{\Omega} = (0, 0, \Omega_F)$). Since $\nabla \times \mathbf{E}_{\mathbf{P}} = 0$, taking the curl of Equation 3.27 gives

$$\begin{aligned}\nabla \times \mathbf{E}_{\mathbf{P}} &= \nabla \times \left[-\frac{1}{c}((\boldsymbol{\Omega} \times \mathbf{r}) \times \mathbf{B}) \right] \\ \therefore \nabla \times [((\boldsymbol{\Omega} \times \mathbf{r}) \times \mathbf{B})] &= 0.\end{aligned}\tag{3.28}$$

From Equation 3.28, it is then possible to show that

$$\mathbf{B}_{\mathbf{P}} \cdot \nabla \Omega_F = 0,$$

which implies that there is no change in Ω_F along poloidal field lines, i.e. Ω_F is constant and so there is no twisting of magnetic field lines. This condition is known as *Ferraro's law of isorotation* (e.g. Choudhuri (1998, p. 308)). At some point along the field line the velocity will approach the speed of light. The surface where this occurs is known as the *speed of light surface*.

The electric field within the accretion disc results in the formation of a charge density within the disc, which in turn gives rise to an electric field beyond the disc. This electric field can then accelerate charged particles. The resulting charge density is

$$\begin{aligned}\rho &= \frac{1}{4\pi \nabla \cdot \mathbf{E}} \\ &= -\left[\frac{\boldsymbol{\Omega} \cdot \mathbf{B}}{2\pi c} \right].\end{aligned}$$

In a sufficiently high magnetic field, the force on the charged particles will exceed that of gravity and particles will be removed from the disc surface. The condition of degeneracy ($\mathbf{E} \cdot \mathbf{B} = 0$) will still hold to a reasonable approximation if the condition $R\boldsymbol{\Omega} \ll c$ applies.

The result of this model is a force-free region above the disc (the disc is non-force-free), which extends until close to the *speed of light surface*, where special relativistic effects create a non-force-free region due to the high relativistic mass as $v \rightarrow c$ (Figure 3.18).

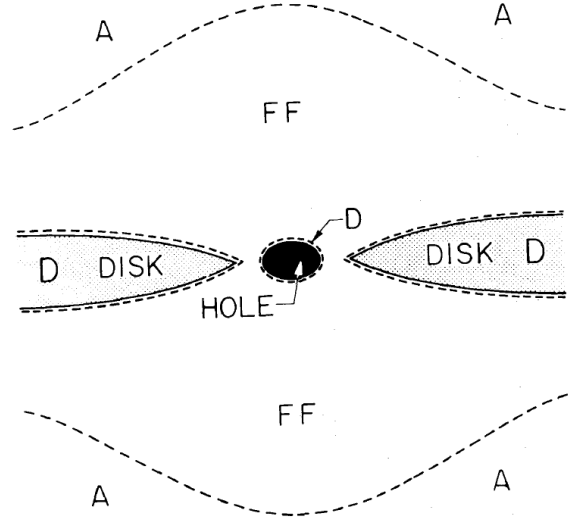


Figure 3.18: Force-free region (FF) around the disc structure (MacDonald and Thorne, 1982).

In the Blandford-Znajek model the disc is formed around a Kerr BH. The effects of GR only become important close to the inner edge of the disc near $R \sim 3R_{Schw}$ and as a result the luminosity can be considered in terms of Newtonian gravity. The magnetic lines are frozen into the disc and accrete across the event horizon, resulting in the magnetic field connecting the rotating BH with the disc. Differential rotation between the BH and the disc results in a torque exerted on the disc, which extracts rotational kinetic energy from the BH.

If poloidal magnetic field line is rotated around the z axis (the axis of symmetry), the result is a surface of constant Ω , known as *magnetic surfaces* (Figure 3.19). The magnetic flux at a point (r, z) , is found by integrating the magnetic field over an area defined by a circle with radius r , aligned around the z -axis,

$$\begin{aligned}\Phi(r, z) &= \int_0^r \mathbf{B} \cdot d\mathbf{a} \\ &= \int_0^r 2\pi R B(z) dR.\end{aligned}$$

This flux Φ is constant over the magnetic surfaces since $\nabla \cdot \mathbf{B} = 0$. In order to create an energy flux above the disc it is necessary to have a non-zero toroidal magnetic field, implying the existence of a current I , driven along the magnetic surfaces. From Ampere's law

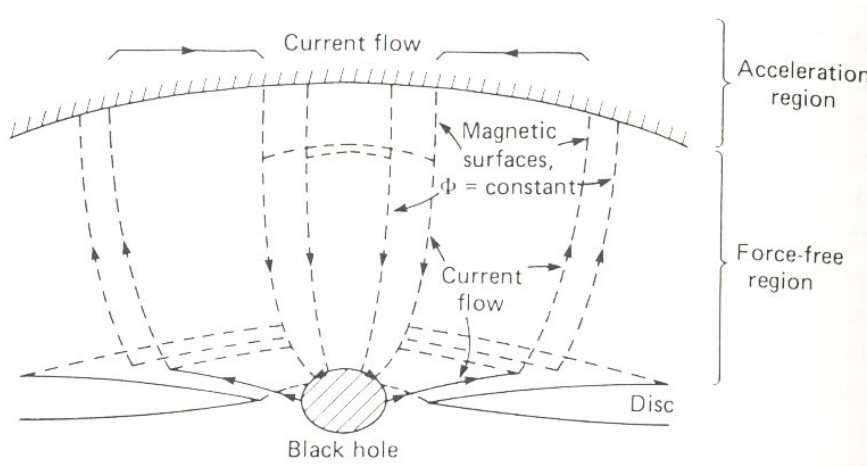


Figure 3.19: Magnetic surfaces and current flow in Blandford-Znajek model (Frank et al., 1992).

$$\oint \mathbf{B}_T \cdot d\mathbf{l} = \frac{4\pi}{c} I$$

$$B_T 2\pi R = \frac{4\pi}{c} I$$

$$B_T = \frac{2I}{cR},$$

which gives the magnetic field induced by the current I . If two magnetic surfaces at R and $R + dR$, with a current $I(R)$ and $I(R + dR)$ are considered, it is clear that a current must flow between them or else a charge will build up (see Figure 3.19 for the current flow). The Poynting flux through the force-free region is then

$$\mathbf{S} = \frac{c}{4\pi} (\mathbf{E} \times \mathbf{B})$$

$$= \frac{c}{4\pi} (\mathbf{E}_T \times \mathbf{B}_T).$$

An order of magnitude approximation for the flux can be made from Equation 3.27 such that

$$S \sim \frac{R\Omega B_P B_T}{4\pi}. \quad (3.29)$$

To get a very rough estimate of $B_P B_T$ it can be considered in terms of the velocities of the particles. Close to the acceleration region (upper non-force-free region) the particles velocity approaches c . Since these particles must flow along the magnetic field line, $\mathbf{B} = \mathbf{B}_T + \mathbf{B}_P$, and the resulting diagram of velocities and magnetic field is shown in Figure 3.20. The result is (order

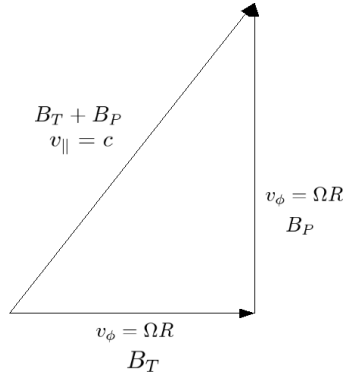


Figure 3.20: Diagram of the velocities and magnetic fields above the disc.

of magnitude estimation)

$$\begin{aligned} \frac{B_P}{B_T} &\sim \frac{(c^2 - R^2\Omega^2)^{1/2}}{R\Omega} \\ &\sim \frac{c}{R\Omega}. \end{aligned}$$

Substituting this ratio into Equation 3.29 gives

$$L \approx \frac{1}{4\pi} \int B_P^2 c \left(\frac{R\Omega}{c} \right)^2 2\pi R dR. \quad (3.30)$$

Since the maximum contribution should come from close to the last stable orbit at $R \sim 3R_{Schw}$, Equation 3.30 can be simplified for a Keplerian orbit (Equation 2.18) and $R = 3R_{Schw}$ (Equation 2.47) as

$$\begin{aligned} L &\approx \frac{B_P}{2c} \int R^3 \left(\frac{GM}{R^3} \right) dR \\ &\approx \frac{GB_P^2 MR}{2c} \\ &\approx \frac{3G^2 B_P^2 M^2}{c^3}. \end{aligned}$$

For values of active galactic nuclei the luminosity can become very high,

$$L \approx 10^{45} \left(\frac{B_P}{10^4 \text{ G}} \right)^2 \left(\frac{M_{BH}}{10^8 M_\odot} \right)^2 \text{ erg s}^{-1}.$$

This luminosity is the result of the electrodynamic coupling between the disc and the rotating BH, extracting rotational kinetic energy from the BH. Although this analysis is very simplistic, it provides some insight in terms of the enormous VHE emission potential of these systems.

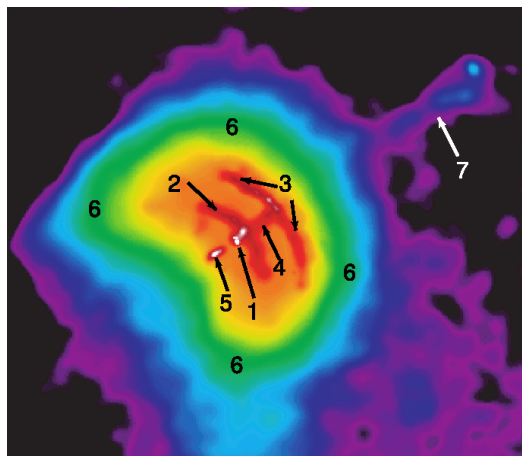


Figure 3.21: Chandra image of the Vela pulsar, showing the pulsar wind shock front, and the torus and jet. The labels show: 1. The Vela pulsar, 2. Inner arc, 3. Outer arc, 4. Inner jet, 5. Counter jet, 6. The shell, 7. The outer jet. Pavlov et al. (2003).

3.3.3 Jets in PWNe

Observations of numerous pulsar systems have revealed the existence of a torus-jet structure surrounding them (Figures 3.6, 3.21 & 3.22). The jets appear to originate from the pulsar while the pulsar is surrounded by a torus shaped structure. The challenge is then to connect these structures with the PWN model. The likely scenario is that these “jets” are not jet structures similar to those found in quasars and microquasars, where particles are accelerated to relativistic velocities from an accretion disc, but are instead regions of collimated mass outflow. This will occur outside of the shock radius where the pulsar wind has been decelerated and magnetic collimation can occur (e.g. Lyubarsky (2002)). The jet and torus are explained by assuming that the Lorentz factor of the pulsar wind has the form (e.g. Bogovalov and Khangoulyan (2002); Bogovalov et al. (2005))

$$\gamma = \gamma_0 + \gamma_m \sin^2 \theta,$$

where $\gamma_0 \approx 200$, is the Lorentz factor near the light cylinder and

$$\begin{aligned} \gamma_m &= \left(\frac{\Omega R_0}{v} \right)^2 \left[\frac{B_{p0}^2}{4\pi n_0 m c^2 \gamma_0} \right] \\ &\approx 10^6 - 10^7. \end{aligned}$$

Here B_{p0} ^{||} is the poloidal magnetic field and θ is the angle relative to the z-axis. The Lorentz factor is modelled in this way because it requires a value greater than 200 in order to be unaffected by magnetic collimation, while the second term, $\gamma_m \sin^2 \theta$, is the result of electromagnetic energy flux conservation. For a detailed discussion see Bogovalov and Khangoulyan (2002). The result

^{||}The subscript 0 indicates that the value is near the light cylinder.

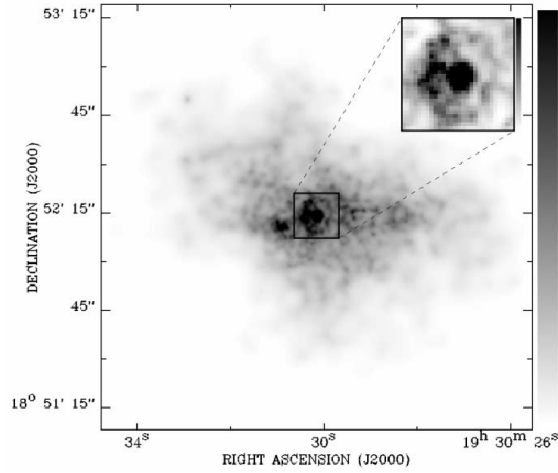


Figure 3.22: *Chandra* image of SNR G54.1+0.3 (Lu et al., 2002).

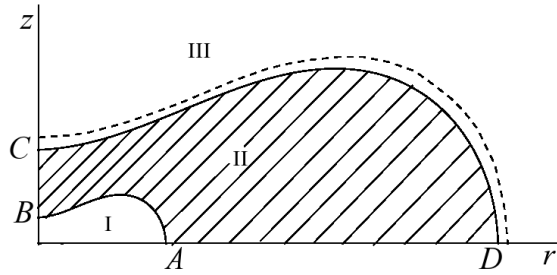


Figure 3.23: Schematic of the PWN shock (Bogovalov et al., 2005).

is that γ is dependent on $\sin^2 \theta$ and the result is a shock front of the form shown in Figure 3.23. This shows that the shock front occurs a lot closer to the pulsar along the z axis. As a result the non-relativistic wind can be collimated much closer to the pulsar, given the impression that it is a “jet” emanating from the pulsar.

A number of numerical simulations have been applied to this phenomena. Figures 3.24 & 3.25 show two examples by Bogovalov et al. (2005) & Komissarov and Lyubarsky (2004) respectively. These simulations show that for a sufficiently low value of the magnetization ratio, σ , “jet” formation in PWNe is a natural consequence.

The evolution of the jets is far from simple as observations of the Vela pulsar have shown (Figure 3.26).

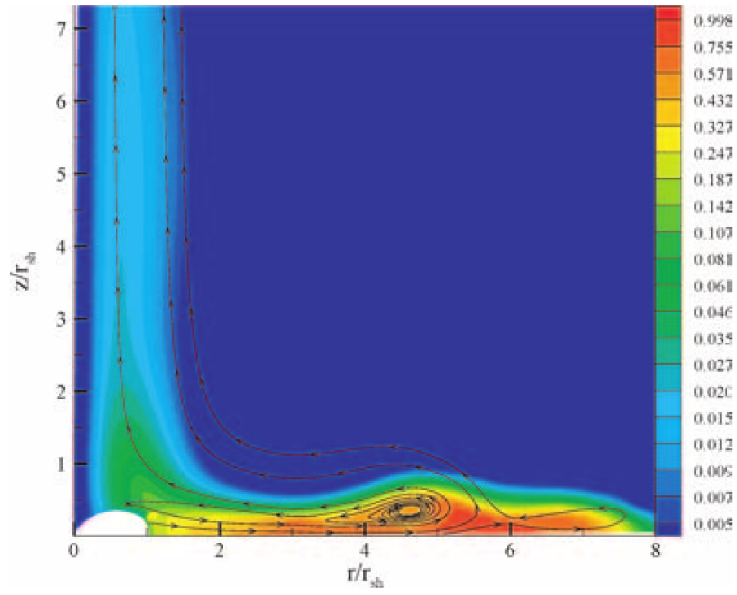


Figure 3.24: Prediction of the volume synchrotron emissivity for a Crab-like PWN (Bogovalov et al., 2005). The emissivity is in arbitrary units and scaled logarithmically.

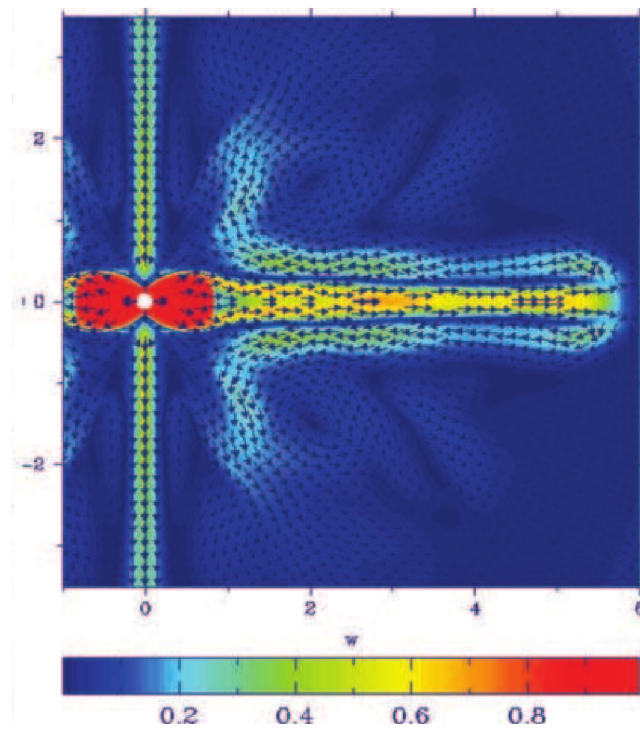


Figure 3.25: Numerical model of the velocity of the outflow in a PWN (Komissarov and Lyubarsky, 2004).

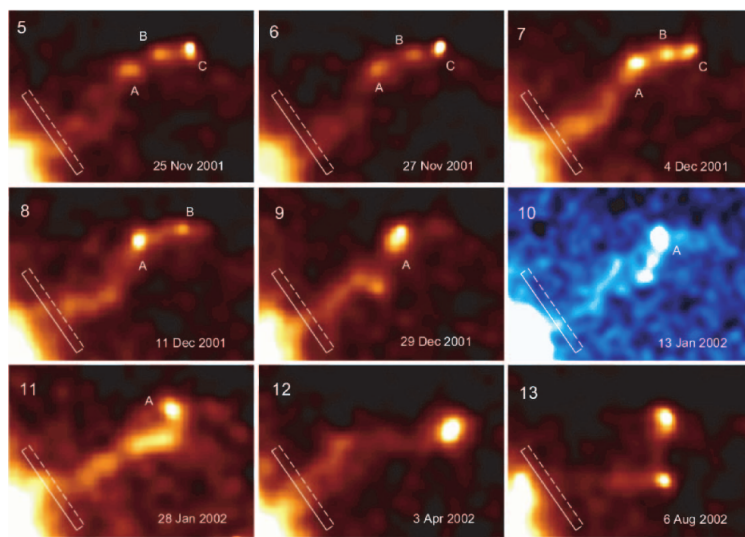


Figure 3.26: Chandra images of the variability of the jet in the Vela pulsar (Pavlov et al., 2003).

Chapter 4

A Model Independent Approach towards Solving the Mysteries of LS 5039

Two models have been proposed to explain the emission from LS 5039. The first is the standard accretion driven microquasar model where relativistic jets are responsible for the synchrotron and IC radiation emitted from the system. The second is the PWN model, applied to HMXBs, where the compact object is a young pulsar that creates a highly relativistic electron/positron wind which interacts with the stellar wind of the optical companion. This interaction results in a shock front of expanding synchrotron and IC emitting material. Both these models present their own advantages and disadvantages. For example the radio jet structures support the microquasar model and suggest an accretion driven scenario. However, the luminosity is very high given the low accretion rate, which implies a very high conversion efficiency (see next section). In addition, the low X-ray luminosity is unusual given the VHE gamma-ray emission. Adapting a pulsar wind model provides an additional energy reservoir (spin-down and magnetic field of the pulsar) as well as providing a relativistic wind. It is however more difficult to reconcile the radio jets with the PWN model. This could be solved by either an elongation the shocked outflow along the semi-major axis or through collimation of the outflow as is seen in isolated pulsars. In addition the absence of a pulsed signal does not allow for a direct measurement of the spin-down power of the pulsar. In this chapter a model independent approach (neither a microquasar nor pulsar wind model) will be taken to determine what conclusions can be drawn about the nature of the compact object.

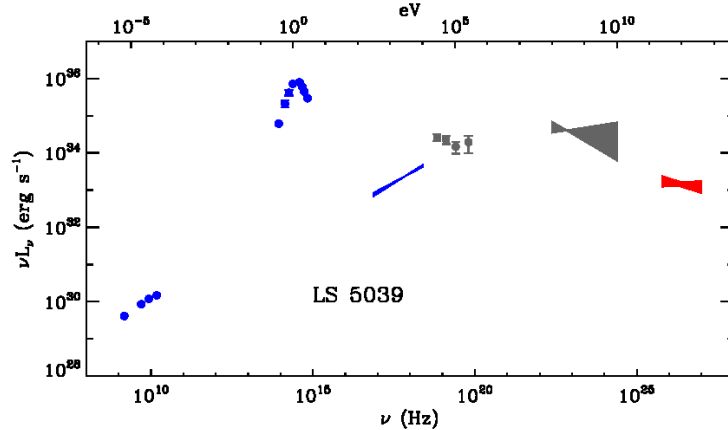


Figure 4.1: Composite of the broad-band observations of LS 5039 (Dubus, 2006b) (Radio: Martí et al. (1998); Optical: Clark et al. (2001); Soft X-ray: Martocchia et al. (2005); Hard X-ray: Harmon et al. (2004); EGRET gamma-rays: Hartman et al. (1999); H.E.S.S. gamma-rays: Aharonian et al. (2006)). With the exception of the optical black-body peak associated with the O-type giant, the broad emission appears to be of a non-thermal nature.

4.1 The Broad Band Spectrum

The broad band spectrum of LS 5039 is shown in Figure 4.1 and is a composite of the observations at different wavelengths from radio up to VHE gamma-rays. This shows broad-band, non-thermal synchrotron and possibly IC emission from the system, with the exception of the optical black body peak of the O-type giant. This suggests that any model proposed for LS 5039 must model the broad non-thermal multi-wavelength emission in terms of synchrotron and possible IC emission. The possibility of the gamma-ray emission above 1 TeV being of IC origin is not excluded as the spectrum above 1 TeV is compatible with both above mentioned radiation mechanisms. The recent detection of VHE gamma-rays shows the enormous amount of power the system is capable of, producing photons with energies $\sim 3 \times 10^{13}$ eV (Aharonian et al., 2006). To produce a photon with this energy through IC scattering would require an electron with a Lorentz factor (Equation 3.13)

$$\begin{aligned} \gamma &= \frac{\epsilon_{\text{photon}}}{m_e c^2} \\ &\gtrsim 6 \times 10^7. \end{aligned}$$

The VHE gamma-ray emission from LS 5039 confirms that a very effective particle acceleration mechanism is operating in the system, which is supported by the estimation above. Since the total bolometric luminosity of the optical star suggests a compact object accreting from the stellar wind of a blue giant under-filling its Roche lobe, the significant VHE gamma-ray emission implies a very efficient conversion of accretion power to non-thermal emission. In Section 4.2.2

it will be shown that the accretion rate onto the compact object is roughly $\dot{M}_w \sim 3 \times 10^{14} \text{ g s}^{-1}$. An approximation of the accretion luminosity for a BH ($M \gtrsim 3 M_\odot$, $R_{Schw} \sim 9 \text{ km}$) and a NS ($M_{NS} \gtrsim 1.4 M_\odot$, $R_{NS} \sim 10 \text{ km}$) is then

$$L_{BH} \approx 1 \times 10^{35} \left(\frac{M}{3 M_\odot} \right) \left(\frac{\dot{M}}{3 \times 10^{14} \text{ g s}^{-1}} \right) \left(\frac{R}{9 \text{ km}} \right)^{-1} \text{ erg s}^{-1}$$

and

$$L_{NS} \approx 6 \times 10^{34} \left(\frac{M}{1.4 M_\odot} \right) \left(\frac{\dot{M}}{3 \times 10^{14} \text{ g s}^{-1}} \right) \left(\frac{R}{10 \text{ km}} \right)^{-1} \text{ erg s}^{-1}$$

for a BH and NS respectively. From Figure 4.1, a rough order of magnitude estimate for the energy conversion is

$$\alpha_{BH} = \frac{L_\gamma}{L_{BH}} \leq 0.20 \left(\frac{L_\gamma}{2 \times 10^{34} \text{ erg s}^{-1}} \right) \left(\frac{L_{BH}}{1 \times 10^{35} \text{ erg s}^{-1}} \right)^{-1}$$

and

$$\alpha_{NS} = \frac{L_\gamma}{L_{NS}} \leq 0.33 \left(\frac{L_\gamma}{2 \times 10^{34} \text{ erg s}^{-1}} \right) \left(\frac{L_{NS}}{6 \times 10^{34} \text{ erg s}^{-1}} \right)^{-1}.$$

This simple estimate demonstrates the high conversion efficiency that is required.

This chapter will attempt not only to propose a mechanism to explain the broad non-thermal emission, but will also consider mechanisms to explain the jet-like radio structures. The discussion is presented as follows: In the following section (Section 4.2) a qualitative evaluation of the most relevant system parameters, which are related to the modelling, will be presented, e.g. binary separation and the accretion rate onto the unknown compact object. Following the basic philosophy adopted in this study, the properties are evaluated in a model independent fashion, i.e. considering only basic physical principles. In Section 4.3 the possibility of a thermal driven jet mechanism is investigated. The purpose of this is to evaluate the possibility of LS 5039 being a microquasar containing a roughly solar mass BH which is surrounded by an accretion disc or ring. In Section 4.4 this is followed-up by a discussion related to the evaluation of the system in the case of the compact object being a magnetized NS.

4.2 System Parameters

In order to understand and model the dynamics of the emission from LS 5039, it is first necessary to know the orbital and system parameters. Not only does this determine the nature and rate of accretion, but it also places constraints on the particle acceleration and the non-thermal emission in such a system. This section will investigate how different values for the mass of the compact object will adjust the orbital system properties and how this will affect the wind accretion rate onto the compact object. These values are independent of a particular model, since the orbital parameters are only dependent on the masses of the two objects, while the wind accretion rate is

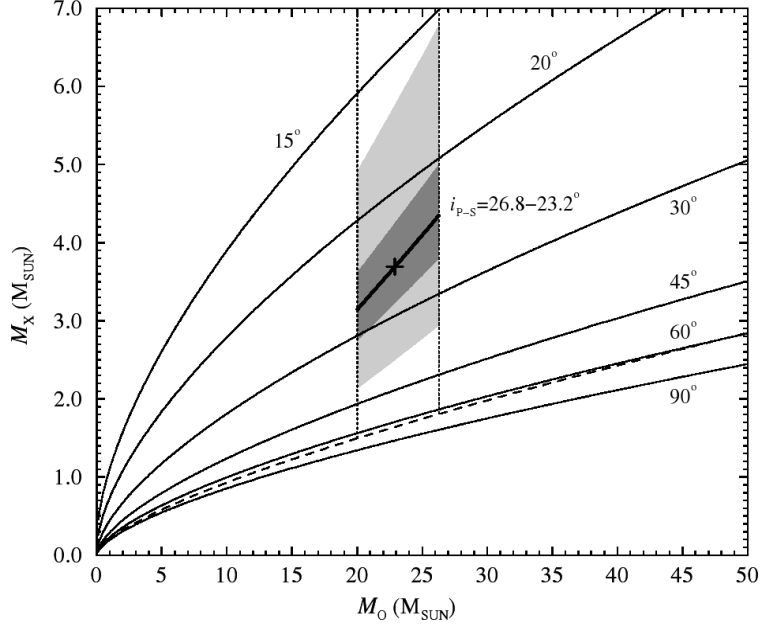


Figure 4.2: An analysis of the mass constraints on the compact object in LS 5039 by Casares et al. (2005). The curved lines represent angles of inclination as indicated, while the dashed line is the maximum angle as constrained by the lack of an eclipse in the system. The vertical dotted lines are the mass constraints of the optical companion, $M_O = 22.9^{+3.4}_{-2.9} M_\odot$. The cross in the centre of the image is the value proposed by the author for $i = 24.9$ and $M_X = 3.7 M_\odot$.

dependent on the mass of the compact object. The two exceptions to the second condition are a compact object possessing a magnetic field with a strength great enough to affect the stellar wind beyond the wind accretion radius, and if the central object is a young, wind-producing pulsar where the pulsar wind would prevent or inhibit accretion. The accretion rate will be discussed here since it will be applied to the majority of the modelling that follows.

4.2.1 Binary Separation and Velocity

A value of $3.7 M_\odot$ has been proposed for the mass of the compact object in LS 5039 by Casares et al. (2005); this however is not a definitive value. Figure 4.2 shows the analysis of the compact object mass performed by these authors. It shows that the absence of an X-ray eclipse constrains the inclination angle to $i < 64.6$, implying a minimum value of $M_X = 1.49 \pm 0.11 M_\odot$. The authors imply a limit by assuming that the system is pseudo-synchronized and in this way limit the inclination angle to $23.2 < i < 26.8$. If this assumption is correct, the best fit for the mass of the compact object is $3.7^{+1.3}_{-1.0} M_\odot$, which places the compact object in the BH mass range and the system is correctly defined as a microquasar. There is however no evidence to prove that pseudo-synchronization has occurred, and as such the possibility of a NS compact object remains open.

Table 4.1: Orbital parameters of LS 5039 for various mass values of M_X .

Mass(M_\odot)	a (cm)	α (cm)	β (cm)	v_α (cm s $^{-1}$)	v_β (cm s $^{-1}$)
1.4	2.10E+12	1.37E+12	2.84E+12	5.64E+07	2.72E+07
1.8	2.12E+12	1.37E+12	2.86E+12	5.68E+07	2.73E+07
2.2	2.13E+12	1.38E+12	2.87E+12	5.71E+07	2.75E+07
2.6	2.14E+12	1.39E+12	2.89E+12	5.74E+07	2.76E+07
3.0	2.15E+12	1.40E+12	2.90E+12	5.77E+07	2.78E+07
3.7	2.17E+12	1.41E+12	2.93E+12	5.82E+07	2.80E+07

By accepting the mass of the optical donor star, $M_\star = 22.9 M_\odot$, eccentricity, $e = 0.35$ and orbital period, $P_{orb} = 3.90603$ days, as derived by Casares et al. (2005), the orbital parameters can be examined for various values of the compact object. The semi-major axis is determined by rewriting Equation 2.5 as

$$a = \left[\frac{1}{4\pi^2} G(M_\star + M_X) P^2 \right]^{1/3},$$

where M_X is the mass of the compact star. The distances to periastron, α , and apastron, β , are determined from Equations 2.3 & 2.4 respectively, and the relative velocity at these points, v_α and v_β , by Equations 2.6 & 2.7. The results for the various values of M_X are given in Table 4.1.

Since the binary system is dominated by the mass of the optical companion, the orbital parameters do not vary significantly for the mass range $1.4 M_\odot \leq M_X \leq 3.7 M_\odot$. The result is a semi-major axis, $a \approx 2 \times 10^{12}$ cm, and a velocity at periastron of $v_\alpha \approx 5.7 \times 10^7$ cm s $^{-1}$.

By applying a mass ratio, $q = \frac{22.9 M_\odot}{1.8 M_\odot} = 12.72$, to the Eggleton approximation of the Roche lobe radius (Equation 2.10), a distance of,

$$R_{L_1} \approx 1.3 \times 10^{12} \text{ cm},$$

is obtained. This is much larger than the stellar radius (Casares et al., 2005)

$$\begin{aligned} R_\star &= 9.3 R_\odot \\ &\approx 6.5 \times 10^{11} \text{ cm}, \end{aligned}$$

confirming that the optical companion is probably under-filling its Roche lobe. This suggests that the compact object accretes from the stellar wind.

4.2.2 Wind Accretion Ratio

Optical observations of the O-type star in the LS 5039 system allow for estimations of the mass loss rate from the donor star due to the stellar wind. Since the optical giant is a non-Roche lobe

Table 4.2: Wind accretion ratios for estimate $v_w \approx v_\infty$, using Equation 4.1.

M (M_\odot)	$\dot{M}/(-\dot{M}_w)$	
	<i>periastron</i>	<i>apastron</i>
1.4	4.94E-006	1.18E-006
1.8	8.07E-006	1.93E-006
2.2	1.19E-005	2.85E-006
2.6	1.65E-005	3.93E-006
3.0	2.17E-005	5.18E-006
3.7	3.25E-005	7.75E-006

filling system, any accretion must occur via the capturing of the stellar wind by the compact object. The variation of the accretion rate over the orbit will have a significant influence on the modulation of the luminosity. It is therefore necessary to determine the proportion of the stellar wind material that is captured by the compact object. In order to simplify this process, only the values at periastron and apastron will be calculated.

Ratios

The ratio of captured material to wind outflow (Equation 2.17) determined in Section 2.2.2 is not truly applicable to LS 5039 since the condition $v_w \gg v_n$ does not hold true.

The more accurate version of the ratio equation is given by (Davidson and Ostriker, 1973)

$$\frac{\dot{M}}{\zeta \dot{M}_{wind}} = \left(\frac{M_{NS}}{M_\star} \right)^2 \frac{\epsilon^2}{\mu^{1/2}(\mu + \epsilon)^{3/2}}, \quad (4.1)$$

where

$$\mu = \frac{d}{R_\star}$$

and

$$\epsilon = \frac{v_{esc}^2}{2v_w^2(d)}.$$

The variable ζ is a scaling factor to account for the effect of the Eddington limit and is of the order of unity. The results for the wind capture ratio, using Equation 4.1, are shown in Table 4.2. These values show that the rate of accretion should increase by a multiple of 2–4 between apastron and periastron. The modelling presented in this chapter will be based on the accretion rates suggested by Table 4.2.

Captured Material

The amount of captured material is determined by the fraction of the stellar wind that enters the wind accretion radius. An estimate of the inflow material can then be made by

$$\dot{M} = \left(\frac{\dot{M}}{\zeta \dot{M}_{wind}} \right)_{cal} \times (\dot{M}_{wind})_{obs},$$

where the sub-script *cal* refers to the ratio calculated and the term sub-scripted *obs* refers to estimations made by observations. Estimates of the wind mass outflow from the optical companion (Casares et al., 2005), give a range of outflow values, with best fit values of $3.7 \times 10^{-7} M_{\odot} \text{ yr}^{-1}$ and $7.5 \times 10^{-7} M_{\odot} \text{ yr}^{-1}$ for periods of low and high outflow respectively (see page 12). An average value,

$$\begin{aligned} |\dot{M}_{wind}| &= \frac{3.7 + 7.5}{2} \times 10^{-7} \\ &= 5.6 \times 10^{-7} M_{\odot} \text{ years}^{-1} \\ &= 3.5 \times 10^{19} \text{ g s}^{-1} \end{aligned}$$

is then adopted to estimate the position of the Alfvén radius. Since $\dot{M} \leq 10^{-5} \dot{M}_{wind}$ (Table 4.2) it implies a typical accretion rate $\dot{M} \leq 3 \times 10^{14} \text{ g s}^{-1}$.

The fact that the compact object residing in LS 5039 most probably accretes from the wind of its companion has far reaching consequences regarding the nature of the system, i.e. microquasar or pulsar wind driven system, as well as the mechanism driving the particle acceleration and emission to TeV energies. The previous classification of LS 5039 was to some extent influenced by the jet-like outflow, which in the context of a microquasar scenario most probably originates from an accretion disc. Since there is no Roche lobe overflow in LS 5039, it is difficult to determine whether there is sufficient angular momentum to form and accretion disc around the compact object. If it is assumed that a fraction of the accreting material processes sufficient angular momentum to settle into a ring-like structure orbiting the compact object, a model independent estimation of the requirements for a thermal-driven disc outflow can be made for a few M_{\odot} mass BH microquasar.

4.3 A Thermal Driven Jet Outflow in LS 5039?

Since LS 5039 shows an outflow of material in the form of radio jets it is necessary to consider mechanisms whereby this can occur, a few of which have already been discussed in previous chapters. For example it has been shown that centrifugally driven outflows can originate from a magnetosphere-disc interaction (see Section 3.3.1). If however the compact object is an accreting BH, as has been suggested for LS 5039, the presence of an induced magnetosphere connecting the BH and disc (e.g. the Blandford-Znajek model), is based upon assumptions and such models

are not quantifiable. Hence it is assumed any disc outflow will probably be of thermal origin.

In order to investigate this, an estimate will be made of the small fraction of the material within a disc or ring which possesses a velocity on the outer tail-end of the Maxwell-Boltzmann distribution. In this region, a small fraction of particles possess a velocity exceeding the required escape velocity. This will be a rough order of magnitude approximation, but should be sufficient to draw a conclusion on whether a thermally driven outflow is possible in the system. Since any disc or ring will orbit at a distance $R > 3R_{Schw}$, where R_{Schw} is the Schwarzschild radius, general relativistic considerations need not be considered.

4.3.1 Fraction of Particles

In order to determine the fraction of particles within a system that possess a thermal velocity greater than the escape velocity, the particles will be considered in terms of the Maxwell-Boltzmann distribution function,

$$f(\mathbf{p}) = \frac{dn}{d^3p} = n \left(\frac{1}{2\pi mkT} \right)^{3/2} e^{-\frac{p^2}{2mkT}} \quad [(\text{cm}^{-3})(\text{g cm s}^{-1})].$$

This can then be re-written in the form

$$\begin{aligned} \frac{dn}{n} &= \left(\frac{1}{2\pi mkT} \right)^{3/2} e^{-\frac{p^2}{2mkT}} d^3p \\ &= 4\pi p^2 \left(\frac{1}{2\pi mkT} \right)^{3/2} e^{-\frac{p^2}{2mkT}} dp. \end{aligned}$$

The particles that possess a momentum exceeding the required escape momentum, $p_{esc} = mv_{esc}$, can be estimated from the above equation by integrating over the region in momentum space, $p = p_{esc} \rightarrow \infty$, i.e.

$$\begin{aligned} frac &= \int_{p_{esc}}^{\infty} \frac{dn}{n} \\ &= 4\pi \left(\frac{1}{2\pi mkT} \right)^{3/2} \int_{p_{esc}}^{\infty} p^2 e^{-\frac{p^2}{2mkT}} dp. \end{aligned} \quad (4.2)$$

The term *frac* is the fraction of particles that can escape due to thermal evaporation. In order to write the equation only in terms of momentum, the *most probable momentum* is defined as

$$p_0 \equiv mv_0 = \sqrt{2mkT},$$

where

$$v_0 = \sqrt{\frac{2kT}{m}},$$

is the most *probable velocity* of a particle in a thermal medium with temperature T . Equation 4.2 is then re-written as

$$\begin{aligned}
frac &= \frac{4}{\sqrt{\pi}} \left(\frac{1}{p_0} \right)^3 \int_{p_{esc}}^{\infty} p^2 e^{-\frac{p^2}{p_0^2}} dp \\
&= \frac{4}{\sqrt{\pi}} \int_{p_{esc}}^{\infty} \left(\frac{p}{p_0} \right)^2 e^{-\frac{p^2}{p_0^2}} \frac{dp}{p} \\
&= \frac{4}{\sqrt{\pi}} \int_{x_c}^{\infty} x^2 e^{-x^2} dx,
\end{aligned} \tag{4.3}$$

where $x = p/p_0$, $dx = dp/p_0$ and $x_c \equiv x(p_{esc}) = p_{esc}/p_0$. It can then be shown that Equation 4.3 has a solution of the form

$$frac = \frac{2}{\sqrt{\pi}} x_c e^{-x_c^2} + \frac{2}{\sqrt{\pi}} \int_{x_c}^{\infty} e^{-x^2} dx, \tag{4.4}$$

where the second term in the equation can be approximated by a Gaussian error function, i.e.

$$\begin{aligned}
\int_y^{\infty} e^{-x^2} dx &= e^{-y^2} \left[\frac{1}{2y} - \frac{1}{4y^3} + \frac{3}{8y^5} - \dots \right] \\
&\approx \frac{e^{-y^2}}{2y} \rightarrow 0 \quad [\text{for large } y]
\end{aligned}$$

Therefore Equation 4.4 can be approximated by

$$frac \approx \frac{2}{\sqrt{\pi}} x_c e^{-x_c^2}$$

in the limit where $x_c \gg 1$. Writing this in terms of the momentum then gives

$$frac = \frac{2}{\sqrt{\pi}} \left(\frac{p_{esc}}{p_0} \right) e^{-\left(\frac{p_{esc}}{p_0} \right)^2},$$

or alternatively, in terms of velocity

$$frac = \frac{2}{\sqrt{\pi}} \left(\frac{v_{esc}}{v_0} \right) e^{-\left(\frac{v_{esc}}{v_0} \right)^2}.$$

If the material within an area dA is considered, this ratio then has the form

$$\begin{aligned}
\frac{\dot{M}_{esc}}{\dot{M}_{cap}} &\approx \frac{\rho dA v_{esc}}{\rho dA v_0} \int \frac{dn}{n} \\
&\approx \frac{2}{\sqrt{\pi}} \left(\frac{v_{esc}}{v_0} \right) e^{-\left(\frac{v_{esc}}{v_0} \right)^2}.
\end{aligned} \tag{4.5}$$

This expression allows for an order of magnitude estimate of the outflow versus inflow of

material around the compact object in LS 5039 due to thermal evaporation. This approximation ignores any other possible contributions to outflow, such as magnetic pressure exerted by a rotating magnetosphere, to accommodate an accreting BH scenario.

4.3.2 Application to LS 5039

By applying this simple model to LS 5039, it is possible to obtain an order of magnitude approximation of the required temperature before thermal evaporation enables a significant proportion of material to escape the gravitational potential of the compact object.

In order to cover all possible values of LS 5039, a central mass of

$$M_{comp} = 1 \rightarrow 4 M_{\odot},$$

and a temperature between

$$T = 10^5 \rightarrow 10^9 \text{ K},$$

were considered (this wide range of temperatures is unrealistic, but is used to illustrate the problem of thermal evaporation), while the radial distance was chosen to lie between

$$R \sim 3 R_{Schw} \rightarrow R_{acc},$$

where R_{Schw} is the Schwarzschild radius (Equation 2.47) and R_{acc} is the accretion radius for wind accretion systems (Equation 2.15). These limits were chosen because they can be considered as extreme upper and lower limits; the $3 R_{Schw}$ radius since it is the distance of the last stable orbit, and the accretion radius since beyond this point material can no longer be considered as “trapped” by the compact object.

For the mass range considered, the smallest Schwarzschild radius, associated with a $M \sim M_{\odot}$ BH is

$$R_{Schw} = 2.95 \times 10^5 \left(\frac{M}{M_{\odot}} \right) \text{ cm}$$

while the largest accretion radius, associated with a $M \sim 4 M_{\odot}$ BH is

$$\begin{aligned} R_{acc} &\sim \frac{2GM_{acc}}{v_{rel}^2} \\ &\sim 1.7 \times 10^{10} \left(\frac{M}{4 M_{\odot}} \right) \left(\frac{v_{rel}}{\sqrt{(2.44 \times 10^8)^2 + (5.9 \times 10^7)^2}} \right)^{-2} \text{ cm}. \end{aligned}$$

Here $v_{rel} = \sqrt{v_w^2 + v_n^2}$, and $v_n \approx 590 \text{ km s}^{-1}$ (Table 4.1) and $v_w \approx v_{\infty} = 2440 \text{ km s}^{-1}$. This then implies a range of radial values between

$$\begin{aligned}
R &= 3R_{Schw} \rightarrow R_{acc} \\
&\approx 10^6 \rightarrow 10^{10} \text{ cm} \\
&\sim 1 \rightarrow 10000 R_6
\end{aligned}$$

where $R_6 = 10^6$ cm, would cover the most viable values for the system.

Figures 4.3–4.6 show the graphical solutions for this model. What is clear from the results is that $T > 10^7$ K before a significant amount of material can evaporate from a disc or ring orbiting outside the last stable orbital radius ($r > 3R_{Schw}$). This is supported by the fact that viscous dissipation in a disc at $r > 3R_{Schw}$ can result in a temperature of (Equation 2.25)

$$\begin{aligned}
T(R) &= \left\{ \frac{3GM\dot{M}}{8\pi R^3\sigma} \left[1 - \left(\frac{R_*}{R} \right)^{1/2} \right] \right\}^{1/4} \\
&\leq 1.5 \times 10^6 \left(\frac{M_*}{3M_\odot} \right)^{1/4} \left(\frac{\dot{M}}{3 \times 10^{14} \text{ g s}^{-1}} \right)^{1/4} \left(\frac{R}{3R_{Schw}} \right)^{-3/4} \text{ K}.
\end{aligned}$$

Here an accretion rate of $\dot{M} \leq 3 \times 10^{14} \text{ g s}^{-1}$, and

$$R_{Schw} \approx 9 \times 10^5 \left(\frac{M}{3M_\odot} \right) \text{ cm},$$

were used. This casts serious doubt on whether any outflow is related to thermal evaporation from a disc or ring orbiting an accreting BH.

It should be noted that the wave shape visible in Figures 4.5 & 4.6 is due to the shape of Equation 4.5,

$$f(x) = x^2 e^{-x^2},$$

which is shown in Figure 4.7. The assumption made during the derivation of Equation 4.5 implies that it is only valid in the case of $x \gg 1$, i.e. when $v_{esc} \gg v_0$. This limitation in Equation 4.5 does not invalidate the conclusion drawn about the thermal limit, since this is based on the results where the condition $v_{esc} \gg v_0$ still holds.

These estimates suggest that a thermal outflow mechanism producing an outflow in LS 5039 is probably not realistic. This is to some extent also supported by the absence of any disc related black body or thermal bremsstrahlung signature in the spectrum of LS 5039, since the black body component in the non-thermal dominated spectrum is only associated with the optical companion. However, the possibility of a magnetohydrodynamic wind process cannot be excluded, but since it relies on a model dependent scenario (i.e. relies on assumptions made in the Blandford-Znajek model), it is impossible to evaluate without introducing several assumptions related to BHs and disc magnetic fields, without any observational backup.

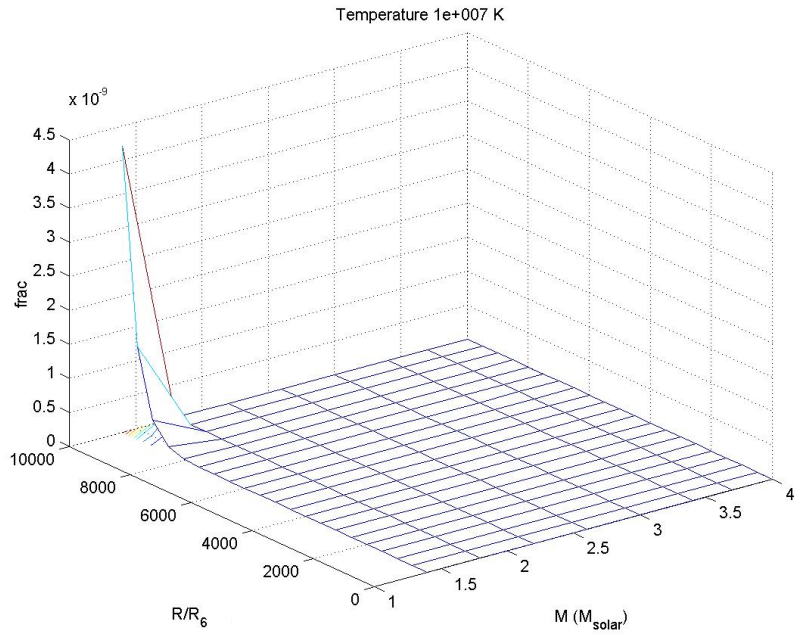


Figure 4.3: Fraction of material escaping through thermal evaporation at $T = 10^7$ K.

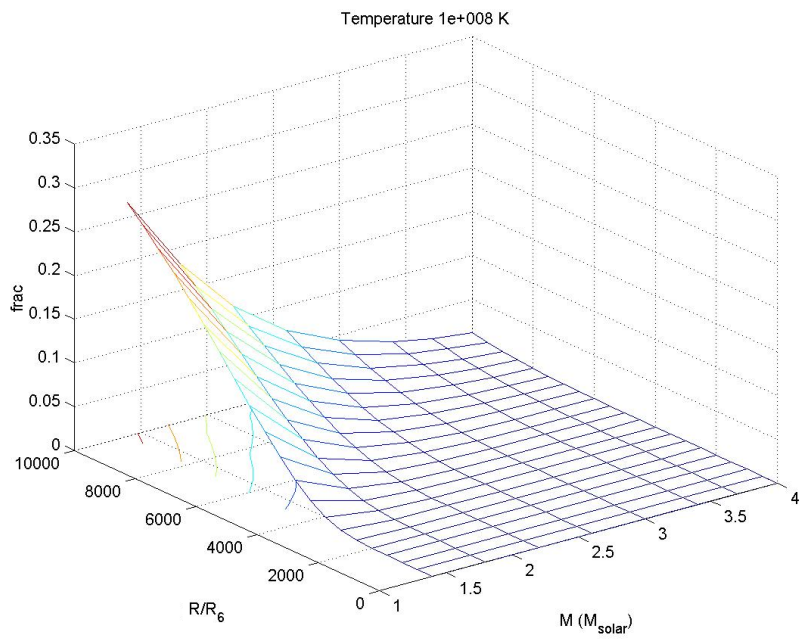


Figure 4.4: Fraction of material escaping through thermal evaporation at $T = 10^8$ K.

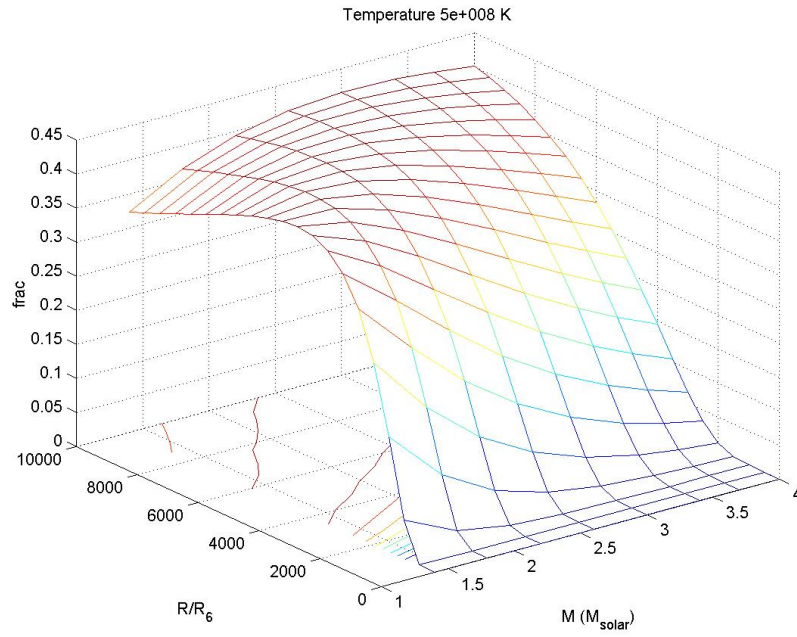


Figure 4.5: Fraction of material escaping through thermal evaporation at $T = 5 \times 10^8$ K.

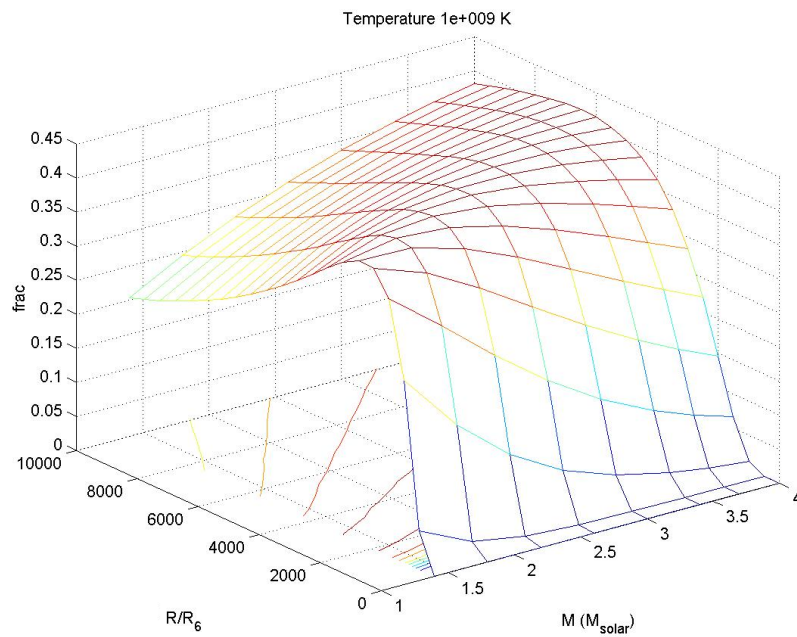


Figure 4.6: Fraction of material escaping through thermal evaporation at $T = 10^9$ K.

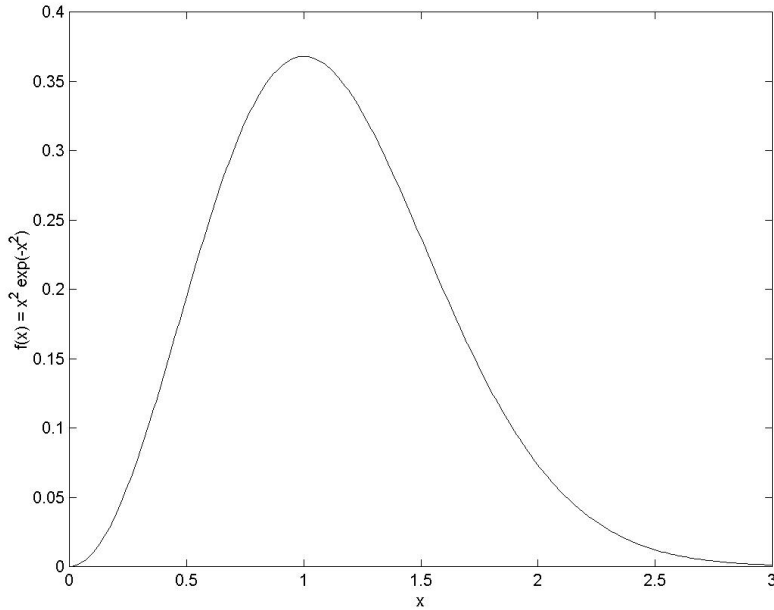


Figure 4.7: Shape of the function $f(x) = x^2 \exp(-x^2)$.

Introducing a rotating magnetized NS provides two benefits. First, spin-down power provides an additional source for the required energy of the system and second, the magnetosphere provides a mechanism to drive mass outflow in the system.

Figure 4.8 shows the spin down luminosity that can be extracted from a pulsar that is spinning down (Equation 2.43). The shaded area represents the region where the spin-down luminosity lies within $10^{34} \leq \dot{E} \leq 10^{38} \text{ erg s}^{-1}$. This provides a wide range of parameter space associated with fast rotating NSs ($0.01 \leq P_{rot} \leq 2.5 \text{ sec}$; $\sim 10^{-16} \leq \dot{P} \leq \sim 10^{-13} \text{ s s}^{-1}$), providing sufficient spin-down power to drive the maximum VHE gamma-ray emission with a luminosity of $L_\gamma \sim 10^{34} \text{ erg s}^{-1}$.

4.4 A Magnetized Compact Object

The previous section has shown the inconsistency associated with a thermal jet originating from a disc or ring structure around a BH. This strongly suggests that a different approach is needed to explain LS 5039, especially the non-thermal emission at energies $\epsilon_\gamma > 1 \text{ GeV}$. It is for this reason that a fast rotating magnetized compact object is considered, specifically a NS, since this is consistent with the implied mass limits (see Section 4.2.1).

The scenario is then envisaged as follows; a NS is in orbit around the optical companion and material is captured by the gravitational potential of the compact object. This material then

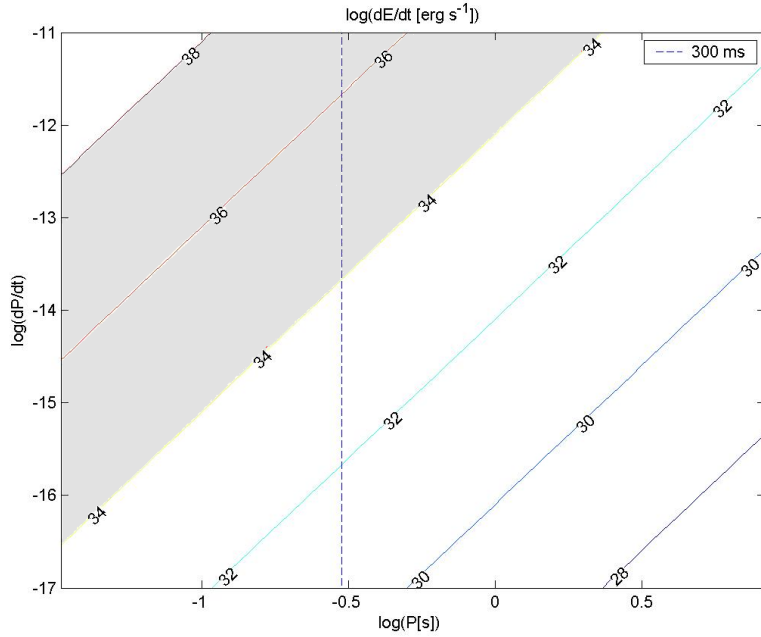


Figure 4.8: Range of spin-down luminosities, typical of pulsars. The vertical dashed line shows a spin period of 300 ms.

attempts to accrete onto the surface of the NS while interacting with the magnetosphere. It is this interaction between the magnetic field (originating from the NS) and the material that is attempting to accrete that must now be investigated. The following sections will attempt to model the broad-band emission from the system. In order to do so, two questions must be answered;

1. The influence of a rotating magnetosphere on the mass flow dynamics in the system, and
2. The role it plays in driving the broad-band non-thermal emission from radio to VHE gamma-ray energies.

In order to answer the question of the flow, it will be necessary to consider the position of the Alfvén radius and the effective gravity experienced, while to understand the radiation process, the required magnetic field strengths and the Lorentz factors of the accelerated particles must be determined. These questions will be investigated in six steps:

1. Considering the requirement for producing the high energy non-thermal gamma-ray emission detected by EGRET and H.E.S.S., including
 - The required magnetic field strength and Lorentz factor of the particles and
 - Whether the interactions will occur in the Thomson or Klein-Nishina limits.

2. Considering how the magnetic field strength decreases with distance if it is assumed that the field is dipolar, i.e. $B(r) \propto 1/r^3$.
3. Assuming the magnetic field interacts with the fraction of the stellar wind captured by the gravitational potential of the compact object, the point at which the condition $B^2/(8\pi) = \rho v^2$ is satisfied must be considered. This will be approximated from the Alfvén radius analysis performed earlier (Section 2.2.4).
4. If the non-thermal emission occurs at the Alfvén radius, the constraints this places on the EGRET and TeV energy gamma-ray emission must be determined.
5. Assuming the magnetosphere is rapidly rotating – as would be expected in a NS/pulsar scenario – the effective gravity of the accreting particles must be considered. This will play a significant role for any possible pulsar wind outflow.
6. Finally it should be determined whether sufficient power can be dissipated by a MHD shock front to account for the TeV gamma-ray energies.

The next six sections will look at each of these questions and use them to build up a model for LS 5039.

4.4.1 Requirements of High Energy Non-thermal Emission

The first step is to consider the expected conditions of the non-thermal emission from LS 5039. Specifically, the requirements for synchrotron and IC radiation to be able to produce the VHE energy emission, and the regime in which IC scattering will occur, must be considered.

High Energy Gamma-ray Production

LS 5039 emits high energy gamma-rays, first detected by EGRET, and later confirmed (up to TeV levels) by H.E.S.S. Since this is of a non-thermal origin, it is of interest whether it is the result of synchrotron or IC radiation. Rigid constraints will not be implied at this point; instead estimates of the requirements for this to occur will be considered. This will be used for comparison, once more rigid constraints are placed on the production site.

The critical frequency of synchrotron radiation (Equation 3.7) implies a dependence on the magnetic field,

$$H \approx \frac{\nu_c}{6.266 \times 10^{18} E^2},$$

under the assumption that $\sin \psi \approx 1$, where ψ is the pitch angle. Here ν_c is the critical frequency and $E = \gamma m_e c^2$ is the energy of the relativistic electron. The maximum luminosity of the EGRET emission occurs at $\epsilon_\gamma \sim 10^{10}$ eV, which translates to a frequency of

$$\nu_c \sim 2.4 \times 10^{24} \text{ Hz.}$$

If it is assumed that the radiating electron has an energy of $E \sim 1 \text{ TeV} \sim 1 \text{ erg}$, the required magnetic field strength is

$$H \approx 4 \times 10^5 \left(\frac{\nu_c}{2.4 \times 10^{24} \text{ Hz}} \right) \left(\frac{E}{1 \text{ erg}} \right)^{-2} \text{ G}.$$

Such a magnetic field strength is not unusual in astrophysical sources. However the condition becomes more severe when frequencies consistent with the H.E.S.S. detection are considered. In this case $\epsilon_\gamma \sim 10^{13} \text{ eV}$, implying

$$\nu_c \sim 2.4 \times 10^{27} \text{ Hz},$$

which increases the required magnetic field strength to

$$H \approx 4 \times 10^8 \left(\frac{\nu_c}{2.4 \times 10^{27} \text{ Hz}} \right) \left(\frac{E}{1 \text{ erg}} \right)^{-2} \text{ G},$$

for a similar electron energy. Such a requirement, as will be seen later, requires the synchrotron cooling to occur close to the surface of the NS. There are, however, questions around whether emission at EGRET energies and above can still be considered as synchrotron radiation or whether it is produced by IC radiation. Dubus (2006b) (Figure 3.12) calculates this region as tail-end synchrotron radiation and peak IC radiation, and similarly microquasar modelling by Paredes et al. (2006) (Figure 4.9) used an accretion disc and jet structures to match this emission (the model also assumed a coronal emission, accretion stream and an equatorial wind from the mass donor to increase the accretion rate).

If instead IC radiation in the Klein-Nishina limit is considered, the required Lorentz factor is determined from (Equation 3.13)

$$\gamma \gtrsim \frac{\epsilon_\gamma}{m_e c^2}.$$

For the EGRET region this translates to

$$\gamma \gtrsim 2 \times 10^4 \left(\frac{\epsilon_\gamma}{10^{10} \text{ eV}} \right),$$

while it was shown in Section 4.1, the requirement in the H.E.S.S. regime is

$$\gamma \gtrsim 6 \times 10^7 \left(\frac{\epsilon_\gamma}{3 \times 10^{13} \text{ eV}} \right).$$

Both the synchrotron and IC radiation mechanism, as shown above, require ultra-relativistic particle energies to produce the observed high energy gamma-ray emission. However, the advantage of the IC radiation mechanism is that it does not rely on a magnetic field, simply requiring a sufficient photon field in the vicinity of the accelerating region. This requirement is satisfied by the radiation field of the optical companion. Since IC scattering may play a role in the emission process, it is now necessary to determine the point where the scattering must be considered in

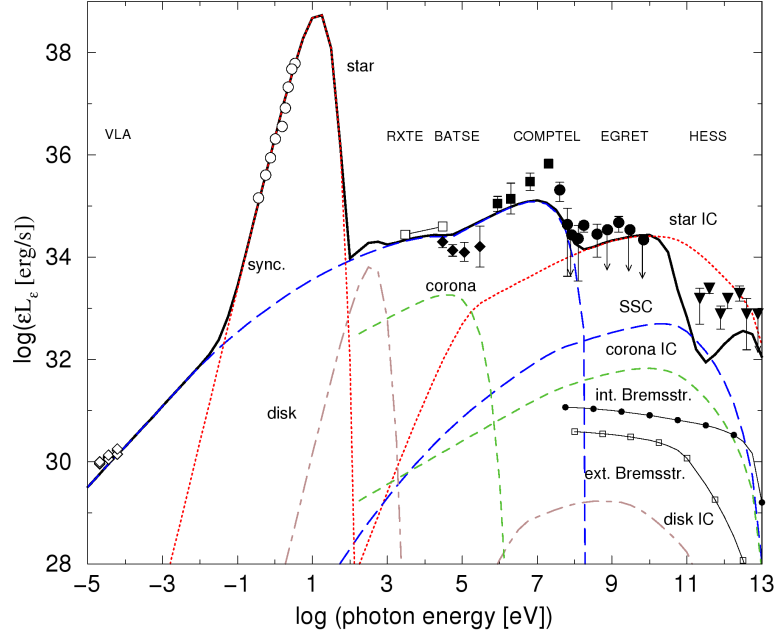


Figure 4.9: Microquasar model for LS 5039 (Paredes et al., 2006). The model assumed the presence of an accretion disc and jet structure, as well as an increased accretion rate from a proposed equatorial wind and accretion stream from the mass donor. A coronal emission was also considered.

the Klein-Nishina limit.

Cross Section

When considering IC radiation it is necessary to determine whether the scattering will occur in the Thomson or Klein-Nishina regime, since this influences the energy transfer process during the photon scattering. Equations 3.12 give the detailed equations for the scattering cross section and show that the boundary between the Thomson and Klein-Nishina regime occurs when (Blumenthal and Gould, 1970)

$$\gamma h\nu \approx m_e c^2, \quad (4.6)$$

where γ is the Lorentz factor of the electron before scattering. This notation considers the photon energy in the rest frame of the electron. For electrons moving through a photon field, the scattering will then occur in the Klein-Nishina limit when the frequency of the photon is

$$\nu > \frac{m_e c^2}{\gamma h}.$$

The required Lorentz factors for IC radiation estimated above were 2×10^4 and 6×10^7 for the EGRET and H.E.S.S. respectively. By using these values the frequency above which the

scattering will enter the Klein-Nishina limit is then

$$\nu_{EGRET} > 6 \times 10^{15} \left(\frac{\gamma}{2 \times 10^4} \right) \text{ Hz}$$

and

$$\nu_{HESS} > 2 \times 10^{12} \left(\frac{\gamma}{6 \times 10^7} \right) \text{ Hz},$$

for the EGRET and H.E.S.S. energy requirements respectively. Since the radiation field is dominated by the radiation of the blue optical companion ($\nu \sim 10^{15}$ Hz), the IC scattering for both EGRET and H.E.S.S. gamma-rays will be in the Klein-Nishina limit.

The approximations for the required magnetic field and Lorentz factor made above, will provide a comparison for the more stringent constraints that will be placed on these values once the position of the Alfvén radius has been determined. Before proceeding to do so, the decrease in the magnetic field strength with distance will be considered, so that the position of the non-thermal radiation region can be constrained.

4.4.2 Magnetic Field Strength

The non-thermal signature of emission, especially the synchrotron component, requires a sufficiently strong magnetic field strength. The estimated magnetic field strengths were $\sim 10^5$ G and $\sim 10^8$ G for the EGRET and H.E.S.S. detections respectively, suggesting that if synchrotron radiation is responsible for the emission, the site of emission must lie close to the compact object. If the magnetic field associated with the compact object is considered to be dipolar then at a distance r , $B(r)$ can be approximated by Equation 2.29, leading to a magnetic field strength that falls off as

$$B \propto \frac{1}{r^3}.$$

The region of interest is then from the surface of the NS, $R_{NS} = 10^6$ cm, to the boundary of the binary system at $R \sim 10^{12}$ cm. In such a scenario Figure 4.10 shows the decrease in magnetic field strength with distance for four different surface field strengths, namely 10^6 G, 10^9 G, 10^{12} G and 10^{15} G. This covers a wide range of magnetic fields that can be considered for a NS, from radio pulsars with, $B \sim 10^6$ G, to magnetars, $B \sim 10^{15}$ G. Very simply this shows that the magnetic field strength becomes very low when distances approaching the binary separation are considered.

In order to satisfy the high magnetic field required for synchrotron radiation to be responsible for the high energy gamma-ray emission, the emission site must lie close to the compact object. To satisfy the 10^5 G requirement of the EGRET detection the production site must lie well within a radius of 10^9 cm, for a NS with a surface magnetic field strength of 10^{12} G.

It is now necessary to further constrain the emission by considering the point at which the magnetic pressure will become dominant with respect to the inflowing material that is captured from the stellar wind of the optical companion.

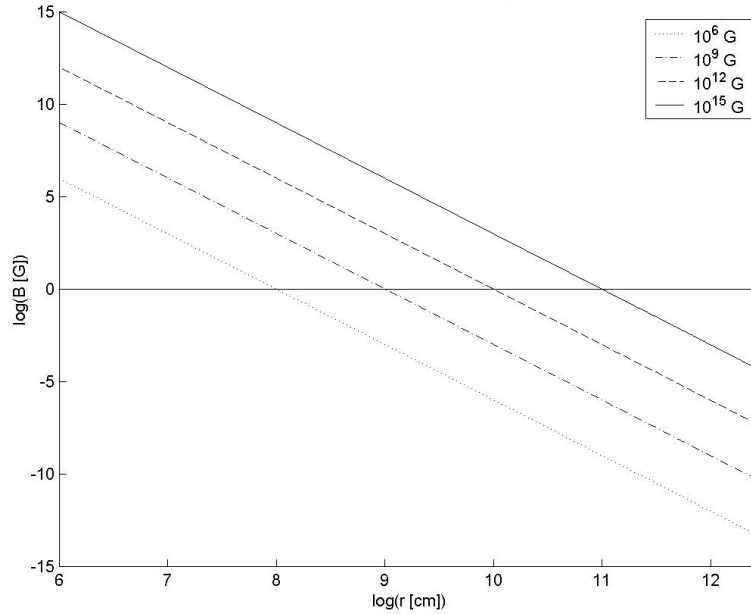


Figure 4.10: Magnetic fields strength as a function of distance for surface field strengths of 10^6 G, 10^9 G, 10^{12} G and 10^{15} G.

4.4.3 Magnetosphere–Stellar Wind Interaction

Any significant magnetospheric interaction with the inflowing material will occur when the magnetospheric pressure reaches equilibrium with the ram pressure exerted by the inflow, i.e. the Alfvén radius. As discussed in Section 2.2.4, the Alfvén radius occurs at the point where the magnetic pressure equals that of the ram pressure of the inflowing material, such that

$$\frac{B(r)^2}{8\pi} = \rho_w v^2.$$

In the scenario presented here the inflowing material is the fraction of the stellar wind that has been captured by the gravitational potential. As was shown in Section 4.2.2, this is approximately $\dot{M} \sim 3 \times 10^{14} \text{ g s}^{-1}$.

Compact Object

Values for the mass and surface magnetic field strength were chosen to cover a wide range of possible values for a NS. The mass values examined were $1.4 M_\odot$, $1.8 M_\odot$, $2.2 M_\odot$, $2.6 M_\odot$ and $3.0 M_\odot$, while the surface magnetic field strengths ranged between $10^6 - 10^{13}$ G. For all masses an assumed radius of $R_{NS} \sim 10^6 \text{ cm}$ ($\sim 10 \text{ km}$) was used.

Alfvén Radius

At the Alfvén radius the magnetic field begins to have a significant influence on the motion of the inflowing material. If it is assumed that the captured material flows in spherically with a free fall velocity, the distance to the Alfvén radius, from the accreting compact object, is

$$r_{Alf} = 1.4 \times 10^9 \left(\frac{\dot{M}}{3 \times 10^{14} \text{ g s}^{-1}} \right)^{-2/7} \left(\frac{M_*}{M_\odot} \right)^{-1/7} \left(\frac{\mu}{10^{30} \text{ G cm}^3} \right)^{4/7} \text{ cm.}$$

From this the position of the Alfvén radius was calculated for the parameter range described above. In each case the appropriate fraction, $(\dot{M})/(\zeta \dot{M}_{wind})$, as given in Table 4.2, was used to calculate the accretion rate for each mass.

Figures 4.11–4.13 show the position of the Alfvén radius as it varies with surface magnetic field strength for three different masses ($M = 1.4 M_\odot$, $2.2 M_\odot$ & $3.0 M_\odot$) and Tables 4.3–4.5 show the numerical values along with the associated magnetic field strength. As expected, the position of the Alfvén radius is far more dependent on the surface magnetic field strength than the mass of the compact object. This is due to the fact that

$$r_{Alf} \propto M^{-1/4}$$

while

$$r_{Alf} \propto B^{4/7},$$

but also because the mass range covered is small in comparison to the large order of magnitude range covered by the surface magnetic field strength.

The calculations show that for a magnetic field strength $B = 10^6$ G, the Alfvén radius is less than the radius of a NS, implying that for low magnetic fields the accretion is unaffected by the magnetic field. In addition these calculations show that for the values of the parameters considered, the Alfvén radius lies within $\sim 3 \times 10^9$ cm. This is well within the binary system, and orders of magnitude away from the optical companion. Since $B \sim 10^{12}$ G can be considered as a typical value of a NS, and it is not expected that the values in LS 5039 could greatly exceed this, the results imply that the synchrotron emission region will definitely be within the binary system and centred on the compact object. This is consistent with the observed orbital modulation (see Section 1.3.3 & 1.3.4).

Since it can be assumed the non-thermal radiation originates close to the Alfvén radius it is now necessary to re-evaluate the requirements for this emission at this new distance.

4.4.4 Non-thermal Radiation at the Alfvén radius

Re-evaluating the non-thermal radiation at the Alfvén radius allows for more stringent constraints to be applied to the system. The first conclusion that can be drawn is that there is no scenario in which the magnetic field strength is high enough ($> 10^8$ G) to be able to explain the TeV

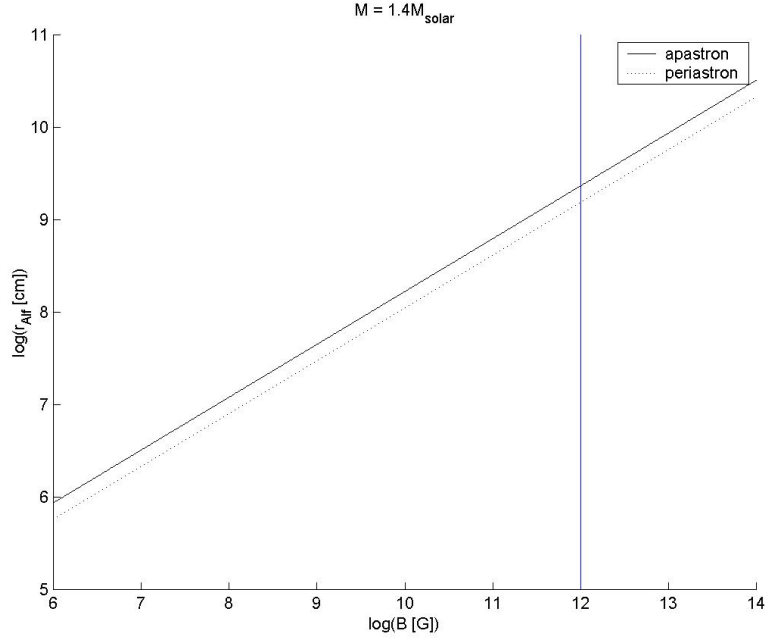


Figure 4.11: The position of the Alfvén radius plotted against magnetic field strength for $1.4 M_{\odot}$. The values of both periastron and apastron are shown. The solid vertical line indicates the position of 10^{12} G.

Table 4.3: Alfvén radius for $1.4 M_{\odot}$ compact object.

$\log(B)$	r_{Alf} (10^9 cm) <i>periastron</i>	r_{Alf} (10^9 cm) <i>apastron</i>	$B(r_{Alf})$ (G) <i>periastron</i>	$B(r_{Alf})$ (G) <i>apastron</i>
6	0.0006	0.0009	4.63E+06	1.37E+06
7	0.0021	0.0032	1.08E+06	3.05E+05
8	0.0080	0.0121	1.95E+05	5.64E+04
9	0.0298	0.045	3.78E+04	1.10E+04
10	0.1113	0.1676	7.25E+03	2.12E+03
11	0.4147	0.6246	1.40E+03	4.10E+02
12	1.5459	2.3284	2.71E+02	7.92E+01

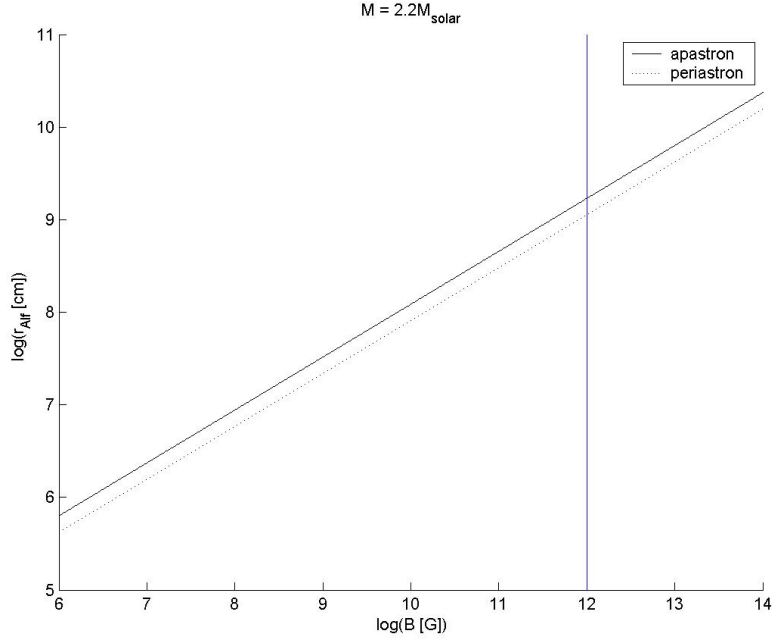


Figure 4.12: The position of the Alfvén radius plotted against magnetic field strength for $2.2 M_{\odot}$. The values of both periastron and apastron are shown. The solid vertical line indicates the position of 10^{12} G.

Table 4.4: Alfvén radius for $2.2 M_{\odot}$ compact object.

$\log(B)$	r_{Alf} (10^9 cm) <i>periastron</i>	r_{Alf} (10^9 cm) <i>apastron</i>	$B(r_{Alf})$ (G) <i>periastron</i>	$B(r_{Alf})$ (G) <i>apastron</i>
6	0.0004	0.0006	1.56E+07	4.63E+06
7	0.0016	0.0024	2.44E+06	7.23E+05
8	0.0058	0.0088	5.13E+05	1.47E+05
9	0.0217	0.0327	9.79E+04	2.86E+04
10	0.0810	0.1221	1.88E+04	5.49E+03
11	0.3021	0.4550	3.63E+03	1.06E+03
12	1.1261	1.6962	7.00E+02	2.05E+02

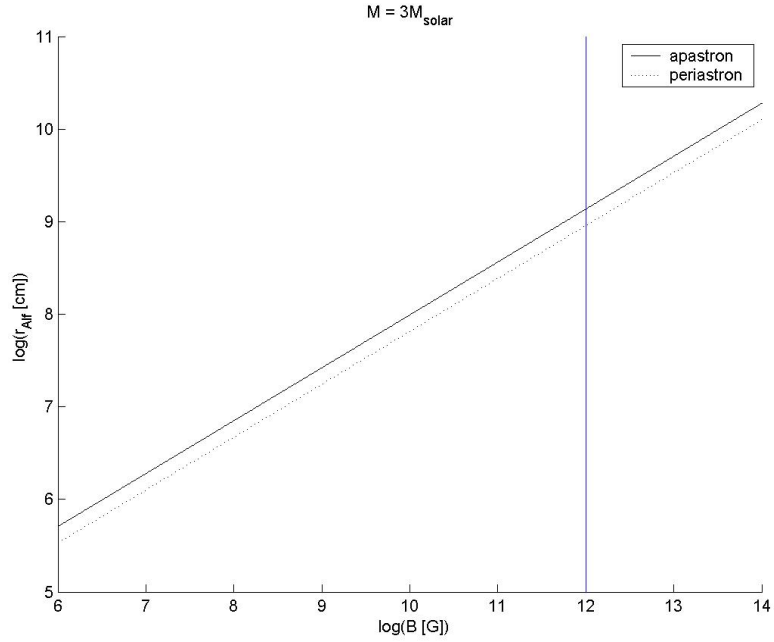


Figure 4.13: The position of the Alfvén radius plotted against magnetic field strength for $3.0 M_{\odot}$. The values of both periastron and apastron are shown. The solid vertical line indicates the position of 10^{12} G.

Table 4.5: Alfvén radius for $3.0 M_{\odot}$ compact object.

$\log(B)$	r_{Alf} (10^9 cm) <i>periastron</i>	r_{Alf} (10^9 cm) <i>apastron</i>	$B(r_{Alf})$ (G) <i>periastron</i>	$B(r_{Alf})$ (G) <i>apastron</i>
6	0.0003	0.0005	2.54E+07	8.00E+06
7	0.0013	0.0019	5.00E+06	1.46E+06
8	0.0047	0.0071	9.63E+05	2.79E+05
9	0.0175	0.0264	1.86E+05	5.43E+04
10	0.0653	0.0984	3.59E+04	1.05E+04
11	0.2435	0.3668	6.93E+03	2.03E+03
12	0.9076	1.3672	1.34E+03	3.91E+02

Table 4.6: Lorentz factors of particles for synchrotron radiation.

B_*	$1.4 M_\odot$		$2.2 M_\odot$		$3.0 M_\odot$	
	<i>periastron</i>	<i>apastron</i>	<i>periastron</i>	<i>apastron</i>	<i>periastron</i>	<i>apastron</i>
10^7	7.85×10^5	1.48×10^6	5.22×10^5	9.59×10^5	3.65×10^5	6.75×10^5
10^8	1.85×10^6	3.43×10^6	1.14×10^6	2.13×10^6	8.31×10^5	1.54×10^6
10^9	4.19×10^6	7.78×10^6	2.61×10^6	4.82×10^6	1.89×10^6	3.50×10^6
10^{10}	9.57×10^6	1.77×10^7	5.94×10^6	1.10×10^7	4.30×10^6	7.96×10^6
10^{11}	2.18×10^7	4.03×10^7	1.35×10^7	2.50×10^7	9.80×10^6	1.81×10^7
10^{12}	4.96×10^7	9.16×10^7	3.08×10^7	5.70×10^7	2.23×10^7	4.12×10^7

emission via synchrotron radiation. This is a strong indication that the TeV emission must occur through IC radiation.

The required Lorentz factor of an electron capable of producing the EGRET level emission through synchrotron radiation ($\epsilon_\gamma \sim 10^{10}$ eV) can be determined by rearranging Equation 3.7; this results in

$$\begin{aligned} \gamma^2 &= \frac{4\pi}{3} \frac{m_e c}{e \sin \psi} \frac{\nu_c}{H} \\ &\approx 2.75010 \times 10^{-7} \frac{\nu_c}{H} \quad \text{for } \psi = 60^\circ. \end{aligned}$$

If the EGRET energy is used, the Lorentz factor can then be approximated by

$$\gamma \approx \left(6.65 \times 10^{17} \frac{1}{H} \right)^{1/2}.$$

Table 4.6 list numerical values for the required Lorentz factors at the Alfvén radii (Section 4.4.3), if a $B(r) \propto r^{-3}$ dipolar scaling law is adopted.

These estimations show that the required Lorentz factor for synchrotron radiation for realistic NS magnetic field strengths ($B > 10^9$ G) is $\gamma > 10^6$. This is greater than the Lorentz factor required by IC radiation in the Klein-Nishina limit to produce the same radiation, i.e

$$\begin{aligned} \gamma &\gtrsim \frac{\epsilon_\gamma}{m_e c^2} \\ &\gtrsim 2 \times 10^4. \end{aligned}$$

Therefore it can be seen that the IC radiation slackens the stringent requirements placed on the electron energies to produce high energy gamma-ray emission ($\epsilon_\gamma \gtrsim 10$ GeV).

Cross Section

The Lorentz factors of the electrons have a direct influence on the scattering cross section during Thomson scattering. Since it is likely that IC radiation is responsible for the gamma-ray emission,

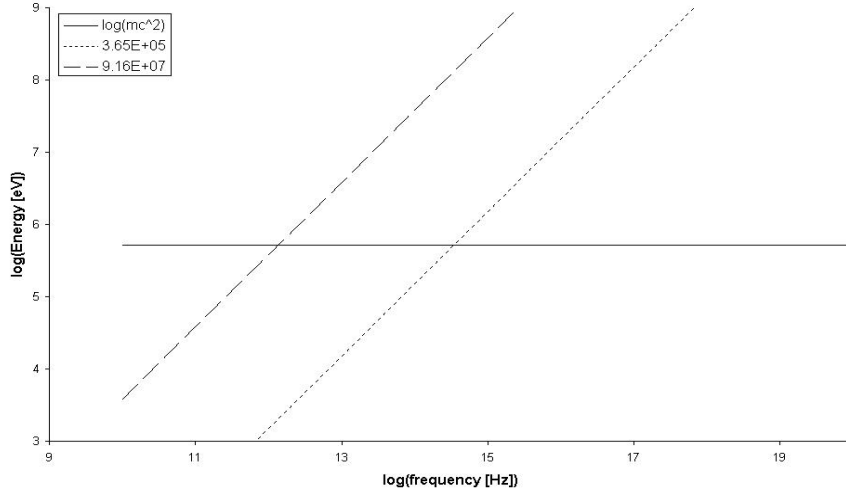


Figure 4.14: The figure shows $\gamma h\nu$ plotted versus frequency. The horizontal line represents the rest mass energy of an electron.

the question of whether the scattering will occur in the Thomson or the Klein-Nishina regime must be re-examined for the new constraints on the Lorentz factor.

The boundary between the Thomson and Klein-Nishina region occurs when (Equation 4.6)

$$\gamma h\nu \approx m_e c^2.$$

When $\gamma h\nu \gg m_e c^2$ the cross section must be considered in the Klein-Nishina limit. The range of Lorentz factors calculated in Section 4.4.4 (see Table 4.6) has a minimum value of $\gamma = 3.65 \times 10^5$ and a maximum value of $\gamma = 9.16 \times 10^7$. In order to obtain an estimate of the frequency at which the condition $\gamma h\nu \gg m_e c^2$ is met, $\gamma h\nu$ is plotted (in units of eV) for these two values in Figure 4.14.

The graph shows that $\gamma h\nu = m_e c^2$ occurs roughly between $10^{12} - 10^{15}$ Hz. Since the optical companion has an effective temperature of $T_{eff} \approx 40\,000\text{ K}$, the average energy of the radiation field it produces is $\langle \epsilon \rangle = 2.7 kT_{eff}$, resulting in

$$\begin{aligned} \langle \nu_\gamma \rangle &= \frac{2.7 kT_{eff}}{h} \\ &\approx 2.3 \times 10^{15} \left(\frac{T_{eff}}{40\,000\text{ K}} \right) \text{ Hz}. \end{aligned}$$

Then for $\gamma > 10^6$, which implies IC scattering in the Klein-Nishina limit of photons with $\nu \gg 10^{14}$ Hz, the up-scattering of photons from the optical companion will most likely occur in the Klein-Nishina limit.

However for $\gamma \sim 10^4 - 10^5$ the IC scattering with photons $\langle \nu \rangle \sim 10^{15}$ Hz probably still occurs

in the (approximate) Thomson limit. It can be seen that this is sufficient to pump up photons ($\epsilon_{\gamma,int} \sim 10$ eV) to energies between

$$\epsilon_{\gamma} \sim 1 \left(\frac{\gamma}{10^4} \right)^2 \left(\frac{\langle \epsilon_{\gamma,int} \rangle}{10 \text{ eV}} \right) \text{ GeV}$$

to

$$\epsilon_{\gamma} \sim 100 \left(\frac{\gamma}{10^5} \right)^2 \left(\frac{\langle \epsilon_{\gamma,int} \rangle}{10 \text{ eV}} \right) \text{ GeV}$$

This is reconcilable with the EGRET emission.

Synchrotron Self-Compton

The other factor that cannot be ignored is that the *synchrotron self-Compton* (SSC) process may also play a role. Relativistic electrons can create synchrotron radiation, which can then be up-scattered through IC scattering by the relativistic electrons. IC scattering will occur in the Klein-Nishina limit if the frequency of the photon is

$$\begin{aligned} \nu &\gg \frac{m_e c^2}{h\gamma} \\ &\gg 6.2 \times 10^{15} \left(\frac{\gamma}{2 \times 10^4} \right)^{-1} \text{ Hz.} \end{aligned}$$

To create photons of $\nu \approx 6.2 \times 10^{15}$ Hz through synchrotron radiation (assuming the emission is at the critical frequency), the required magnetic field strength is (Equation 3.7)

$$\begin{aligned} B &= \frac{4\pi m_e c}{3 e} \frac{\nu_c}{\gamma^2 \sin \psi} \\ &\approx \frac{\nu_c}{3.6 \times 10^6 \gamma^2} \quad \text{for } \psi = 60^\circ \\ &\sim 5 \left(\frac{\nu_c}{6.2 \times 10^{15} \text{ Hz}} \right) \left(\frac{\gamma}{2 \times 10^4} \right)^{-2} \text{ G.} \end{aligned}$$

Magnetic field strengths of this magnitude are easily obtained and exceeded at the Alfvén radius. For a frequency $\nu < 10^{15}$ Hz, IC scattering in the Thomson limit would produce a photon with a maximum energy of

$$\begin{aligned} \epsilon_{\gamma} &= 4\gamma^2 h\nu \\ &\approx 1.7 \times 10^9 \left(\frac{\gamma}{10^4} \right)^2 \left(\frac{\nu}{10^{15} \text{ Hz}} \right) \text{ eV.} \end{aligned}$$

This is consistent with the EGRET emission.

Table 4.7 lists additional Lorentz factors, with the appropriate frequency limit, and the required magnetic field strength for SSC to occur. Included are the photon energies of photons up-scattered by IC in the Thomson and Klein-Nishina limit (in the Thomson limit a frequency of

Table 4.7: The Klein-Nishina frequency limit and required magnetic field strength for Synchrotron self-Compton radiation, for various particle energies. The required magnetic field strengths become very low (unrealistically for the binary system), which illustrates the high likelihood of Synchrotron self-Compton occurring in the system.

Lorentz factor	Frequency limit (Hz)	Magnetic field (G)	IC radiation	
			Thomson limit (eV)	Klein-Nishina limit (eV)
10^4	10^{16}	3	1.65×10^9	5.11×10^9
10^5	10^{15}	3×10^{-2}	1.65×10^{10}	5.11×10^{10}
10^6	10^{14}	3×10^{-5}	1.65×10^{11}	5.11×10^{11}
10^7	10^{13}	3×10^{-8}	1.65×10^{12}	5.11×10^{12}
10^8	10^{12}	3×10^{-11}	1.65×10^{13}	5.11×10^{13}

one tenth of the critical frequency is used to approximate the condition $\gamma h\nu \ll m_e c^2$). The low requirements on the magnetic field strengths indicates that a SSC process can most definitely drive the gamma-ray emission at energies $\epsilon > 10^9$ eV with rather modest requirements in terms of electron energy.

SSC process complicates the radiation emission mechanism. If it is assumed that the bulk of IC scattering occurs off the optical photons, the Lorentz factors ($\sim 10^6$) required to produce TeV energy gamma-rays will result in the scattering occurring in the Klein-Nishina limit. If, however, SSC is considered, additional scattering of synchrotron produced photons could result in high energy emission begin created in the Thomson limit. The concern is whether sufficient synchrotron photons exist to produce the luminosity of the VHE emission.

The details of such a process are beyond the scope of this study as the goal is simply to demonstrate the ability of a magnetized NS system to produce the non-thermal emission. The conclusion that is drawn is that it is more likely that the high energy ($> 10^9$ eV) is created through IC radiation than synchrotron radiation.

4.4.5 Effective Gravity: A MHD Propeller in LS 5039

The preceding sections have considered the effect of a magnetized compact object in LS 5039 by considering the position of the Alfvén radius, and the Lorentz factor that particles would require at that point. Since it is believed that IC scattering in the ultra-relativistic case is required to produce the TeV energy gamma-rays, the requirement of a very large Lorentz factor, $\gamma > 10^6$, must still be met irrespective of the model applied. Attention will now be shifted from the radiation effects of a magnetic field, to the effect that a rotating magnetosphere will have on the accretion flow.

It has already been shown in Section 3.3.1 that magnetic field lines connected to an accretion disc can remove material from the disc and that the effective gravitational potential is given by

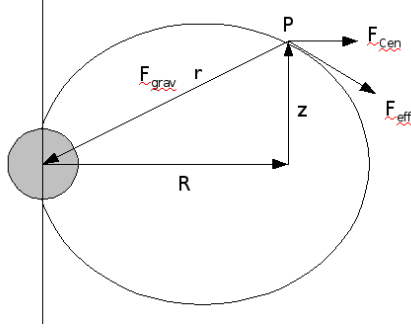


Figure 4.15: Sketch of the forces acting on a test particle attached to a field line at point P.

(Equation 3.25),

$$\Phi_{eff} = \Phi_{grav} - \frac{1}{2} (|\boldsymbol{\Omega} \times \mathbf{R}|^2).$$

A similar scenario can be considered without an accretion disc. Consider a test particle attached to the field lines (point P) of a magnetosphere co-rotating with a compact object with angular velocity Ω , as shown in Figure 4.15. In the rotating frame this results in an inward acceleration due to gravity and an outwards acceleration due to the centrifugal force. In a co-rotating reference frame the effective gravitational potential experienced by the particle is (in cylindrical coordinates)

$$\Phi_{eff} = -\frac{GM}{(R^2 + z^2)^{1/2}} - \frac{1}{2}\Omega^2 R^2,$$

where M is the mass of the central gravitating object. The effective gravity is then determined by

$$\begin{aligned} g_{eff} &= -\nabla\Phi_{eff} \\ &= -\frac{GM}{r^2}\hat{e}_r + \Omega^2 R\hat{e}_R, \end{aligned} \quad (4.7)$$

where $\mathbf{r} = R\hat{e}_R + z\hat{e}_z$ and $\hat{e}_r = \frac{\mathbf{r}}{|\mathbf{r}|}$. If $g_{eff} > 0$, the particle experiences an effective force that drives it out of the system*.

A consequence of this effective gravity model that should be mentioned here, is the possibility of jet formation through magnetic collimation. If only the R-components of Equation 4.7 are considered, the acceleration due to the gravitational and centrifugal forces are

$$g_{grav}\hat{e}_R = -\frac{GMR}{(R^2 + z^2)^{3/2}}\hat{e}_R$$

*In Section 3.3.1, the requirement for mass outflow was $g_{eff} < 0$. This is because in that analysis g_{eff} had been reduced to a magnitude along the field line, and a positive value implied a direction towards the disc. In this section the configuration is slightly different, and a negative direction is towards the spin axis.

and

$$g_{cent}\hat{e}_R = \Omega^2 R\hat{e}_R = \frac{v_\phi^2}{R}\hat{e}_R$$

respectively. The condition that material will collimate around the spin axis is then

$$|g_{grav}| > |g_{cent}|.$$

After some re-arranging this condition requires that

$$\frac{GM}{R^2 \left[1 + \left(\frac{z}{R}\right)^2\right]^{3/2}} > \Omega^2 R.$$

Small values of R and z can satisfy this condition, and the consequence is that material within the region will experience a net force directed towards the z -axis. This implies that outflowing material near the poles can be collimated towards the z -axis and is a possible mechanism for jets formation in astrophysical sources.

In order to determine the possible effect a rotating magnetosphere will have in LS 5039, numerical calculations were obtained for a range of values, that can be considered reasonable for the system.

Numerical Calculations

To obtain a picture of the effect of a rotating magnetosphere, a wide range for the mass and spin frequencies were considered. The mass range covered was $1.5 - 3 M_\odot$, while the spin frequency considered was $20 - 200 \text{ s}^{-1}$ which corresponds to 1 to 10 times the spin period of the Crab pulsar. The calculations of the effective gravity using Equation 4.7, are independent of the strength of the magnetosphere, and only models its effect by considering the centrifugal force that results from it.

Figures 4.16–4.23 shows some of the calculated effective gravities and the respective contour lines. The contours lines show the effective gravity in units of cm s^{-2} , while the vertical dashed line represents the position of the light cylinder.

While in each case the values differ slightly, the general trend remains the same for the ranges of parameters covered. In all cases the light cylinder lies well within the binary system, orders of magnitude away from the optical companion, and within the accretion radius implied by wind accretion, $r_{acc} \sim 10^{10} \text{ cm}$. The acceleration predicted beyond the light cylinder is of course not physically possible. While the magnetic field lines may extend beyond the light cylinder[†], particles cannot remained attached in co-rotation in this region, since this would require that their velocities exceed the speed of light. The maximum centrifugal acceleration will occur near

[†]The magnetic field lines are simply a mathematical entity with no physical component. Therefore a rotational velocity exceeding the speed of light does not violate the laws of special relativity.

the light cylinder where

$$\begin{aligned}
 g_{cent} &= \Omega^2 R_{lc} \\
 &= \Omega^2 \frac{c}{\Omega} \\
 &= \Omega c.
 \end{aligned}$$

The calculations of the effective gravity demonstrate that for a rapidly rotating magnetosphere any form of accreting material must first overcome a high potential barrier before it is possible to accrete onto the surface of the compact object. If the compact object in LS 5039 is a NS, the rotational velocities considered are not unrealistic.

If the Alfvén radius is taken as measure of the position where the magnetic pressure dominates the particle pressure, the results shown earlier (see Tables 4.3, 4.4 & 4.5) indicate that for a magnetic field strength $B \gtrsim 10^{10}$ G, the Alfvén radius exceeds the radius at which $g_{eff} = 0$. This implies that material accreting in LS 5039 could well experience a net outwards force that will prevent the accretion process. This is similar to the so called *propeller effect* that has been applied to systems such as AE Aqr (Meintjes and de Jager, 2000; Meintjes and Venter, 2003), where it accounts for the emission observed from the system. Since it appears that the possibility exists that similar processes may be applicable in LS 5039, it is necessary to determine whether such a process could create enough power to explain the observed emission, particularly the TeV gamma-rays.

4.4.6 MHD Power

It has been suggested earlier that the high ratio of VHE gamma-ray luminosity to inferred accretion power, for both BH and NS scenarios, implies a high conversion efficiency of accretion power to high energy emission, i.e. $> 20\%$. It has also been suggested that the rotational kinetic energy of a fast rotating NS provides an additional reservoir of energy that can drive the high energy emission. Figure 4.8 shows that for a rather broad range of NS periods and spin-down speeds the VHE gamma-ray luminosity above EGRET energies ($\epsilon_\gamma > 1$ GeV) can readily be accounted for.

It is now necessary to apply the condition of MHD power to see whether or not this process is capable of extracting the required power needed to explain the gamma-ray luminosity ($\sim 10^{34}$ erg s⁻¹).

The Propeller Effect–MHD Power Equation

The MHD power that can be extracted from dissipation of magnetosphere energy in a thin spherical shell of width comparable to the skin depth can be estimated by

$$P_{MHD} = 4\pi r^2 \delta \left(\frac{B(r)^2}{8\pi} \right) \Omega_*, \tag{4.8}$$

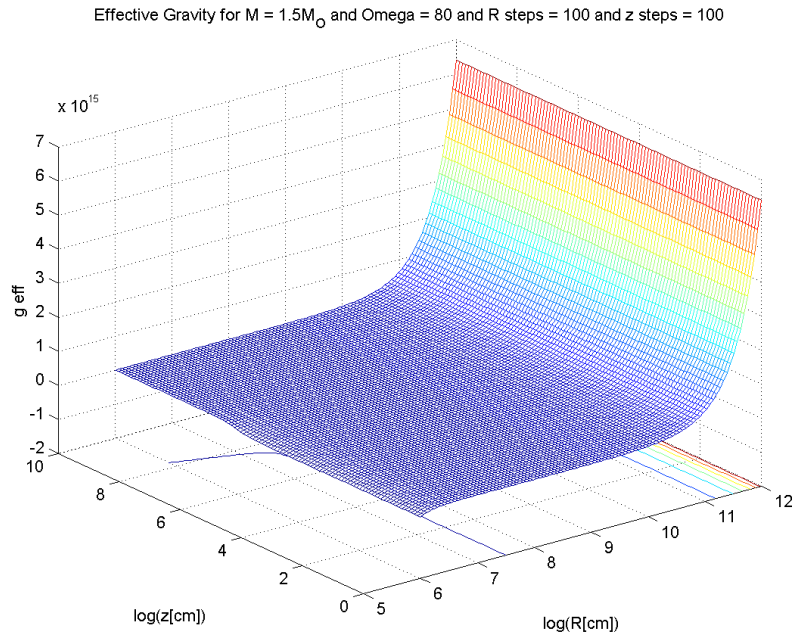


Figure 4.16: Effective gravity for $M = 1.5 M_{\odot}$ and $\Omega = 80 \text{ s}^{-1}$.

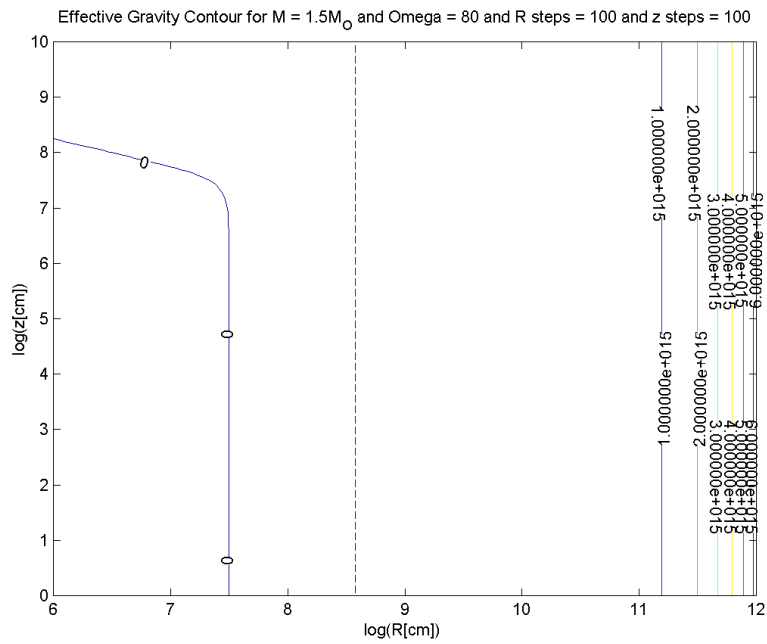


Figure 4.17: Contour lines of the effective gravity for $M = 1.5 M_{\odot}$ and $\Omega = 80 \text{ s}^{-1}$.

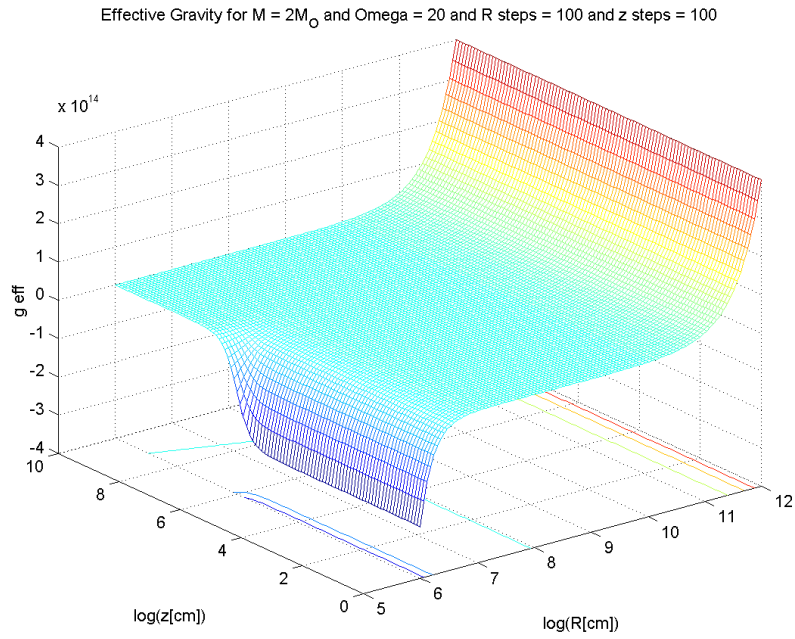


Figure 4.18: Effective gravity for $M = 2.0 M_{\odot}$ and $\Omega = 20 \text{ s}^{-1}$.

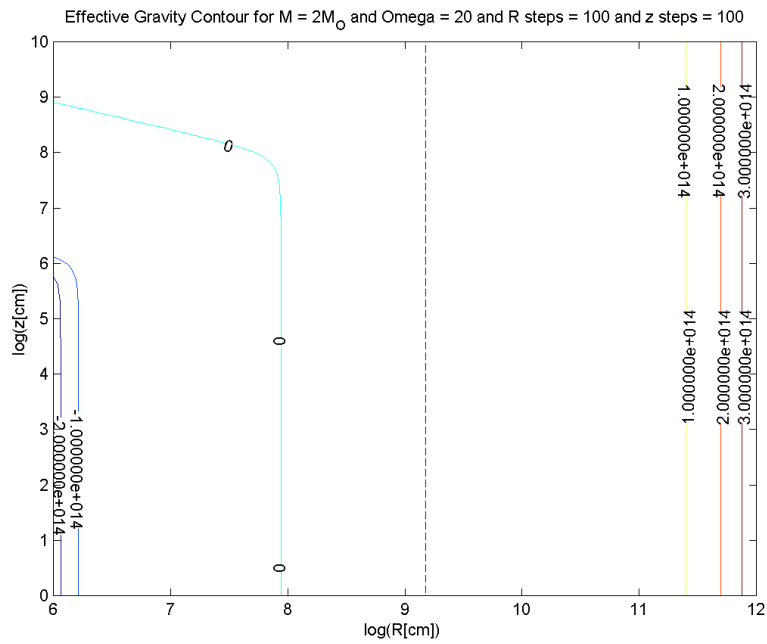


Figure 4.19: Contour lines of the effective gravity for $M = 2.0 M_{\odot}$ and $\Omega = 20 \text{ s}^{-1}$.

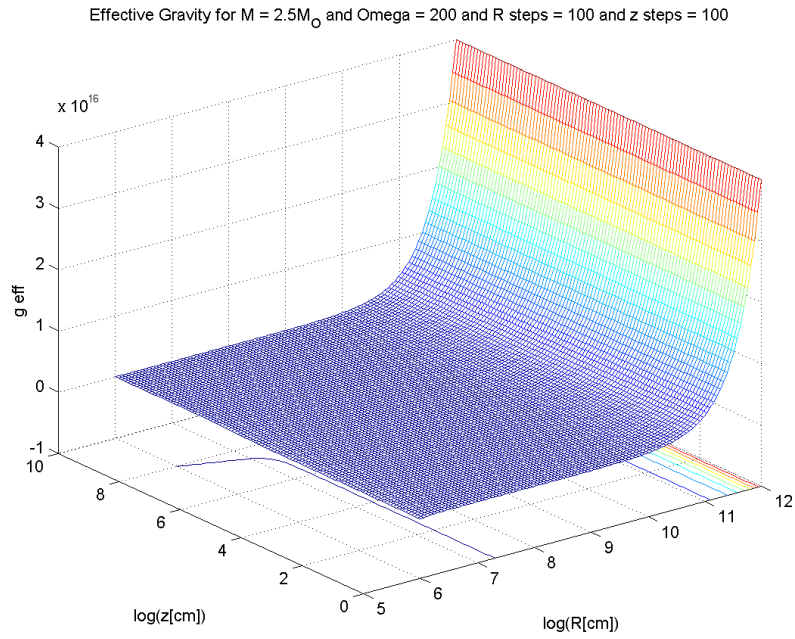


Figure 4.20: Effective gravity for $M = 2.5 M_{\odot}$ and $\Omega = 200 \text{ s}^{-1}$.

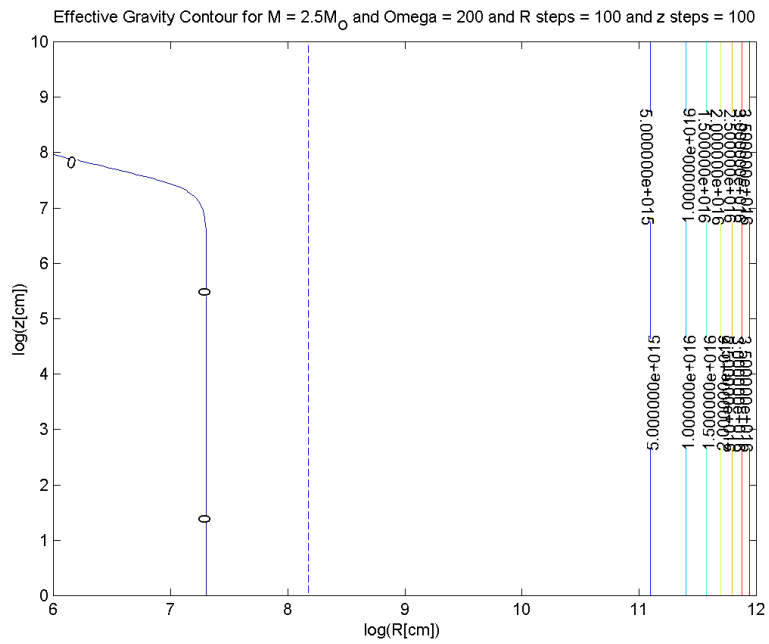


Figure 4.21: Contour lines of the effective gravity for $M = 2.5 M_{\odot}$ and $\Omega = 200 \text{ s}^{-1}$.

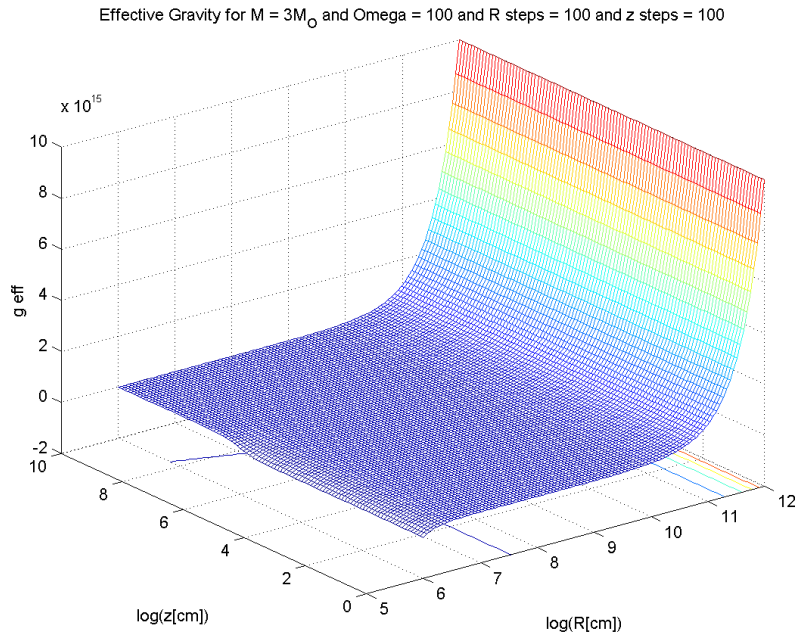


Figure 4.22: Effective gravity for $M = 3.0 M_{\odot}$ and $\Omega = 100 \text{ s}^{-1}$.

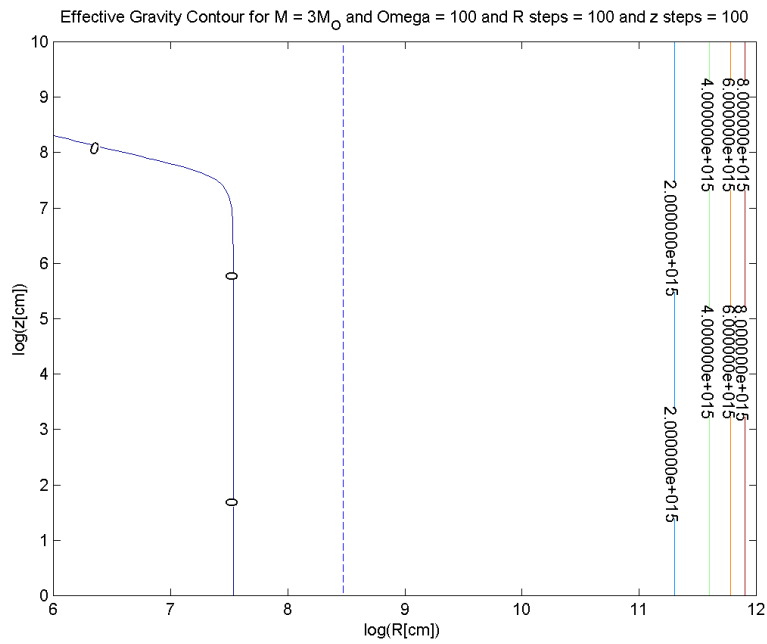


Figure 4.23: Contour lines of the effective gravity for $M = 3.0 M_{\odot}$ and $\Omega = 100 \text{ s}^{-1}$.

where r is the radial distance from the central magnetized compact object, $B(r)$ is the magnetic field strength at the distance r , and

$$\delta = \frac{c}{\sqrt{2\pi\sigma\Omega_*}},$$

represents the skin depth, where σ is the electrical conductivity, defined as

$$\sigma = \frac{(3kT)^{3/2}}{e^2 m_e^{1/2}}.$$

Here Ω_* is the rotational frequency ($2\pi/P_*$). Equation 4.8 gives a measure of the maximum amount of power that can be extracted from the propeller effect which will give an indication of the power that is available to create the observed emission. This effect must now be applied to LS 5039.

MHD Power in LS 5039

In order to obtain a simple approximation, the MHD power was considered at a distance of $r = 10^8$ cm, consistent with the distance to the Alfvén radius. For completeness, it was similarly considered at the distance of the possible PWN shock, $r = 10^{11}$ cm (Dubus, 2006b). Due to the high energy requirements implied by the VHE gamma-rays (Aharonian et al., 2006), surface magnetic field strengths of $B = 10^9 - 10^{16}$ G. $B(r)$ was approximated as a dipole field for a NS with a radius $R_{NS} = 10^6$ cm (Equation 2.29), while the spin frequency was considered over the range $\Omega = 20 - 600$ s⁻¹. In order to determine the electrical conductivity, σ , of the inflowing stellar wind, the temperature was considered being of the order of the surface temperature of the optical star, $T = 39\,000$ K (Casares et al., 2005). The results of these calculations are shown in Table 4.8.

These results show that MHD power of the above skin depth approximation is only capable of providing the required power ($> 10^{34}$ erg s⁻¹) in the case of very high magnetic field strengths, $B \sim 10^{16}$ G. Such extremely high field strengths are believed to be improbable in a system such as LS 5039.

It is important to note, however, that the effect of turbulence in the shock front can noticeably increase the power that can be extracted from the system. If a shock width of $0.1 r_{Alf}$ is considered, where the Alfvén radius is approximated as $r_{alf} \approx 10^9$ cm, and the spin-period as 30 ms, the power that would be extracted is

$$P_{MHD} \approx 10^{34} \left(\frac{B(r)}{1000 \text{ G}} \right)^2 \left(\frac{r_{Alf}}{10^9 \text{ cm}} \right)^2 \left(\frac{\delta}{0.1 r_{Alf}} \right) \left(\frac{P_*}{30 \text{ ms}} \right)^{-1} \text{ erg s}^{-1}.$$

This is a conservative estimate. The diffusion time of magnetic fields implied by this shock width is

Table 4.8: Skin depth approximation of the available MHD Power in LS 5039.

Alfvén radius (10^8 cm)		30	40	50	60	70	80	90
Ω								
B_* (G)								
1.0E+09	2.77E+24	3.39E+24	3.92E+24	4.38E+24	4.80E+24	5.18E+24	5.54E+24	5.87E+24
1.0E+10	2.77E+26	3.39E+26	3.92E+26	4.38E+26	4.80E+26	5.18E+26	5.54E+26	5.87E+26
1.0E+11	2.77E+28	3.39E+28	3.92E+28	4.38E+28	4.80E+28	5.18E+28	5.54E+28	5.87E+28
1.0E+12	2.77E+30	3.39E+30	3.92E+30	4.38E+30	4.80E+30	5.18E+30	5.54E+30	5.87E+30
1.0E+13	2.77E+32	3.39E+32	3.92E+32	4.38E+32	4.80E+32	5.18E+32	5.54E+32	5.87E+32
1.0E+14	2.77E+34	3.39E+34	3.92E+34	4.38E+34	4.80E+34	5.18E+34	5.54E+34	5.87E+34
1.0E+16	2.77E+38	3.39E+38	3.92E+38	4.38E+38	4.80E+38	5.18E+38	5.54E+38	5.87E+38
Ω	100	110	120	130	140	200	300	600
B_* (G)								
1.0E+09	6.19E+24	6.49E+24	6.78E+24	7.06E+24	7.33E+24	8.76E+24	1.07E+25	1.52E+25
1.0E+10	6.19E+26	6.49E+26	6.78E+26	7.06E+26	7.33E+26	8.76E+26	1.07E+27	1.52E+27
1.0E+11	6.19E+28	6.49E+28	6.78E+28	7.06E+28	7.33E+28	8.76E+28	1.07E+29	1.52E+29
1.0E+12	6.19E+30	6.49E+30	6.78E+30	7.06E+30	7.33E+30	8.76E+30	1.07E+31	1.52E+31
1.0E+13	6.19E+32	6.49E+32	6.78E+32	7.06E+32	7.33E+32	8.76E+32	1.07E+33	1.52E+33
1.0E+14	6.19E+34	6.49E+34	6.78E+34	7.06E+34	7.33E+34	8.76E+34	1.07E+35	1.52E+35
1.0E+16	6.19E+38	6.49E+38	6.78E+38	7.06E+38	7.33E+38	8.76E+38	1.07E+39	1.52E+39
PWN shock front (10^{11} cm)								
Ω		30	40	50	60	70	80	90
B_* (G)								
1.0E+09	2.43E+11	2.98E+11	3.44E+11	3.84E+11	4.21E+11	4.55E+11	4.86E+11	5.16E+11
1.0E+10	2.43E+13	2.98E+13	3.44E+13	3.84E+13	4.21E+13	4.55E+13	4.86E+13	5.16E+13
1.0E+11	2.43E+15	2.98E+15	3.44E+15	3.84E+15	4.21E+15	4.55E+15	4.86E+15	5.16E+15
1.0E+12	2.43E+17	2.98E+17	3.44E+17	3.84E+17	4.21E+17	4.55E+17	4.86E+17	5.16E+17
1.0E+13	2.43E+19	2.98E+19	3.44E+19	3.84E+19	4.21E+19	4.55E+19	4.86E+19	5.16E+19
1.0E+14	2.43E+21	2.98E+21	3.44E+21	3.84E+21	4.21E+21	4.55E+21	4.86E+21	5.16E+21
1.0E+16	2.43E+25	2.98E+25	3.44E+25	3.84E+25	4.21E+25	4.55E+25	4.86E+25	5.16E+25
Ω	100	110	120	130	140	200	300	600
B_* (G)								
1.0E+09	5.44E+11	5.70E+11	5.95E+11	6.20E+11	6.43E+11	7.69E+11	9.42E+11	1.33E+12
1.0E+10	5.44E+13	5.70E+13	5.95E+13	6.20E+13	6.43E+13	7.69E+13	9.42E+13	1.33E+14
1.0E+11	5.44E+15	5.70E+15	5.95E+15	6.20E+15	6.43E+15	7.69E+15	9.42E+15	1.33E+16
1.0E+12	5.44E+17	5.70E+17	5.95E+17	6.20E+17	6.43E+17	7.69E+17	9.42E+17	1.33E+18
1.0E+13	5.44E+19	5.70E+19	5.95E+19	6.20E+19	6.43E+19	7.69E+19	9.42E+19	1.33E+20
1.0E+14	5.44E+21	5.70E+21	5.95E+21	6.20E+21	6.43E+21	7.69E+21	9.42E+21	1.33E+22
1.0E+16	5.44E+25	5.70E+25	5.95E+25	6.20E+25	6.43E+25	7.69E+25	9.42E+25	1.33E+26

$$\begin{aligned}
t &= \frac{L^2}{\eta} \\
&\approx 100 \left(\frac{L}{0.1 r_{Alf}} \right)^2 \left(\frac{\eta}{10^{14}} \right)^{-1} \text{ sec},
\end{aligned}$$

where

$$\begin{aligned}
\eta &\approx c_s R \\
&\leq 10^{14} \left(\frac{c_s}{10^6 \text{ cm s}^{-1}} \right) \left(\frac{R}{0.1 r_{Alf}} \right) \text{ cm}^{-2} \text{ s}^{-1}.
\end{aligned}$$

The rapid diffusion of the magnetospheric field into the shocked region which forms the boundary between the magnetosphere and stellar wind will result in the generation of huge toroidal fields as a result of the differential motion. This will provide an extremely effective mechanism of extracting rotational kinetic energy from the fast rotating NS, capable of driving the total non-thermal emission from radio to TeV gamma-rays. This simple example shows the enormous amount of additional power that can be extracted from the system if turbulence is considered. It is likely that such a shocked-shell can occur in LS 5039 (e.g. Berezhinskii et al. (1990, p. 300)).

4.5 Magnetosphere as a Power Source

The analysis above shows the huge reservoir of power that is available from a rotating NS in LS 5039. The additional magnetosphere provides the magnetic field required to explain the non-thermal radiation to VHE gamma-ray energies. Of particular interest is the possibility of the Synchrotron Self-Compton process. Through this, it is possible to create the X-ray to EGRET energy photons through IC scattering of synchrotron produced electrons in the Thomson limit. This most likely occurs for electrons with Lorentz factors between $10^4 - 10^6$. The production of the TeV gamma-rays will most likely occur through IC scattering in the Klein-Nishina limit with electrons with Lorentz factors $\gamma > 6 \times 10^7$.

An analysis of the effective gravity shows that the gravitational component of the NS only begins to dominate close to the surface of the compact object. At distances close to the Alfvén radius the effective gravity will accelerate particles out of the system. This result implies that accretion may be impossible in the system. This would effectively create a vacuum condition close to the pulsar and the particle acceleration required will occur along the open field lines originating from the pulsar. Material that attempts to accrete onto the surface of the NS will become trapped along magnetic field lines and is accelerated out of the system. Figure 4.24 shows the expected scenario.

In the ideal MHD limit, a skin depth analysis of the MHD power extraction near the Alfvén radius does not provide sufficient power to drive the multi-wavelength emission up to TeV gamma-

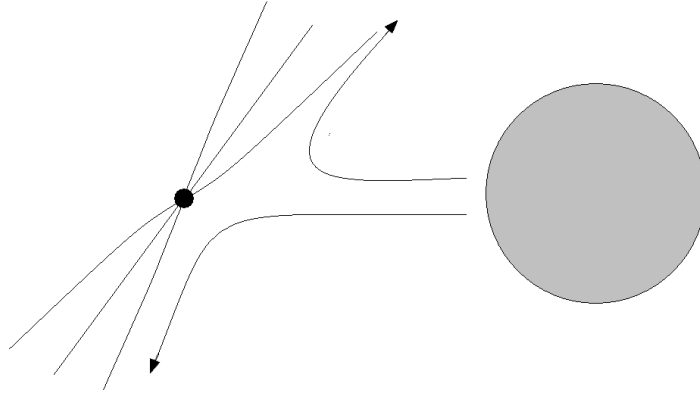


Figure 4.24: Sketch of the possible scenario in LS 5039. The propeller mechanism may prevent all accretion onto the compact object. Material that is directed towards the poles may become collimated through centrifugal forces, creating the radio “jet” structures.

ray energies. This is however not true if it is assumed that turbulence plays a role in this region. The simple example shown above demonstrates that in a turbulent shocked region of thickness $d \sim 0.1 r_{Alf} \sim 10^8$ cm, the resulting MHD power is $P \sim 10^{34}$ erg $^{-1}$, consistent with the luminosity of the VHE gamma-rays. As a result of the enormous centrifugal expulsion of plasma, combined with particle outflow from the fast rotating NS via a Goldreich-Julian mechanism, outflowing plasma along field lines significantly above the equatorial region will be collimated towards the rotational axis. This can explain the jet-like outflow observed in radio observations.

Chapter 5

Conclusion

This study was undertaken to investigate the nature of the compact object in LS 5039. The system has received significant attention in the last few years due to its proposed classification as a microquasar, and then because of its association with high energy gamma-rays. The compact object has been proposed as a BH candidate ($M = 3.7_{-1.0}^{+1.3} M_{\odot}$), but it has been argued in this study that this mass value should not be automatically accepted. The constraints on the inclination angle place the mass value above $1.49 \pm 0.11 M_{\odot}$, allowing for the possibility of a NS compact object.

The methodology followed in this study was to attempt to describe the system using a *model independent* approach, i.e. to attempt to model the system from first principles. For this reason, the first three chapters of this study have covered a wide range of theory, applicable to all high mass binaries. Preference was however given to the super-giant class of HMXBs where applicable, since the optical companion has been directly measured as an O-type giant.

Due to the binary nature of the system, it was necessary to discuss concepts such the *Two-Body problem*, and accretion driven processes. Attention was paid to a number of different aspects of accretion since it is the power source of most X-ray binaries. These aspects included; Roche lobe geometry, wind accretion, and accretion onto magnetized compact objects. The evolution of HMXBs was also discussed. This provides the frame work in which X-ray binaries, particularly HMXBs, must be considered.

The discussion then progressed to a theoretical overview of various radiation mechanisms to provide the frame work for studying the emission from LS 5039. Various mechanisms for removing material from a binary system were also considered, including the effect of magnetic pressure and the Blandford-Znajek model. Since a model in terms of a young pulsar has been proposed for the system, the theory of pulsars and pulsar winds was also included.

A model of LS 5039 has to explain a number of different features, the most important of which are:

1. The broad non-thermal emission from radio to VHE gamma-rays,

2. The power source involved in the production of this broad emission; in particular whether it is able to explain the luminosity of the TeV energy gamma-rays,
3. The orbital modulation detected in X-ray and gamma-rays, and
4. The processes that create the jet-like structures observed in radio.

The two models that have previously been applied are an accretion driven, microquasar model and a young, wind-producing, pulsar model, both of which are able to explain the broad-band spectrum reasonably well. Since each of these models depends on two different compact object (BH or NS/pulsar) and very different explanations for how the observed emission is created (acceleration in a jet or PWN shock front), it was decided to investigate what conclusions could be drawn about LS 5039 from first principles.

The analysis first looked at the possibility of an accretion disc or ring structure around a BH compact object being able to explain the observed jet structures. The concept of thermal evaporation was applied to this scenario since it is the likely cause of outflow around a BH hole. A thermal evaporation scenario proves to be highly unlikely given the required disc temperature ($T > 10^7$ K). This, however, does not rule out a black hole scenario. Disc magnetohydrodynamics models such as the Blandford-Znajek may be capable of extracting rotational energy to create the high energy emission and radio jet-structures. The problem with these models is that they depend on additional assumptions. In addition, an accretion driven process would require a high conversion of energy $> 20\%$ to account for the luminosity of the system. This is made difficult by the low accretion rate, $\dot{M} \leq 10^{-5} \dot{M}_{wind}$, implied by the wind accretion scenario. The introduction of a magnetized compact object allows for an additional reservoir of power to account for the high energy luminosity.

Attention was then focused to the idea of a rotating NS with a significant magnetic field strength. Material captured through wind accretion will attempt to accrete through the magnetic field, resulting in a non-trivial interaction, and the consequences of this interaction were considered; in particular, whether it could be used to model the observed properties of LS 5039.

An application of the wind accretion model based on the parameters of the system show that the inflow rate of material captured by the gravitational potential of the compact object is roughly 10^{14} g s⁻¹. Applying this to a range of masses and magnetic field strengths gives an Alfvén radius of $\lesssim 3 \times 10^9$ cm. Such a distance is well within the binary separation and is within the estimated accretion radius of 1.6×10^{10} cm. This suggests that the production site of the non-thermal radiation lies close to the compact object. This is consistent with the observed modulation of the X-ray and gamma-ray flux.

Constraining the synchrotron and IC radiation to the conditions at the Alfvén radius shows that ultra-relativistic electron energies are required to produce TeV level radiation. A Lorentz factor, $\gamma > 6 \times 10^7$, is required to create the VHE gamma-ray emission (3×10^{13} eV) through IC scattering, will most likely occur in the extreme Klein-Nishina limit. The possibility of Synchrotron Self-Compton process occurring in this region should not be overlooked. Electrons

with Lorentz factors between $10^4 - 10^6$ will readily produce synchrotron radiation which will allow for IC radiation (in the Thomson limit) to produce the EGRET level gamma-rays.

Estimations of the effective gravity from a possible magnetosphere in LS 5039 shows that for surface magnetic field strengths $B \gtrsim 10^{10}$ G, inflow is only dominated by the gravitational force at distances less than the Alfvén radius. This effectively means that at distances where the magnetic pressure begins to dominate, the centrifugal force of the rotating magnetosphere implies a net outwards acceleration. This implies that, for the value range considered, accretion onto the compact object is impossible in LS 5039. Material that is channeled along open field lines near the poles of the NS, can become collimated and account for the observed radio jet-structures. While it might be argued that the misalignment of the jet relative to the core is produced by a processing jet, and as such is evidence of an accretion disc, it must be noted that jet structures seen in pulsar systems are by no means simple. The jet structure in the Vela pulsar, for example, shows complicated motion (Pavlov et al., 2003). This, in combination with the unconsidered effect of the interaction with the stellar wind, could easily explain the shape of the jets.

The MHD power that can be extracted from LS 5039 in the case of a skin depth shock is unable to produce the required power to explain the luminosity of the system, without considering values that are believed to be unreasonable for a binary pulsar system. The introduction of turbulence to this region, though, drastically increases the amount of energy that is extracted. For a conservative estimation of the turbulence thickness, it was shown that the power that is extracted increases to values consistent with the luminosity of the VHE energy emission.

The one property that was not modelled during this study is the orbital modulation of the X-ray and gamma-ray flux. This is most likely the result of the increase in pair-production near periastron. The increase in stellar wind density will also have an effect on the position of the Alfvén radius and the production region of the non-thermal emission. These effects, combined with the possibility of pair cascade may be able to explain the modulation.

This study has demonstrated that it is possible to explain the broad non-thermal emission and jet structures from first principles. It also suggests that a fast rotating NS is a more likely source of power in LS 5039 than a BH. As such it is proposed that the compact object in the system LS 5039 has been classified as a BH, and the system as a microquasar, without sufficient evidence.

Future Work

The simple model proposed above opens up a wide range of possibilities for the system. These will need to be investigated in more detail in future studies. The fast rotating NS in the turbulent environment of the stellar wind must create a turbulent shock front that will allow for enormous dissipation of rotational kinetic energy. The aim of future studies will be to attempt to apply a numerical model to the system. In this way it is hoped that some of the concepts that were presented in this study may be examined in detail.

The interaction between the magnetosphere and the inflowing material at the Alfvén radius needs to be examined beyond the simple illustration presented. The MHD power that can be extracted will vary for different assumed magnetic field strengths, inflow rates and turbulence in the material. How this will be influenced by the orbital motion must also be considered.

This process will influence the non-thermal radiation, and in particular the production of VHE gamma-rays. It is most likely that the TeV energy gamma-rays detected by H.E.S.S. are created through the up-scattering of photons. The photons may be supplied by the optical companion, or by synchrotron radiation. The synchrotron self-Compton process, will most likely have an influence on the production of gamma-rays, and this is a concept that must be expanded and studied in more detail.

It is believed that the development of a numerical model to analyse the MHD process mentioned above will allow for an improved understanding of the system.

Acknowledgements

There are a number of people who must be thanked, because if it had not been for them this dissertation would never have been possible.

- Prof. Pieter Meintjes: For the many, many hours spent working with me and for the multitude of suggestions and advice, without which this would never have been possible.
- The Department of Physics, UFS: For the financial support, and for allowing me the opportunity to undertake this study.
- The National Research Foundation: Their financial support during this study has been greatly appreciated.
- My Parents: For reading every word, even though they understood very few of them.
- Angie: For everything.

List of Acronyms

ASM	All Sky Monitor
Be-XRB	Be X-ray Binary
BeppoSAX	<i>Beppo</i> Satellite per Astronomia a raggi X (<i>Beppo</i> Satellite for X-ray astronomy)
BH	Black Hole
EGRET	Energetic Gamma Ray Experiment Telescope
EVN	European VLBI Network
GBI	Green Bank Interferometer
H.E.S.S.	High Energy Stereoscopic System
HMXB	High Mass X-ray Binary
IC	Inverse Compton
INFC	Inferior Conjunction
ISM	Interstellar Medium
LMXB	Low Mass X-ray Binary
MERLIN	Multi-Element Radio Linked Interferometer Network
MHD	Magnetohydrodynamics
NS	Neutron Star
NW	North West
PCA	Proportional Counter Array
PWN	Pulsar Wind Nebula
REXRB	Radio Emitting X-ray Binary
ROSAT	Röntgen Satellite
RXTE	Rossi X-ray Timing Explorer
SE	South East
SIMBAD	Set of Identifications, Measurements, and Bibliography for Astronomical Data
SN	Supernova
SNR	Supernova Remnant
SSC	Synchrotron self-Compton
SUPC	Superior Conjunction
SXRB	Supergiant X-ray Binary
VHE	Very High Energy
VLA	Very Large Array
VLBA	Very Long Baseline Array
VLBI	Very Long Baseline Interferometry
XRБ	X-ray Binary

Bibliography

- F. Aharonian, A. G. Akhperjanian, K.-M. Aye, A. R. Bazer-Bachi, and *et al.* Discovery of the binary pulsar PSR B1259-63 in very-high-energy gamma rays around periastron with HESS. *A&A*, 442:1–10, 2005.
- F. Aharonian, A. G. Akhperjanian, A. R. Bazer-Bachi, M. Beilicke, and *et al.* 3.9 day orbital modulation in the TeV γ -ray flux and spectrum from the X-ray binary LS 5039. *A&A*, 460: 743–749, 2006.
- G Arfken. *Mathematical Methods for Physicists*. Academic Press, Inc., 3rd edition, 1985.
- Arthur Beiser. *Concepts of Modern Physics*. McGraw-Hill, 6th edition, 2003.
- V. S. Berezhinskii, S. V. Bulanov, V. A. Dogiel, and V. S. Ptuskin. *Astrophysics of cosmic rays*. Amsterdam: North-Holland, 1990, edited by Ginzburg, V.L., 1990.
- D. Bhattacharya and E. P. J. van den Heuvel. Formation and evolution of binary and millisecond radio pulsars. *Physics Reports*, 203:1–124, 1991.
- R. D. Blandford and D. G. Payne. Hydromagnetic flows from accretion discs and the production of radio jets. *MNRAS*, 199:883–903, June 1982.
- R. D. Blandford and R. L. Znajek. Electromagnetic extraction of energy from Kerr black holes. *MNRAS*, 179:433–456, May 1977.
- G. R. Blumenthal and R. J. Gould. Bremsstrahlung, Synchrotron Radiation, and Compton Scattering of High-Energy Electrons Traversing Dilute Gases. *Reviews of Modern Physics*, 42: 237–271, 1970.
- Katherine M. Blundell and Michael G. Bowler. Symmetry in the Changing Jets of SS 433 and Its True Distance from Us. *ApJ*, 616:L159–L162, 2004.
- J. Boersma. Mathematical theory of the two-body problem with one of the masses decreasing with time. *BAN*, 15:291–301, May 1961.
- S. V. Bogovalov and D. V. Khangoulyan. The Crab Nebula: Interpretation of Chandra Observations. *Astronomy Letters*, 28:373–385, June 2002. doi: 10.1134/1.1484137.

- S. V. Bogovalov, V. M. Chechetkin, A. V. Koldoba, and G. V. Ustyugova. Interaction of pulsar winds with interstellar medium: numerical simulation. *MNRAS*, 358:705–715, April 2005. doi: 10.1111/j.1365-2966.2004.08592.x.
- C. T. Bolton. Identification of Cygnus X-1 with HDE 226868. *Nature*, 235:271–273, 1972.
- H. Bondi and F. Hoyle. On the mechanism of accretion by stars. *MNRAS*, 104:273–282, 1944.
- V. Bosch-Ramon, J. M. Paredes, M. Ribó, J. M. Miller, P. Reig, and J. Martí. Orbital X-Ray Variability of the Microquasar LS 5039. *ApJ*, 628:388–394, 2005.
- R. L. Bowers and T. Deeming. Astrophysics. Volume 1 - Stars. *Journal of Biological Physics*, 1984.
- R. H. Boyer and R. W. Lindquist. Maximal Analytic Extension of the Kerr Metric. *Journal of Mathematical Physics*, 8:265–281, February 1967.
- J. Casares, M. Ribó, I. Ribas, J. M. Paredes, J. Martí, and A. Herrero. A possible black hole in the gamma-ray microquasar LS 5039. *MNRAS*, 364:899–908, 2005.
- J. I. Castor, D. C. Abbott, and R. I. Klein. Radiation-driven winds in Of stars. *ApJ*, 195: 157–174, January 1975.
- S. Chandrasekhar. The Maximum Mass of Ideal White Dwarfs. *ApJ*, 74:81–82, July 1931.
- A. R. Choudhuri. *The physics of fluids and plasmas : an introduction for astrophysicists* /. The physics of fluids and plasmas : an introduction for astrophysicists / Arnab Rai Choudhuri. New York : Cambridge University Press, 1998. QB466.F58 C46 1998, December 1998.
- J. S. Clark, P. Reig, S. P. Goodwin, V. M. Larionov, P. Blay, M. J. Coe, J. Fabregat, I. Negueruela, I. Papadakis, and I. A. Steele. On the radio emitting high mass X-ray binary LS 5039. *A&A*, 376:476–483, 2001.
- M. J. Coe. Be stars in X-ray binary systems. In M. A. Smith, H. F. Henrichs, and J. Fabregat, editors, *IAU Colloq. 175: The Be Phenomenon in Early-Type Stars*, volume 214 of *Astronomical Society of the Pacific Conference Series*, pages 656–+, 2000.
- P. S. Conti. Stellar parameters of five early type companions of X-ray sources. *A&A*, 63:225–235, February 1978.
- P. S. Conti and W. R. Alschuler. Spectroscopic Studies of O-Type Stars. I. Classification and Absolute Magnitudes. *ApJ*, 170:325–344, December 1971.
- M. Cropper. The Polars. *Space Science Reviews*, 54:195–295, December 1990.
- K. Davidson and J. P. Ostriker. Neutron-Star Accretion in a Stellar Wind: Model for a Pulsed X-Ray Source. *ApJ*, 179:585–598, January 1973.

- R. E. Davies and J. E. Pringle. On accretion from an inhomogeneous medium. *MNRAS*, 191: 599–604, May 1980.
- J. C. C. Day. *Parallel Detection of Cathodoluminescence*. PhD thesis, UNIVERSITY OF BRISTOL (UNITED KINGDOM)., 1988.
- J. S. Drilling. UBV photometry of OB+ stars north of 1950.0 declination -15 . *The Astronomical Journal*, 80(2):128–130, February 1975.
- G. Dubus. Gamma-ray absorption in massive X-ray binaries. *A&A*, 451:9–18, May 2006a. doi: 10.1051/0004-6361:20054233.
- G. Dubus. Gamma-ray binaries: pulsars in disguise? *A&A*, 456:801–817, 2006b.
- P. P. Eggleton. Approximations to the radii of Roche lobes. *ApJ*, 268:368–369, May 1983. doi: 10.1086/160960.
- A. C. Fabian and M. J. Rees. SS 433 - A double jet in action. *MNRAS*, 187:13P–16P, 1979.
- S. Fabrika. The jets and supercritical accretion disk in SS433. *Astrophysics and Space Physics Reviews*, 12:1–152, 2004.
- R. Fender. *Jets from X-ray binaries*, pages 381–419. Compact stellar X-ray sources, April 2006.
- Juhan Frank, Andrew King, and Derek Raine. *Accretion Power in Astrophysics*. Cambridge University Press, 2nd edition edition, 1992.
- D. B. Friend and J. I. Castor. Radiation-driven winds in X-ray binaries. *ApJ*, 261:293–300, October 1982. doi: 10.1086/160340.
- B. M. Gaensler and P. O. Slane. The Evolution and Structure of Pulsar Wind Nebulae. *ARA&A*, 44:17–47, September 2006. doi: 10.1146/annurev.astro.44.051905.092528PDF: <http://arjournals.annualreviews.org/doi/pdf/10.1146/annurev.astro.44.051905.092528>.
- B. M. Gaensler, E. van der Swaluw, F. Camilo, V. M. Kaspi, F. K. Baganoff, F. Yusef-Zadeh, and R. N. Manchester. The Mouse that Soared: High-Resolution X-Ray Imaging of the Pulsar-powered Bow Shock G359.23-0.82. *ApJ*, 616:383–402, November 2004. doi: 10.1086/424906.
- E. B. Giacani, G. M. Dubner, N. E. Kassim, D. A. Frail, W. M. Goss, P. F. Winkler, and B. F. Williams. New Radio and Optical Study of the Supernova Remnant W44. *AJ*, 113:1379–1390, April 1997. doi: 10.1086/118352.
- W. Gilmore and E. R. Seaquist. Aperture synthesis of the radio structure of SS433. *Astronomical Journal*, 85:1486–1495, 1980.
- V. L. Ginzburg and S. I. Syrovatskii. Cosmic Magnetobremstrahlung (synchrotron Radiation). *ARA&A*, 3:297–350, 1965. doi: 10.1146/annurev.aa.03.090165.001501.

- Peter Goldreich and William II Julian. Pulsar Electrodynamics. *ApJ*, 157:869–880, 1969.
- M. Gottwald, N. E. White, and L. Stella. A search for X-ray periodicities from 4U 1700-37. *MNRAS*, 222:21P–25P, October 1986.
- R. J. Gould and G. P. Schröder. Pair Production in Photon-Photon Collisions. *Physical Review*, 155:1404–1407, March 1967. doi: 10.1103/PhysRev.155.1404.
- P.C. Gregory. Bayesian Analysis of Radio Observations of the Be X-Ray Binary LS I +61303. *ApJ*, 575:427–434, 2002.
- F. Haberl, N. E. White, and T. R. Kallman. An EXOSAT X-ray observation of one orbital cycle of 4U 1700-37/HD 153919. *ApJ*, 343:409–425, August 1989. doi: 10.1086/167714.
- J. Hardop, K. Rohlf, A. Slettebak, and J. Stock. *Luminous Stars in the Northern Milky Way*, volume I. Hamburg-Bergedorf, Hamburger Sternwarte-Warner and Swasey Obs., 1959.
- B. A. Harmon, C. A. Wilson, G. J. Fishman, V. Connaughton, W. Henze, W. S. Paciesas, M. H. Finger, M. L. McCollough, M. Sahi, B. Peterson, C. R. Shrader, J. E. Grindlay, and D. Barret. The Burst and Transient Source Experiment (BATSE) Earth Occultation Catalog of Low-Energy Gamma-Ray Sources. *ApJS*, 154:585–622, October 2004. doi: 10.1086/421940.
- R. C. Hartman, D. L. Bertsch, S. D. Bloom, A. W. Chen, P. Deines-Jones, J. A. Esposito, C. E. Fichtel, D. P. Friedlander, S. D. Hunter, L. M. McDonald, P. Sreekumar, D. J. Thompson, B. B. Jones, Y. C. Lin, P. F. Michelson, P. L. Nolan, W. F. Tompkins, G. Kanbach, H. A. Mayer-Hasselwander, A. Mücke, M. Pohl, O. Reimer, D. A. Kniffen, E. J. Schneid, C. von Montigny, R. Mukherjee, and B. L. Dingus. The Third EGRET Catalog of High-Energy Gamma-Ray Sources. *ApJS*, 123:79–202, July 1999. doi: 10.1086/313231.
- J. F. Hawley and S. A. Balbus. A Powerful Local Shear Instability in Weakly Magnetized Disks. II. Nonlinear Evolution. *ApJ*, 376:223–233, July 1991. doi: 10.1086/170271.
- A. Hewish, S. J. Bell, J. D. Pilkington, P. F. Scott, and R. A. Collins. Observation of a Rapidly Pulsating Radio Source. *Nature*, 217:709–+, February 1968.
- M. S. Hjellming and R. F. Webbink. Thresholds for rapid mass transfer in binary systems. I - Polytropic models. *ApJ*, 318:794–808, July 1987. doi: 10.1086/165412.
- R. M. Hjellming and K. J. Johnston. Ss433 - observing evolution in a precessing, relativistic jet. In *Extragalactic radio sources; Proceedings of the Symposium, Albuquerque, NM, August 3-7, 1981*, pages 197–203. Dordrecht, D. Reidel Publishing Co., 1982. 1982IAUS...97..197H.
- R. A. Hulse and J. H. Taylor. Discovery of a pulsar in a binary system. *ApJ*, 195:L51–L53, January 1975.
- J. D. Jackson. *Classical electrodynamics*. New York: Wiley, 1998, 3rd ed., 1998.

- Simon Johnston, R. N. Manchester, A. G. Lyne, M. Bailes, V. M. Kaspi, Guojun Qiao, and N. D'Amico. PSR 1259-63 - A binary radio pulsar with a Be star companion. *ApJ*, 387: L37–L41, 1992.
- S. D. Kawaler, I. Novikov, G. Srinivasan, G. Meynet, and D. Schaerer. *Stellar Remnants*. Saas-Fee Advanced Course 25. Lecture Notes 1995. Swiss Society for Astrophysics and Astronomy, XII, 340 pp., 9 tabs.. Springer-Verlag Berlin Heidelberg New York, 1996.
- C. F. Kennel and F. V. Coroniti. Confinement of the Crab pulsar's wind by its supernova remnant. *ApJ*, 283:694–709, August 1984a. doi: 10.1086/162356.
- C. F. Kennel and F. V. Coroniti. Magnetohydrodynamic model of Crab nebula radiation. *ApJ*, 283:710–730, August 1984b. doi: 10.1086/162357.
- D. Kilkenny, F. van Wyk, F. Marang, J. H. Spencer Jones, and D. C. B. Whittet. A study of reddened luminous stars in the southern Milky Way. III. VRI photometry. *South African Astronomical Observatory Circular*, 15:65–72, 1993.
- A. R. King. The evolution of compact binaries. *QJRAS*, 29:1–25, March 1988.
- A. R. King. The accretion of diamagnetic blobs by a rotating magnetosphere. *MNRAS*, 261: 144–148, March 1993.
- S. S. Komissarov and Y. E. Lyubarsky. Synchrotron nebulae created by anisotropic magnetized pulsar winds. *MNRAS*, 349:779–792, April 2004. doi: 10.1111/j.1365-2966.2004.07597.x.
- K. R. Lang. *Astrophysical formulae: A compendium for the physicist and astrophysicist*. New York, Springer-Verlag New York, Inc., 1974. 760 p., 1974.
- S. H. Langer and S Rappaport. Low-luminosity Accretion onto Magnetized Neutron Stars. *ApJ*, 257:733–751, 1982a.
- S. H. Langer and S. Rappaport. Low-luminosity accretion onto magnetized neutron stars. *ApJ*, 257:733–751, June 1982b. doi: 10.1086/160028.
- W. H. G. Lewin, J. van Paradijs, and E. van den Heuvel, editors. *X-ray Binaries*. Cambridge University Press, 1995.
- Q. Z. Liu, J. van Paradijs, and E. P. J. van den Heuvel. A catalogue of high-mass X-ray binaries. *A&AS*, 147:25–49, November 2000.
- M. A. Livingstone, V. M. Kaspi, and F. P. Gavriil. Long-Term Phase-coherent X-Ray Timing of PSR B0540-69. *ApJ*, 633:1095–1100, November 2005. doi: 10.1086/491643.
- F. J. Lu, Q. D. Wang, B. Aschenbach, P. Durouchoux, and L. M. Song. Chandra Observation of Supernova Remnant G54.1+0.3: A Close Cousin of the Crab Nebula. *ApJ Letters*, 568: L49–L52, March 2002. doi: 10.1086/340137.

- Y. E. Lyubarsky. On the structure of the inner Crab Nebula. *MNRAS*, 329:L34–L36, January 2002. doi: 10.1046/j.1365-8711.2002.05151.x.
- D. MacDonald and K. S. Thorne. Black-hole electrodynamics - an absolute-space/universal-time formulation. *MNRAS*, 198:345–382, January 1982.
- R. N. Manchester, G. B. Hobbs, A. Teoh, and M. Hobbs. The Australia Telescope National Facility Pulsar Catalogue. *AJ*, 129:1993–2006, April 2005. doi: 10.1086/428488.
- B. Margon, H. C. Ford, J. I. Katz, K. B. Kwitter, R. K. Ulrich, R. P. S. Stone, and A. Klemola. The bizarre spectrum of SS 433. *ApJ*, 230:L41–L45, 1979.
- J. Martí, J.M. Paredes, and M. Ribó. The system LS 5039: a new massive radio emitting X-ray binary. *A&A*, 338:L71–L74, 1998.
- A. Martocchia, C. Motch, and I. Negueruela. The low X-ray state of LS 5039 / RX J1826.2-1450. *A&A*, 430:245–253, January 2005. doi: 10.1051/0004-6361:20041390.
- K. O. Mason, M. G. Watson, and N. E. White, editors. *The Physics of Accretion onto Compact Objects*, volume 266 of *Lecture Notes in Physics*, Berlin Springer Verlag, 1986.
- M. Massi. LS I +61303 in the context of microquasars. *A&A*, 422:267–270, 2004.
- R. Matsumoto, T. Kudoh, K. Shibata, and M. R. Hayashi. Outflows and Jets from Magnetized Disks. In S. Howell, E. Kuulkers, and C. Woodward, editors, *Wild Stars in the Old West*, volume 137 of *Astronomical Society of the Pacific Conference Series*, pages 286–293, 1998.
- R. McCray, C. Wright, and S. Hatchett. Interstellar ultraviolet absorption lines and galactic X-ray sources. *ApJ Letters*, 211:L29–L33, January 1977.
- M. V. McSwain and D. R. Gies. Wind Accretion and Binary Evolution of the Microquasar LS 5039. *ApJ*, 568:L27–L30, 2002.
- M. V. McSwain, D. R. Gies, R. L. Riddle, Z. Wang, and D. W. Wingert. The Orbit of the Massive X-Ray Binary LS 5039. *ApJ*, 558:L43–L46, 2001.
- M. V. McSwain, D. R. Gies, W. Huang, P. J. Wiita, D. W. Wingert, and L. Kaper. The N Enrichment and Supernova Ejection of the Runaway Microquasar LS 5039. *ApJ*, 600:927–938, 2004.
- P. J. Meintjes. On the evolution of the nova-like variable AE Aquarii. *MNRAS*, 336:265–275, October 2002. doi: 10.1046/j.1365-8711.2002.05731.x.
- P. J. Meintjes and O. C. de Jager. Propeller spin-down and the non-thermal emission from AE Aquarii. *MNRAS*, 311:611–620, January 2000.

- P. J. Meintjes and L. A. Venter. Modelling the continuous radio outbursts in AE Aquarii. *MNRAS*, 341:891–900, May 2003. doi: 10.1046/j.1365-8711.2003.06459.x.
- Haim Mendelson and Tsevi Mazeh. Discovery of a 26.5-day optical periodicity of LSI+61 deg 303. *MNRAS*, 239:733–740, 1989.
- P. Meszaros, A. K. Harding, J. G. Kirk, and D. J. Galloway. Accreting X-ray pulsar atmospheres heated by Coulomb deceleration of protons. *ApJ Letters*, 266:L33–L37, March 1983. doi: 10.1086/183973.
- R. Moderski, M. Sikora, P. S. Coppi, and F. Aharonian. Klein-Nishina effects in the spectra of non-thermal sources immersed in external radiation fields. *MNRAS*, 363:954–966, November 2005. doi: 10.1111/j.1365-2966.2005.09494.x.
- C. Motch, F. Haber, K. Denner, M. Pakull, and E. Janot-Pacheco. New massive X-ray binary candidates from the ROSAT Galactic Plane Survey. *A&A Supplement Series*, 323:853–875, 1997.
- C.D. Murray and S.F. Dermott. *Solar System Dynamics*. Cambridge University Press, 1999.
- J. R. Oppenheimer and G. M. Volkoff. On Massive Neutron Cores. *Physical Review*, 55:374–381, February 1939. doi: 10.1103/PhysRev.55.374.
- J. P. Ostriker and J. E. Gunn. On the Nature of Pulsars. I. Theory. *ApJ*, 157:1395–1417, September 1969.
- A. G. Pacholczyk. *Radio astrophysics. Nonthermal processes in galactic and extragalactic sources*. Series of Books in Astronomy and Astrophysics, San Francisco: Freeman, 1970.
- F. Pacini. Rotating Neutron Stars, Pulsars and Supernova Remnants. *Nature*, 219:145–+, July 1968.
- B. Paczyński. Gravitational Waves and the Evolution of Close Binaries. *AcA*, 17:287–296, 1967.
- J. M. Paredes, J. Martí, M. Peracaula, and M. Ribó. Evidence of X-ray periodicity in LSI+61 303. *A&A*, 320,:L25–L28, 1997.
- J. M. Paredes, V. Bosch-Ramon, and G. E. Romero. Spectral energy distribution of the γ -ray microquasar LS 5039. *A&A*, 451:259–266, May 2006. doi: 10.1051/0004-6361:20054155.
- J.M. Paredes, M. Ribó, E. Ros, J. Martí, and M. Massi. Conrmaton of persistent radio jets in the microquasar LS 5039. *A&A*, 393:L99–L102, 2002.
- Josep M. Paredes, Josep Martí, and Maria Massi. Discovery of a High-Energy Gamma-Ray-Emitting Persistent Microquasar. *Science*, 288:2340–2342, 2000.

- G.G. Pavlov, M.A. Teter, O. Kargaltsev, and D. Sanwal. The Variable Jet of the Vela Pulsar. *ApJ*, 591:11571171, 2003.
- A. C. Phillips. *The physics of stars*. Chichester ; New York : Wiley, c1994., 1994.
- J. E. Pringle and M. J. Rees. Accretion Disc Models for Compact X-Ray Sources. *A&A*, 21:1–+, October 1972.
- J. Puls, R.-P. Kudritzki, A. Herrero, A. W. A. Pauldrach, S. M. Haser, D. J. Lennon, R. Gabler, S. A. Voels, J. M. Vilchez, S. Wachter, and A. Feldmeier. O-star mass-loss and wind momentum rates in the Galaxy and the Magellanic Clouds Observations and theoretical predictions. *A&A*, 305:171–208, January 1996.
- S. Rappaport and E. P. J. van den Heuvel. X-ray observations of Be stars. In M. Jасhek and H.-G. Groth, editors, *Be Stars*, volume 98 of *IAU Symposium*, pages 327–344, April 1982.
- S. Rappaport, G. W. Clark, L. Cominsky, F. Li, and P. C. Joss. Orbital elements of 4U 0115+63 and the nature of the hard X-ray transients. *ApJ*, 224:L1–L4, August 1978. doi: 10.1086/182745.
- M. J. Rees and J.E. Gunn. The Origin of the Magnetic Field and Relativistic Particles in the Crab Nebula. *MNRAS*, 167:1–12, 1974.
- P. Reig, M. Ribó, J. M. Paredes, and J. Martí. Long-term X-ray variability of the microquasar system LS 5039/RX J1826.2-1450. *A&A*, 405:285–290, 2003.
- S. P. Reynolds and H. D. Aller. Radio observations of the Crab-like supernova remnant 3C 58. I - Total intensity observations. *ApJ*, 327:845–852, April 1988. doi: 10.1086/166242.
- C. E. Rhoades and R. Ruffini. Maximum mass of a neutron star. *Physical Review Letters*, 32: 324–327, 1974.
- M. Ribó. Microquasars. In J. Romney and M. Reid, editors, *Future Directions in High Resolution Astronomy*, volume 340 of *Astronomical Society of the Pacific Conference Series*, pages 269–+, December 2005.
- M. Ribó, P. Reig, J. Martí, and J. M. Paredes. X-ray and radio observations of RX J1826.2-1450/LS 5039. *A&A*, 347:518–523, 1999.
- M. Ribó, J. M. Paredes, G. E. Romero, P. Benagli, J. Martí, O. Fors, and J. García-Sánchez. LS 5039: a runaway microquasar ejected from the galactic plane. *A&A*, 384:954–964, 2002.
- L. F. Rodríguez, I. F. Mirabel, and J. Martí. The radio counterpart of the hard X-ray source GRS 1758-258. *ApJ*, 401:,L15–L18, 1992.

- R. E. Rothschild, D. E. Gruber, F. K. Knight, J. L. Matteson, P. L. Nolan, J. H. Swank, S. S. Holt, P. J. Serlemitsos, K. O. Mason, and I. R. Tuohy. The X-ray spectrum of AM Herculis from 0.1 to 150 keV. *ApJ*, 250:723–732, November 1981. doi: 10.1086/159420.
- M. A. Ruderman and P. G. Sutherland. Theory of pulsars - Polar caps, sparks, and coherent microwave radiation. *ApJ*, 196:51–72, February 1975.
- B. F. Schutz. *A First Course in General Relativity*. A First Course in General Relativity, by Bernard F. Schutz, pp. 392. ISBN 0521277035. Cambridge, UK: Cambridge University Press, February 1985., February 1985.
- E. R. Seaquist, W. Gilmore, G. J. Nelson, W. J. Payten, and O. B. Slee. The quiescent radio spectrum of SS 433. *ApJ Letters*, 241:L77–L81, October 1980. doi: 10.1086/183365.
- S. L. Shapiro and A. P. Lightman. Black holes in X-ray binaries - Marginal existence and rotation reversals of accretion disks. *ApJ*, 204:555–560, March 1976.
- P. Slane, D. J. Helfand, E. van der Swaluw, and S. S. Murray. New Constraints on the Structure and Evolution of the Pulsar Wind Nebula 3C 58. *ApJ*, 616:403–413, November 2004. doi: 10.1086/424814.
- D. P. Smits. *The Structure and Evolution of Stars*. University of South Africa, Muckleneuk, Pretoria, 2002. UNISA study guide.
- J. H. Spencer Jones, D. C. B. Whittet, and L. He. A study of reddened luminous stars in the southern Milky Way. IV. JHK photometry. *South African Astronomical Observatory Circular*, 15:73–77, 1993.
- B. W. Stappers, B. M. Gaensler, V. M. Kaspi, M. van der Klis, and W. H. G. Lewin. An X-ray nebula associated with the millisecond pulsar B1957+20. *Science*, 299:1372–1374, 2003. doi: 10.1126/science.1079841.
- C.B. Stephenson and N. Sanduleak. *Luminous Stars in the Southern Milky Way*, volume I of 1. Warner and Swasey Obs., Hamburger Sternwarte-Warner and Swasey Obs., 1971.
- T. L. Swihart. *Astrophysics and stellar astronomy*. Space Science Text Series, New York: Wiley, 1968, 1968.
- T. M. Tauris and E. van den Heuvel. Formation and Evolution of Compact Stellar X-ray Sources. *ArXiv Astrophysics e-prints*, March 2003.
- S. A. Tjemkes, J. van Paradijs, and E. J. Zuiderwijk. Optical light curves of massive X-ray binaries. *A&A*, 154:77–91, January 1986.
- E. P. J. van den Heuvel and G. M. H. J. Habets. Observational lower mass limit for black hole formation derived from massive X-ray binaries. *Nature*, 309:598–600, July 1984.

- F. Verbunt. Accretion disks in stellar X-ray sources - A review of the basic theory of accretion disks and its problems. *SSRv*, 32:379–404, 1982.
- B. L. Webster and P. Murdin. Cygnus X-1a Spectroscopic Binary with a Heavy Companion ? *Nature*, 235:37 – 38, 1972.
- N. E. White. X-ray binaries. *A&ARv*, 1:85–110, April 1989.
- N. E. White, T. R. Kallman, and J. H. Swank. The X-ray absorption spectrum of 4U 1700-37 and its implications for the stellar wind of the companion HD 153919. *ApJ*, 269:264–272, June 1983. doi: 10.1086/161038.
- F. P. Wilkin. Exact Analytic Solutions for Stellar Wind Bow Shocks. *ApJ Letters*, 459:L31–L34, March 1996. doi: 10.1086/309939.
- G. A. Wynn and A. R. King. Diamagnetic accretion in intermediate polars - I. Blob orbits and spin evolution. *MNRAS*, 275:9–21, July 1995.